

REPORT NO. PD73-0123
CONTRACT NAS8-29859

(NAS8-01-111-43) CONICAL ISOGRID ADAPTER
STRUCTURAL TEST RESULTS. APPENDIX C:
CYLINDRICAL ISOGRID STRUCTURES (FOR THE
AVIATION/CONVAIL) TM 140-17. 1962 2 R

A7-34116

13/32 1975

CONICAL ISOGRID ADAPTER STRUCTURAL TEST RESULTS

APPENDIX C • CYLINDRICAL ISOGRID STRUCTURES

GENERAL DYNAMICS
Convair Division

REPORT NO. PD 73-0123

CONICAL ISOGRID ADAPTER STRUCTURAL TEST RESULTS

APPENDIX C ♦ CYLINDRICAL ISOGRID STRUCTURES

July 1974

Prepared Under
Contract NAS8-29859

Prepared by
GENERAL DYNAMICS CONVAIR DIVISION
P.O. Box. 80847
San Diego, California 92138

PD 73-0123
Appendix C

Prepared by Paul Slysh
P. Slysh
Sr. Design Engineer

Prepared by J. E. Dyer
(Sections J. E. Dyer
3.3 & 3.4) Sr. Structures Engineer

Approved E. J. Hujsak
E. J. Hujsak
Chief, LVP Predesign

FOREWORD

The information presented in this document was obtained as a result of the conical isogrid structural testing done by General Dynamics Convair Division under Contract NASA 8-29859. The contract was administered under the direction of John Key, Marshall Space Flight Center, NASA. Additional comparative data are presented from the cylindrical isogrid structural testing accomplished by NASA, Marshall Space Flight Center, in 1973.

These structures were developed and fabricated by Convair under Independent Research and Development funding. Appreciation is expressed to Mr. Jack Furman of the Marshall Space Flight Center, NASA, for his contribution and continued interest in the development and application of isogrid to the aerospace structures.

TABLE OF CONTENTS

<u>SECTION</u>	<u>PAGE</u>
C.1 INTRODUCTION	C-1
C.2 SUMMARY OF TEST DATA	C-1
C.2.1 TEST SETUP & INSTRUMENTATION	C-4
C.2.2 SPECIMEN FAILURE CONDITION	C-10
C.2.3 INSPECTION OF DAMAGED SPECIMEN	C-10
C.2.4 STRESSES IN FAILED GRID MEMBERS	C-10
C.2.5 STRESSES NEAR PEAK LOAD INTENSITY AREA	C-17
C.2.6 APPLIED LOADS	C-21
C.2.7 TOPOGRAPHICAL PLOTS	C-28
C.2.7.1 Program Description	C-29
C.2.7.2 Preliminary Evaluation	C-31
C.3 ANALYSIS OF TEST RESULTS	C-31
C.3.1 MODIFICATIONS OF GENERAL INSTABILITY KNOCKDOWN FACTORS	C-31
C.3.1.1 Knockdown Factor Corrections	C-37
C.3.2 EXTENDED LOCAL INSTABILITY ANALYSIS	C-38
C.3.2.1 Description of Model	C-38
C.3.2.2 Definition of Symbols	C-40
C.3.2.3 Isogrid Cross Sectional Properties	C-40
C.3.2.4 Analytical Formulation	C-41
C.3.2.5 Computerized Analysis	C-45
C.3.2.6 Numerical Evaluation	C-47
C.3.3 EFFECTIVE SKIN WIDTH	C-52
C.3.3.1 Test Data	C-54

PRECEDING PAGE BLANK NOT FILMED

<u>SECTION</u>	<u>PAGE</u>
C.3.3.2 Analytical Estimation of Effective Skin Width	C-59
C.3.3.3 Analysis Procedure	C-60
C.3.4 COMPRESSION BUCKLING OF SKIN PANELS	C-60
C.3.4.1 Measured Buckling Data Evaluation	C-60
C.3.4.2 Effects of Skin Edge Fixity	C-66
C.3.4.3 Analysis Procedure	C-69
C.4 SUMMARY AND RECOMMENDATIONS	C-69
C.5 REFERENCES	C-70

TABLE OF FIGURES

<u>FIGURE</u>		<u>PAGE</u>
C-1a	Isogrid Cylindrical Adapter (photograph)	C-2
C-1b	Isogrid Cylindrical Adapter (drawing)	C-3
C-2	View of test setup (side)	C-5
C-3	Close up of instrumentation	C-5
C-4	View of test setup (top)	C-6
C-5	Instrumentation reference	C-7
C-6	Jack bolt in bolted flange	C-9
C-7	Specimen near failure	C-11
C-8	Failed specimen	C-12
C-9	Close up of typically failed area	C-13
C-10	Inspection reference	C-14
C-11a-d	Stresses in failed grid members (longitudinal)	C-15
C-12	Stresses in failed grid members (diagonal)	C-18
C-13	Stresses near peak load intensity area	C-20
C-14	Circumferential stress distribution in structural transition	C-23
C-15	Differential forces on loading fixture	C-24
C-16	Measured displacement of upper loading fixture	C-25
C-17	Edge loading due to measured transition stresses	C-27
C-18	Topographical plot 250% load	C-29
C-19	Differential topographical plot 250-240% load	C-30
C-20a-d	Performance of test isogrid adapter	C-32
C-21a-d	Beam column model for extended local instability analysis	C-39
C-22	Computer program flow diagram	C-46
C-23a-d	Computed N_7 vs a	C-48

<u>FIGURE</u>		<u>PAGE</u>
C-24	Typical skin stringer geometry	C-54
C-25a-b	Typical local specimen strain data	C-55
C-26	Grid-skin stress distribution	C-57
C-27	Effective skin calculations	C-58
C-28a-d	Skin strains vs. load	C-62
C-29	Average panel geometry	C-66
C-30	Panel buckling coefficient vs. edge rigidity ratio	C-68

<u>TABLE</u>		
C-1	Applied edge loads	C-21
C-2	Summary of theoretical and actual critical loads	C-37
C-3	Computer printouts	C-53
C-4	K_c calculations	C-61
C-5	Panel geometry values	C-66
C-6	Table rigidity ratios	C-67

APPENDIX C

CYLINDRICAL ISOGRID STRUCTURES

C.1 INTRODUCTION

Continuing work started on the conical isogrid adapter (see Appendix B), the purpose of this handbook section is to present analysis techniques and data for evaluating the load carrying capabilities of cylindrical isogrid structures subjected to compression and body bending loads. The results in this section are based on a structural test performed at MSFC on a Convair Aerospace furnished 120-inch diameter by 37-inch long cylindrical adapter. The loading fixture for this test was also designed and fabricated at Convair Aerospace.

Figure C-1a is a photograph and Figure C-1b is a drawing of the flanged isogrid adapter structure considered. Its construction is similar to that of the conical isogrid adapter except for the grid configuration which includes parallel-longitudinal rather than radial members.

The approach of this handbook section will be: (1) to summarize test data resulting from a test on a cylindrical isogrid adapter, (2) to outline modifications to the techniques for predicting local and general instability described in Section B.2 of Appendix B, (3) to develop a method for predicting extended local instability on the basis of beam column effects in two tandem longitudinal grid members, (4) to apply the extended instability analysis to predict general instability in the test specimen, (5) to demonstrate the effects of basic parameter and constant variations in the extended local stability analysis, and (6) to evaluate effective skin width and compression buckling of skin panels on the basis of test data.

C.2 SUMMARY OF TEST DATA

This section contains a partial summary of the cylindrical isogrid structure test data for the final failure condition. Detail test results for all test conditions as well as a complete description of test setup and instrumentation is available in Reference C-1.

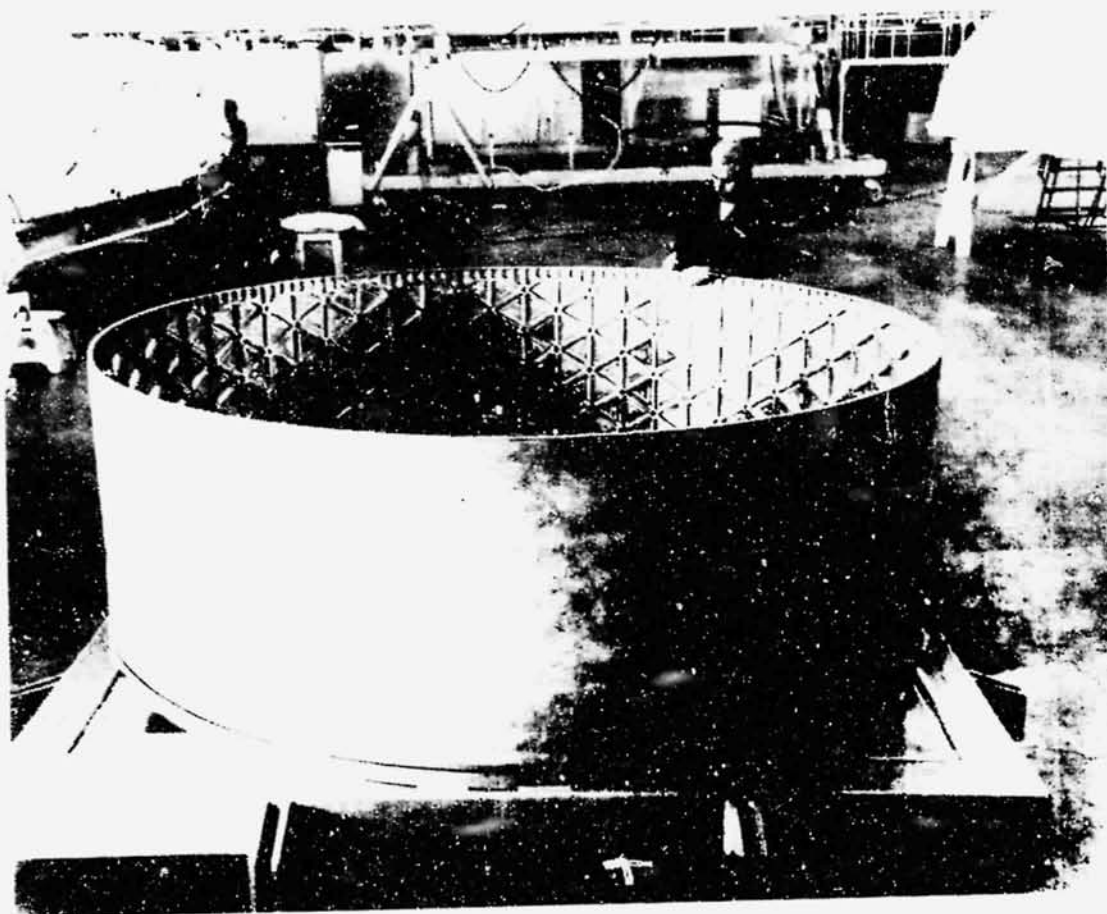
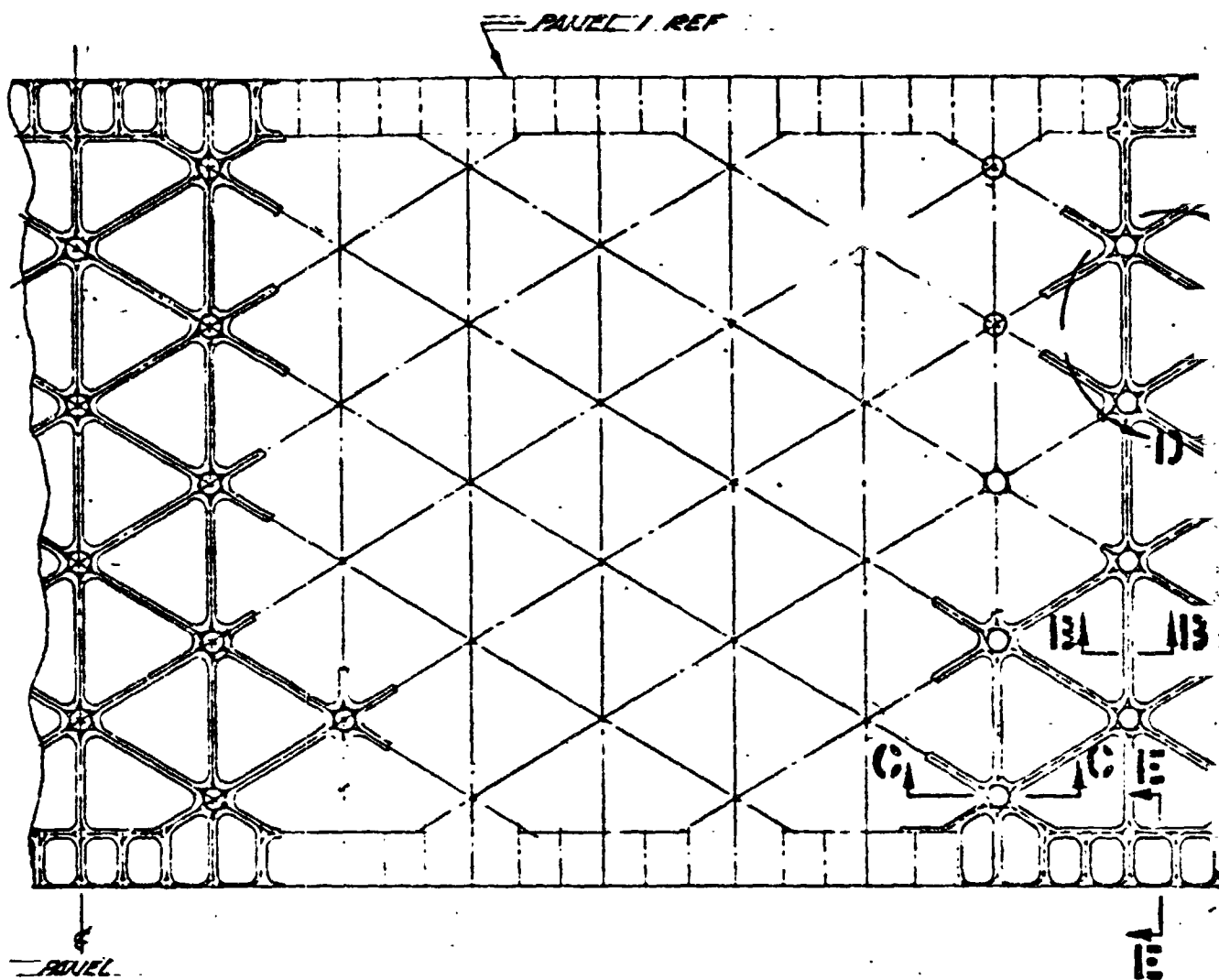
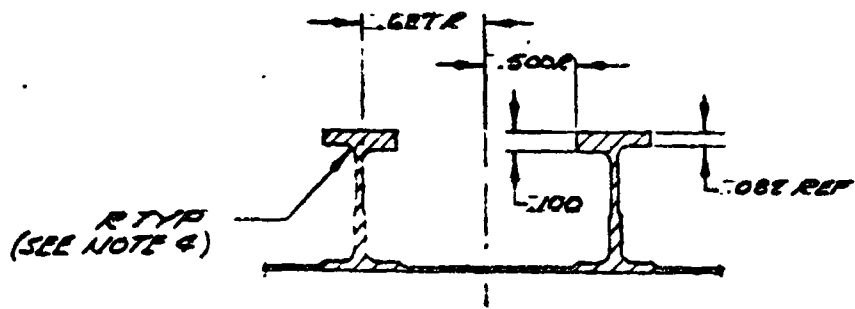


Figure C-la Isogrid cylinder adapter

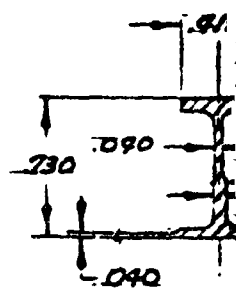


VIEW A-A TYP (ALL PANELS)
SCALE: 1/4

REPRODUCIBILITY OF THE
ORIGINAL PAGE IS POOR

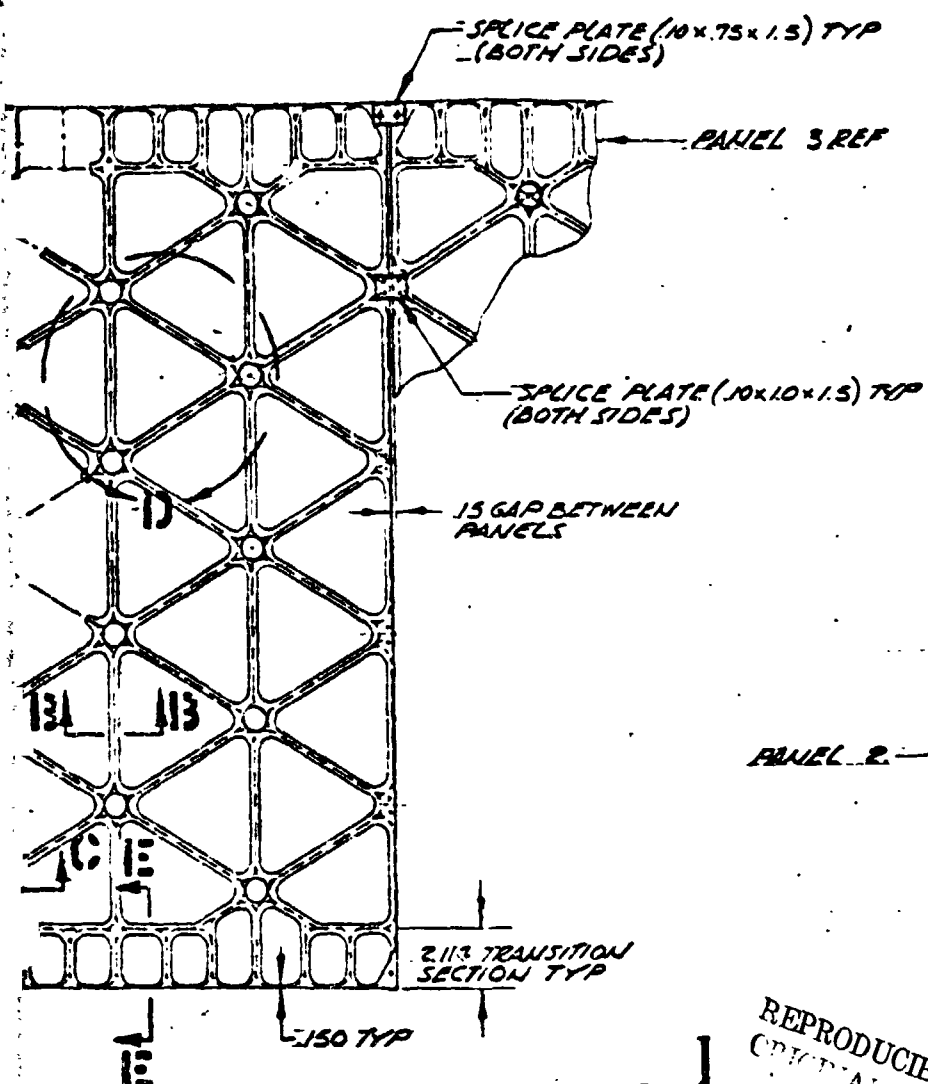


SECTION C-C TYP
SCALE: 2/1



SECTION D-D
SCALE: 2/1

FOLDOUT FRAME

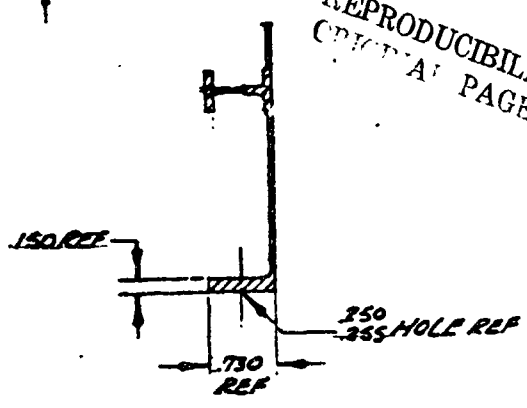


PANEL 2

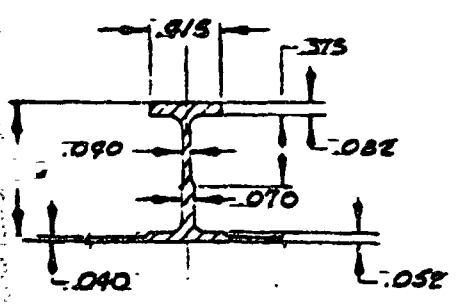
120.44

PANEL 1

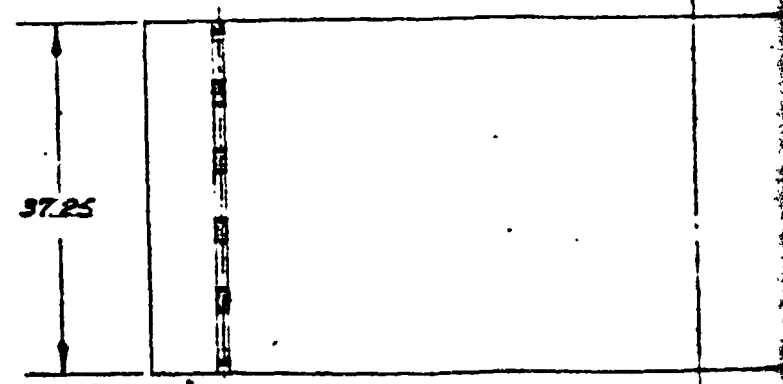
REPRODUCIBILITY OF THE
ORIGINAL PAGE IS POOR



SECTION 11-11 TYP
SCALE: 1/1

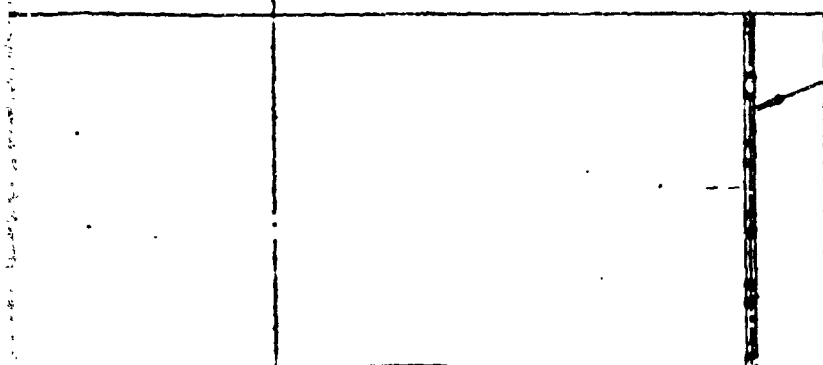
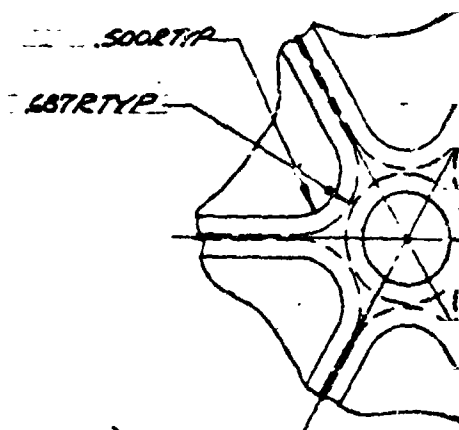
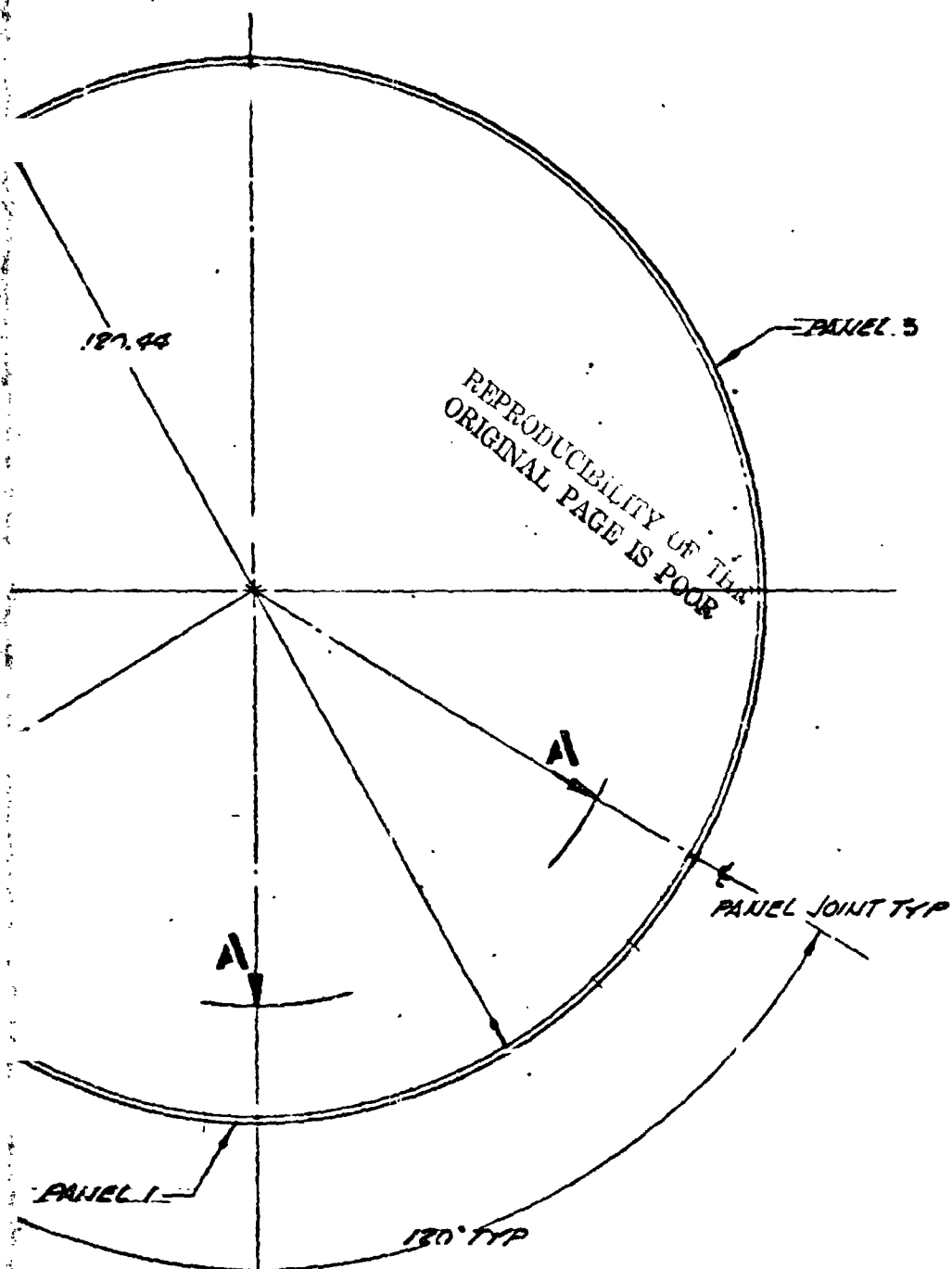


SECTION 13-13 TYP
SCALE: 2/1



FOLDOUT FRAME

2



SPICE PLATE (10x1.0x5.0)
(SKIN SIDE ONLY)

FOLDOUT FRA

3

NOTES:

1. MATERIAL - 2024-T351 AL ALLOY
2. ULTRASONIC INSPECT RAW MATERIAL PER Q-73517-1.
3. DEBUR ALL SHARP EDGES
4. ALL CORNER RADII .050-.070 UNLESS OTHERWISE NOTED
5. ALL FASTENERS - 3/16 DIA NICK BOLTS
6. POCKETS IN TRANSITION SECTION FIT BOLT PATTERN.
7. HEIGHT OF ISOGRID: 6.355
8. TOLERANCE: $\pm .010$
9. MACHINE PANELS IN THE T351 CONDITION. CLEAN (VAPOR DEGREASE)
10. FILL ISOGRID POCKETS WITH RIGIDAX - GREEN AND FACE OFF
11. AFTER FORMING, MELT OUT RIGIDAX AND CLEAN (VAPOR DEGREASE)
12. AGE TO T351 CONDITION BY HOLDING AT 375°F FOR 18 HOURS.
13. POCKETS OF TRANSITION SECTION BASED ON 2" ATTACHMENT SPACING.

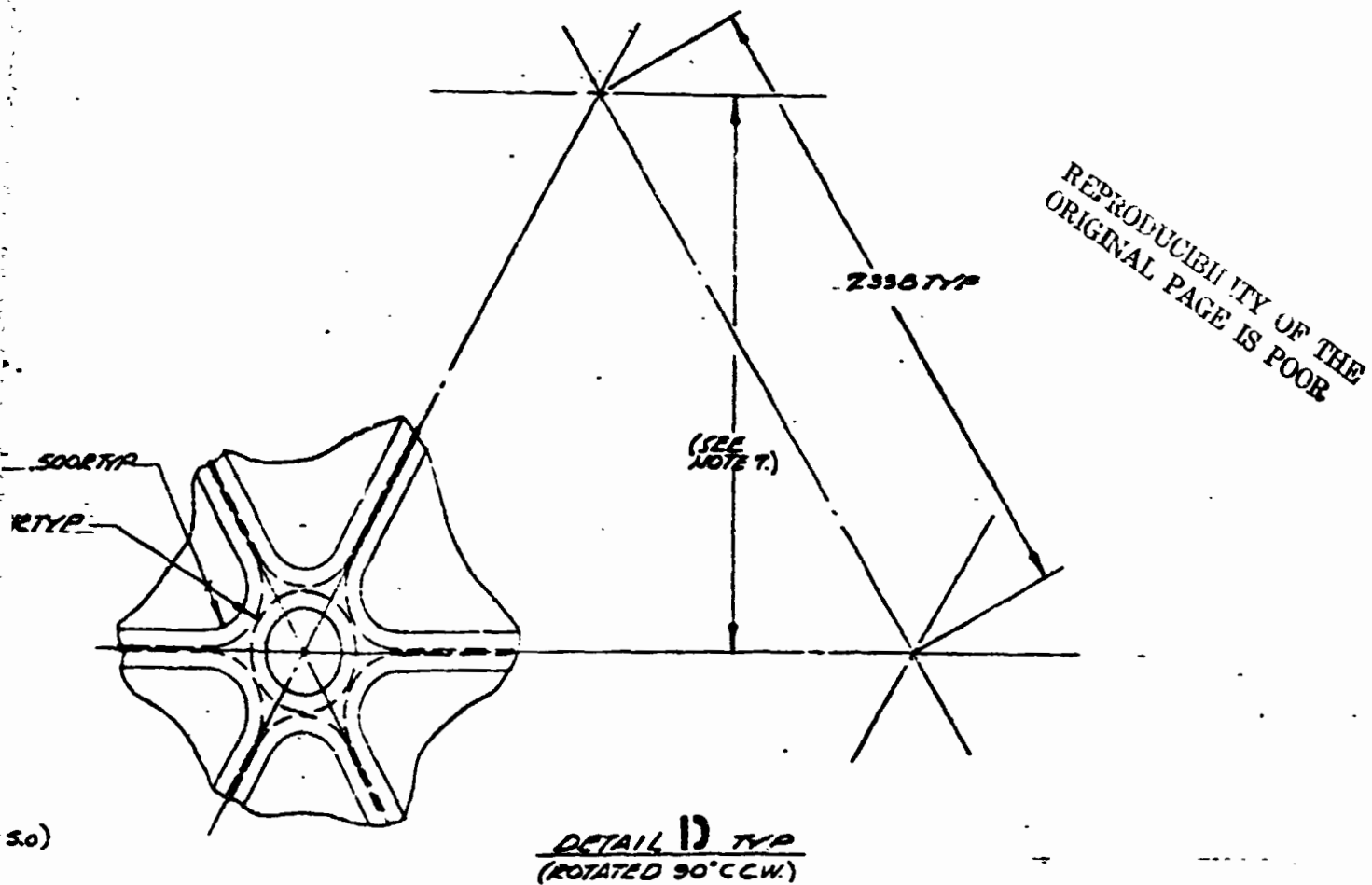


Figure C-1b. Isogrid Cylindrical Adapter

C.2.1 TEST SETUP AND INSTRUMENTATION

Figures C-2 to C-4 are views of the test setup and Figure C-5 identifies the configurations and locations of the instrumentation used on the adapter and loading fixture. It is noted from these figures that there are 24 hydraulic loading cylinders and load cells to apply and measure loads on upper and lower loading fixtures assembled on the test specimen. The specimen is instrumented with about 370 strain gages and 160 linear transducers. The strain gages measure grid member and skin stresses in the isogrid and flange transition areas of the adapter. The linear transducers measure radial deflections at selected nodes. In addition to the above, eight linear transducers measure movements of the upper loading fixture caused by load applications. The lower loading fixture is bolted to a rigid ground plane as is linear transducer support bracketry.

As seen in Figure C-3 the linear transducers for measuring axial displacements are located close to the bolted flange between the upper loading fixture and test specimen. All linear transducers were kept in place up to and including specimen failure. Maximum transducer error is ± 0.00035 inch.

The 24 loading cylinders act in 12 clevis assemblies as seen in Figure C-4. When a bending moment is to be applied the loading cylinders are programmed to apply loads that are nearly proportional to their distance from the axis about which the moment acts. This, in addition to an order of magnitude greater stiffness of loading fixtures compared to the stiffness of test specimen, causes the applied load to approximate perfect body bending.

As seen in Figure C-5 instrumentation is concentrated in the vicinity of the 0 circumferential station. This is the area where load peaking is generated and where initial specimen failure was expected.

There is one jack bolt, as per Figure C-6, in each transition at the upper and lower bolted flanges (Figure C-6). Nuts on these bolts are smugged up against the flanges to create direct load paths through the bolts and to minimize effects of flange bending or prying. Measured bolt tensile strength is 2100 lbs.

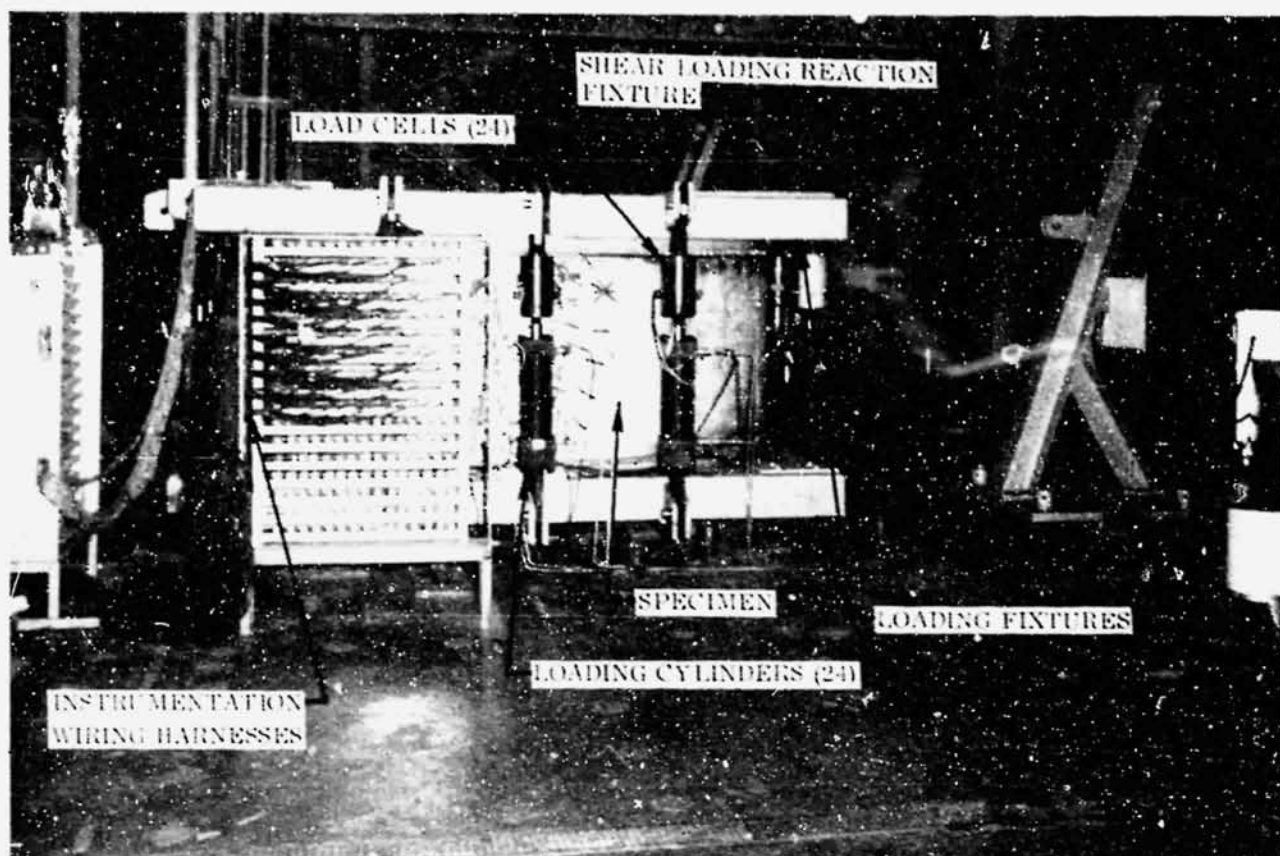


Figure C-2. View of test setup (side)

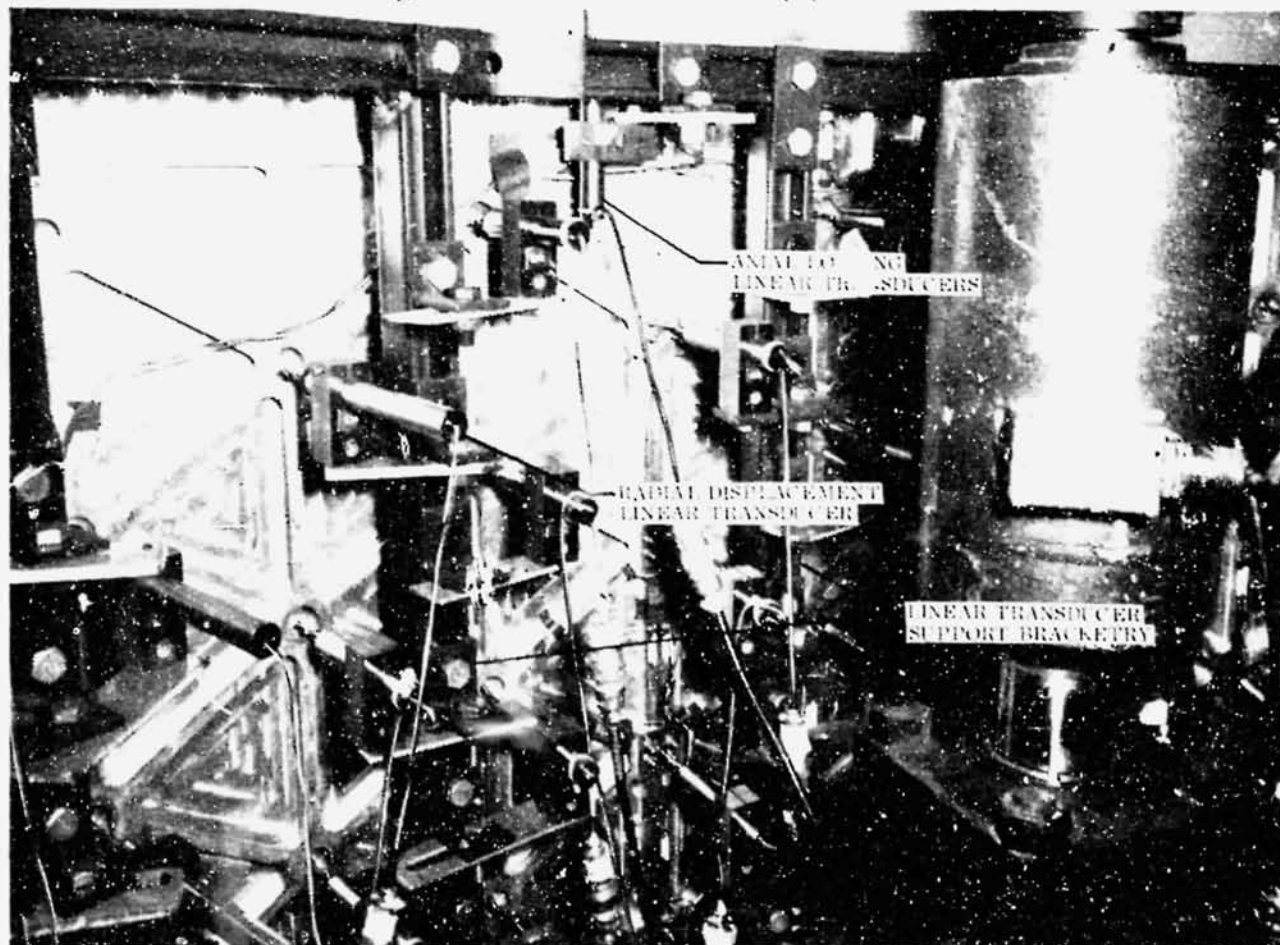


Figure C-3. Close up of instrumentation

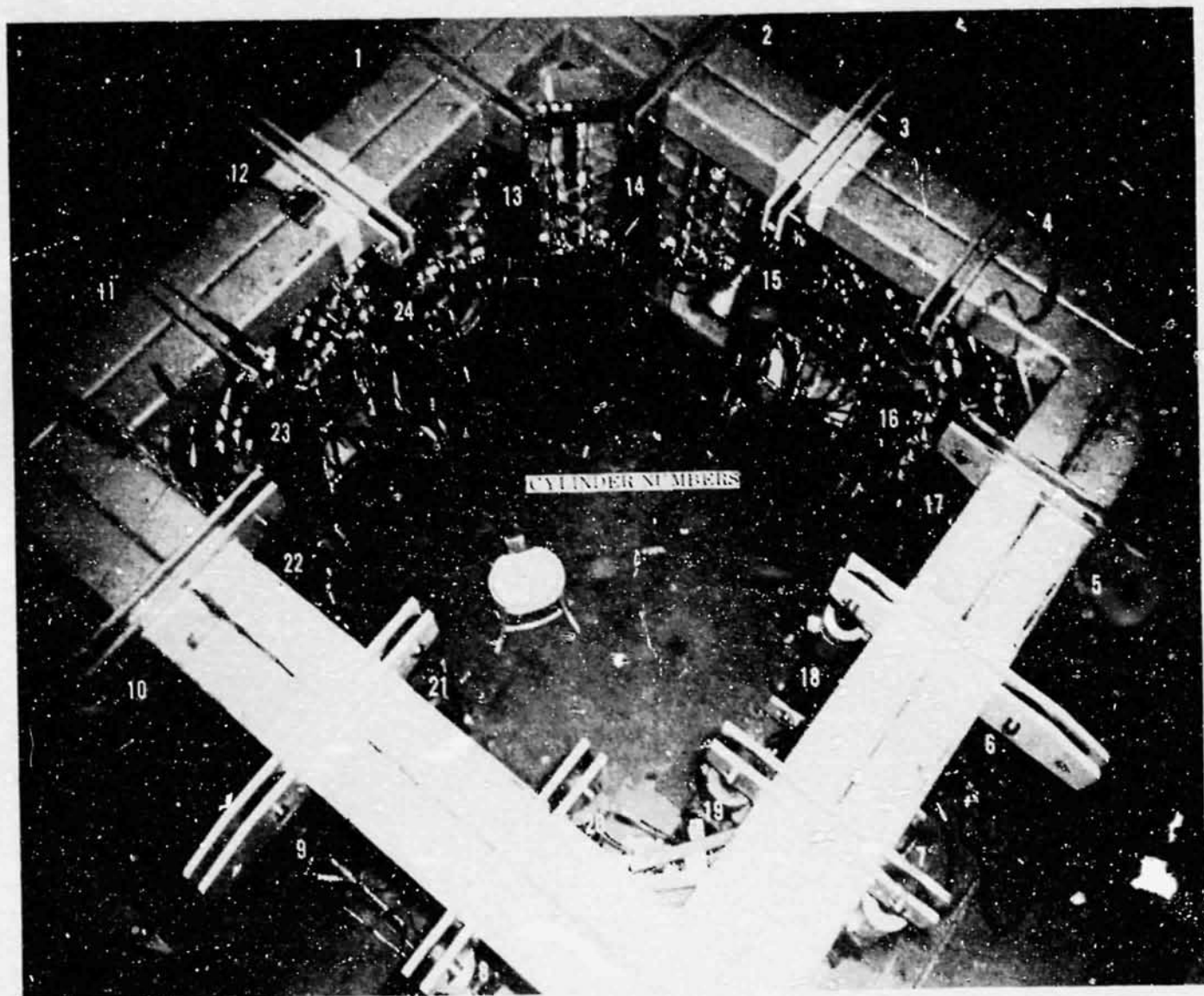
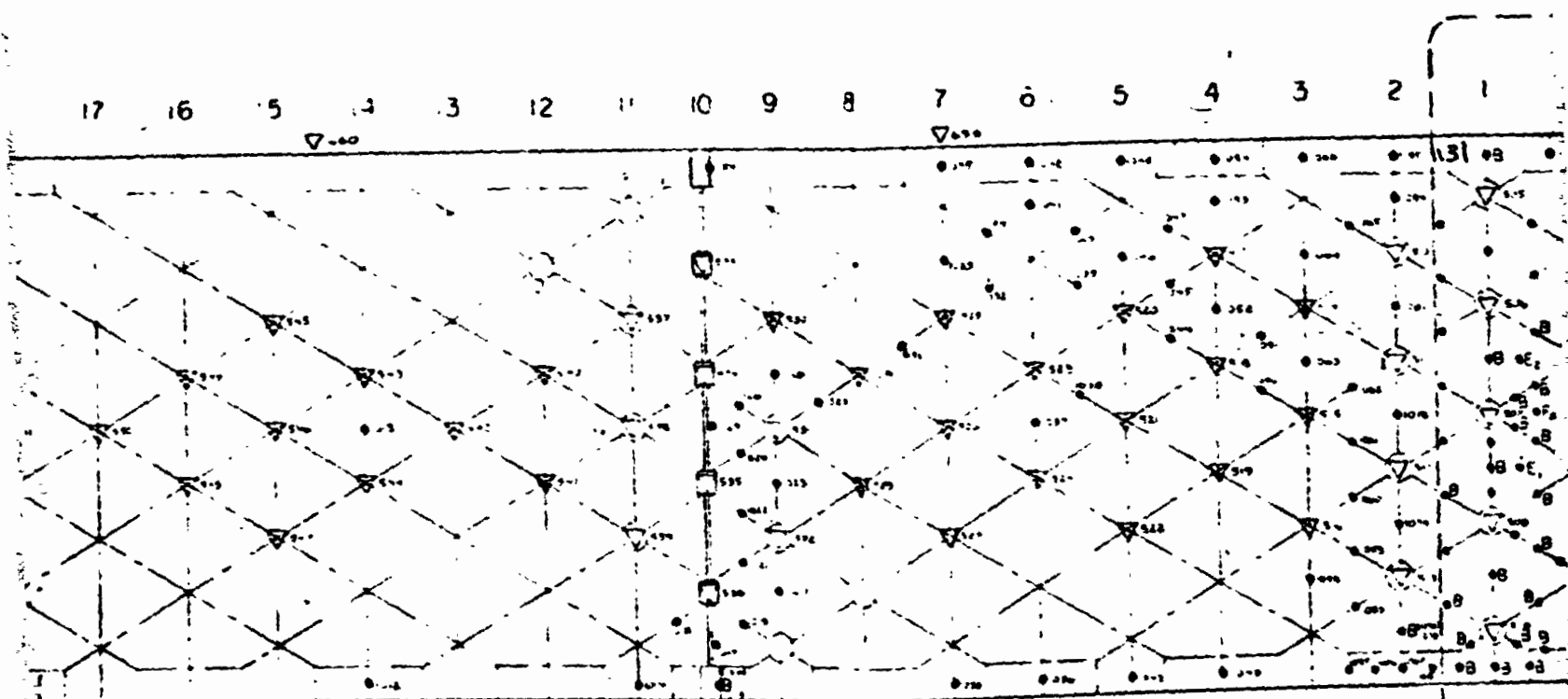


Figure C-4. View of test setup (top)

REPRODUCIBILITY OF THE
ORIGINAL PAGE IS POOR

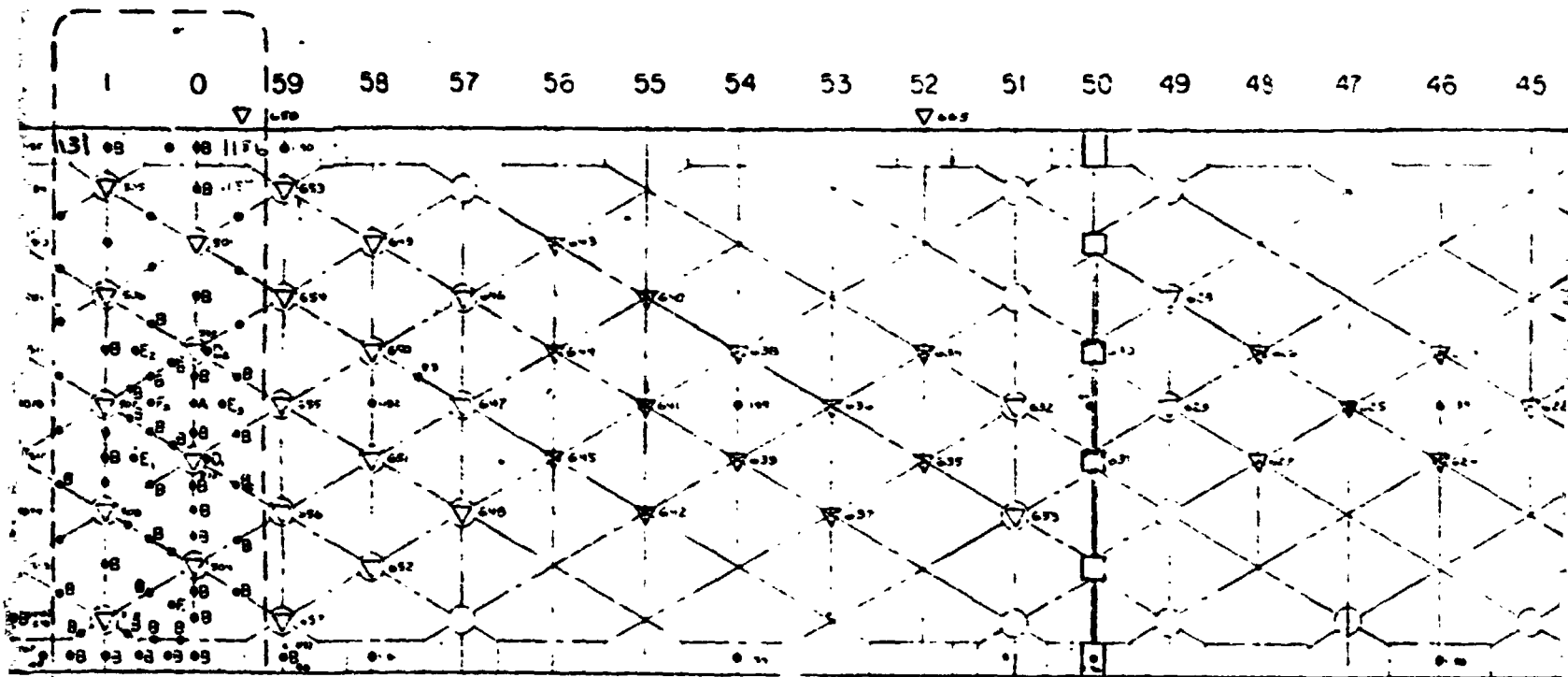


VIEW - OUT:

FOLDOUT FRAME

2

REPRODUCIBILITY OF THE
ORIGINAL PAGE IS POOR



DETAIL A
SEE SHEET 2

VIEW - OUTSIDE LOOKING IN

NOTES:

1. • INDICATES STRAIN GAGE LOCATIONS
2. ▽ INDICATES LINEAR TRANSDUCER LOCATIONS
3. STRAIN GAGE CONFIGURATION

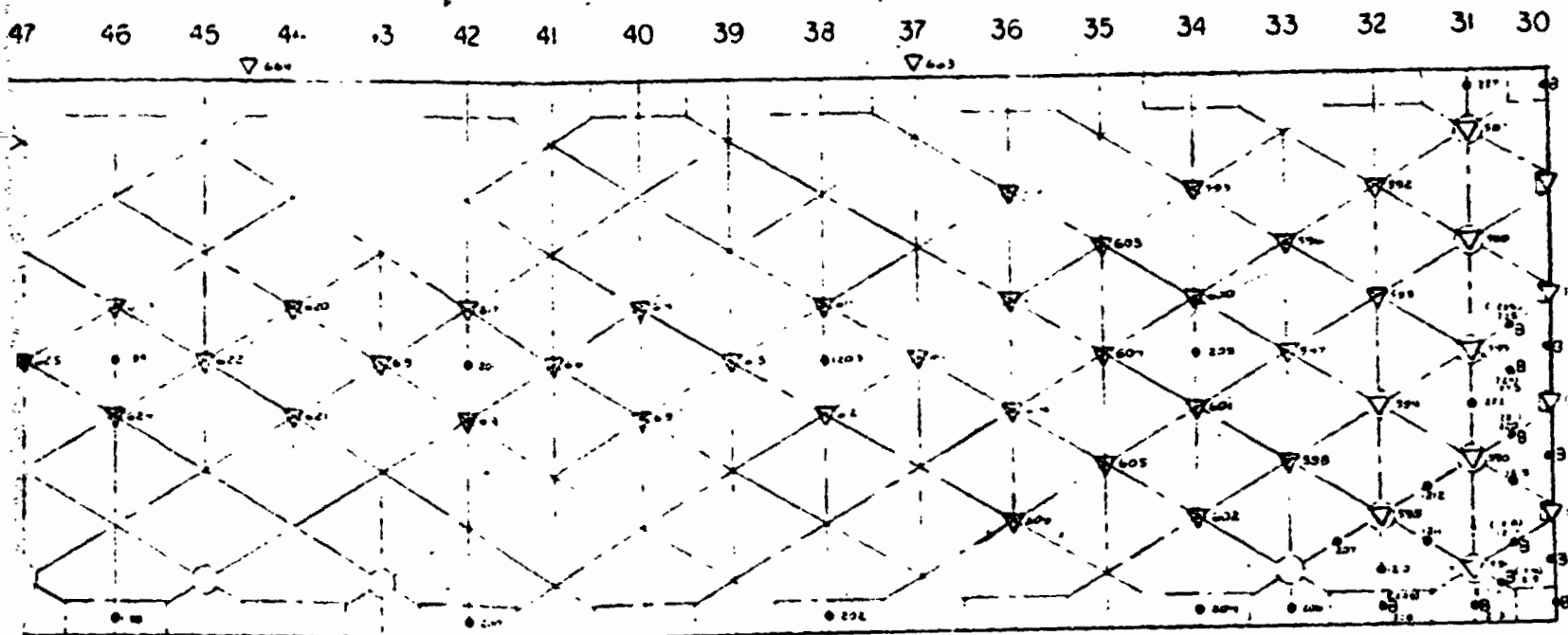
A AXIAL SEE EXAMPLE
B " " " "
C " " " "
D " " " "
E ROSETTE SEE DETAIL A
F " " " "

4. STRAIN GAGE CONFIGURATION "C" NOT MARKED
5. STRAIN GAGE NUMBERS IN () ARE LOCATED ON

FOLD-OUT FRAME

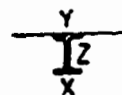
3

REPRODUCIBILITY OF THE
ORIGINAL PAGE IS POOR



MEASUREMENT NUMBERS

AXIAL: 1001 THRU 1240 ROSETTES: 3301 THRU 3162
RADIAL: 501 THRU 687 LONGITUDINAL: 650 THRU 665

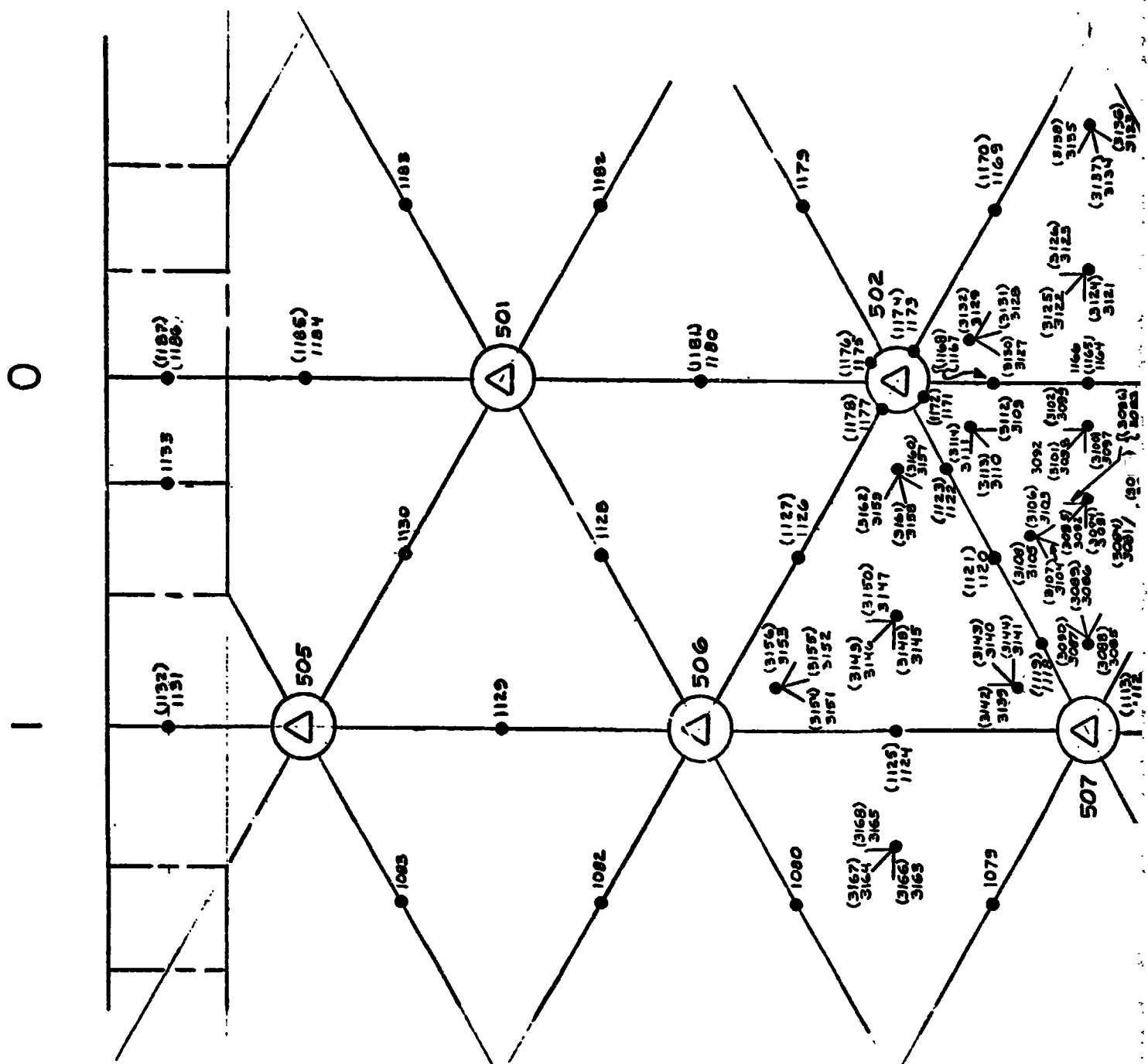


AXIAL			
STRAIN GAGE	Y	Y	Z
A	X	Y	Z
B	X	Y	
C	X		

STRAIN GAGES IN LINE
WITH GRID MEMBER

NOT MARKED
ARE LOCATED ON EXTERNAL SURFACE

Figure C-5a Instrumentation reference



REPRODUCIBILITY OF THE
ORIGINAL PAGE IS POOR

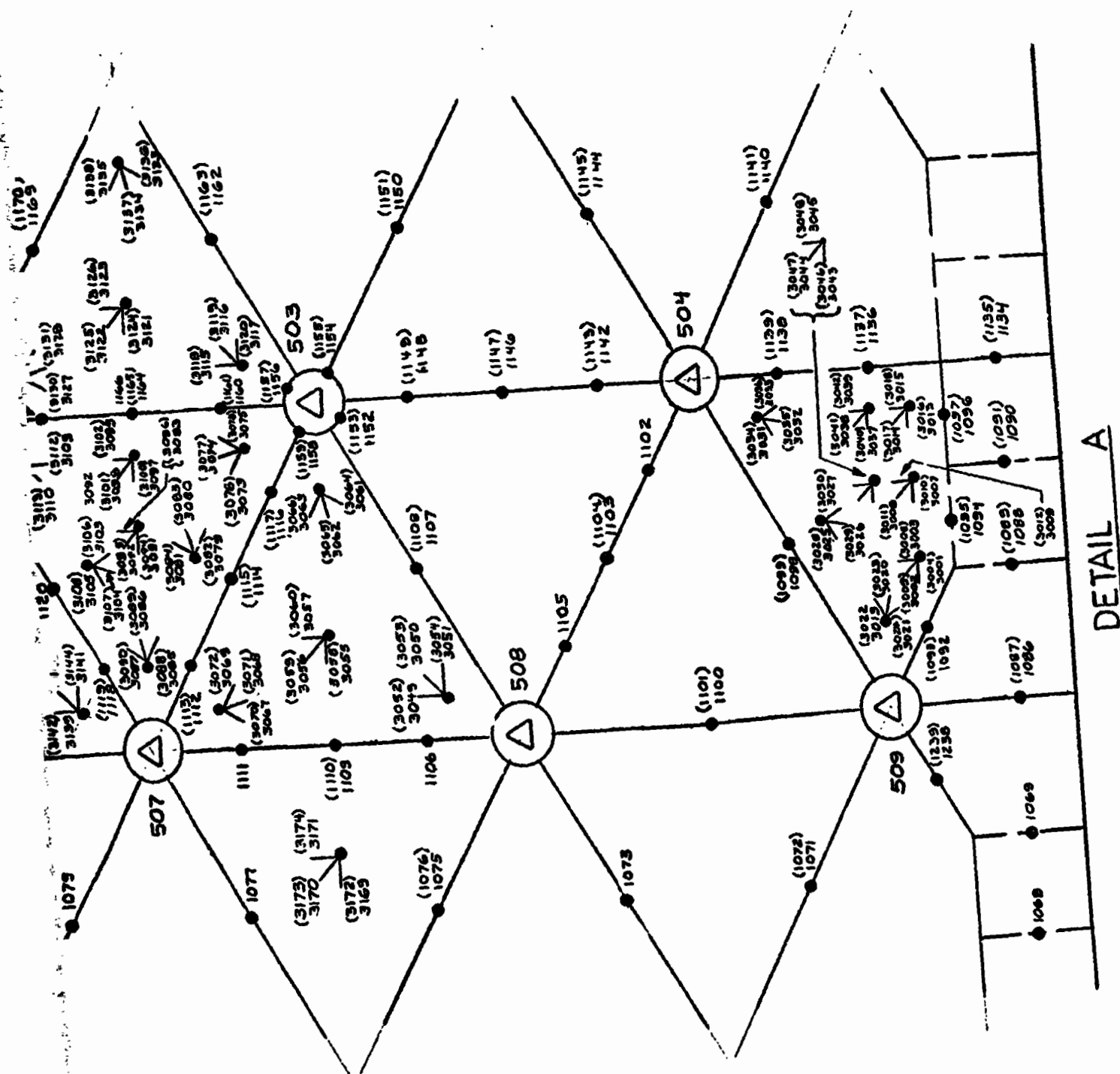


Figure C-5b Instrumentation Reference

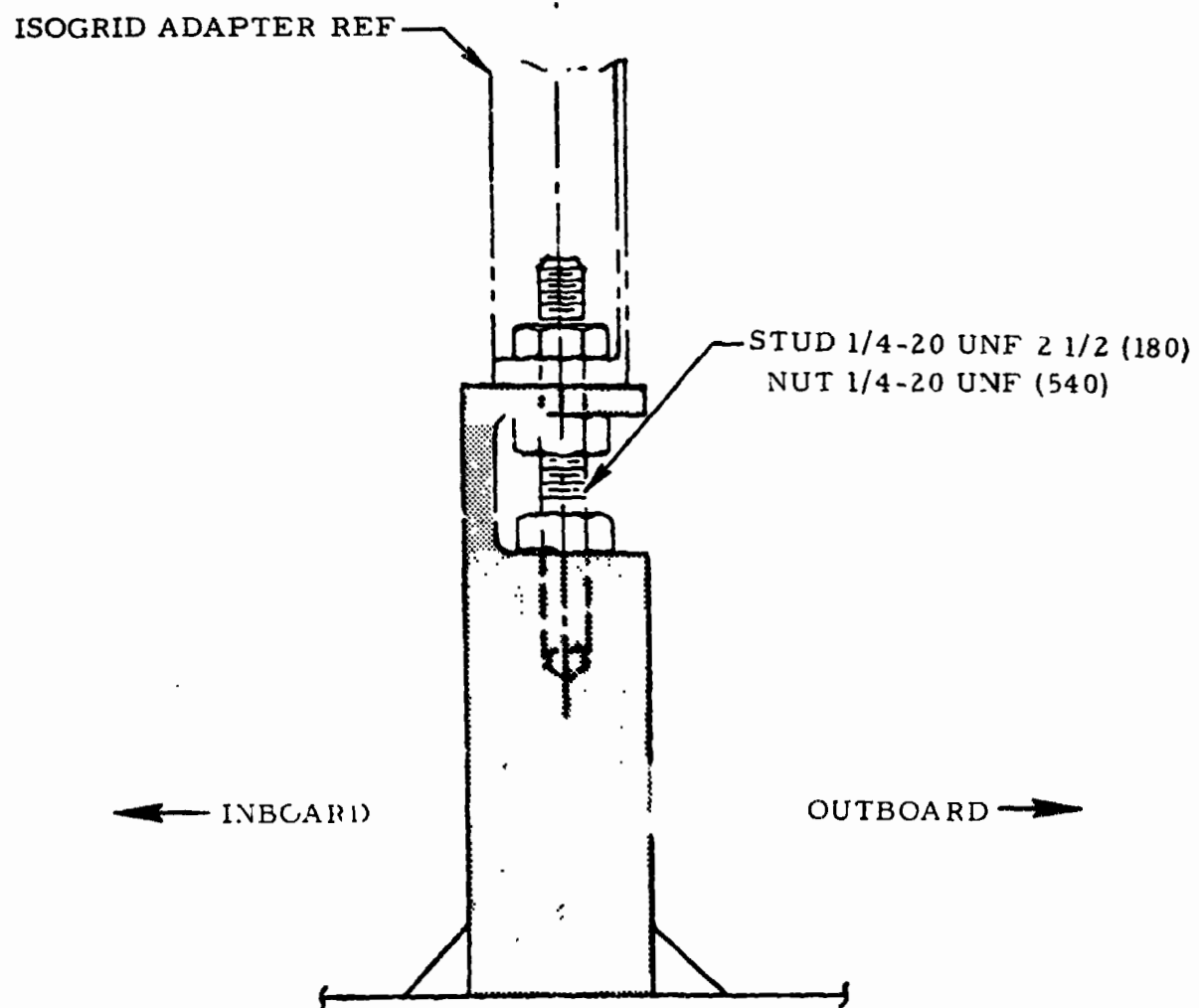


Figure C-6. Jack bolt in bolted flange

C.2.2 SPECIMEN FAILURE CONDITION

Figure C-7 shows the test specimen carrying 250% of the maximal load for the failure loading condition 9 (see Ref. C-1 for cylinder and load cell loads for this condition). Loading condition 9 includes combined axial and body bending loads to produce 636 lbs/in. specimen edge load intensity at circumferential station 0 for 100% nominal load. For the 250% nominal loading or 1590 lbs/in. edge intensity the wrinkles in the skin are on the order of 0.07-inch.

The specimen failed at close to 260% nominal load or 1654 lbs/in. Figure C-8 shows the failed specimen after it was removed from the loading fixture and Figure C-9 shows a close up of a typically failed area. Large deformation damage in this photograph is attributable to post buckling effects.

Initial failure probably occurred between circumferential Stations 54 and 7. Damage beyond these stations is due to sudden load relief in the initially failed area and inability of the loading system to dump applied loads quickly enough to avoid secondary damage.

Specimen failure was probably first sensed by a sudden loud report it created. This triggered a reaction in a matter of seconds by test personnel to dump load; however, this was not fast enough to avoid considerable secondary damage.

C.2.3 INSPECTION OF DAMAGED SPECIMEN

Figure C-10 diagrams damaged areas of the test specimen to indicate failed grid members and directions of structural deformations near damaged areas. Figure C-10 also lists measured or estimated grid-member and skin cross sectional dimensions in damaged areas.

C.2.4 STRESSES IN FAILED GRID MEMBERS

Figures C-11a to C-11d are plots of actual or representative inner flange stresses vs. percent load in some of the longitudinal failed grid members indicated on Figure C-10. Presented plots are based on availability of inner flange strain gage data. Since anticipation of all failed members was impossible, strain gage data is not available for many failed members. Strain gage numbers and corresponding

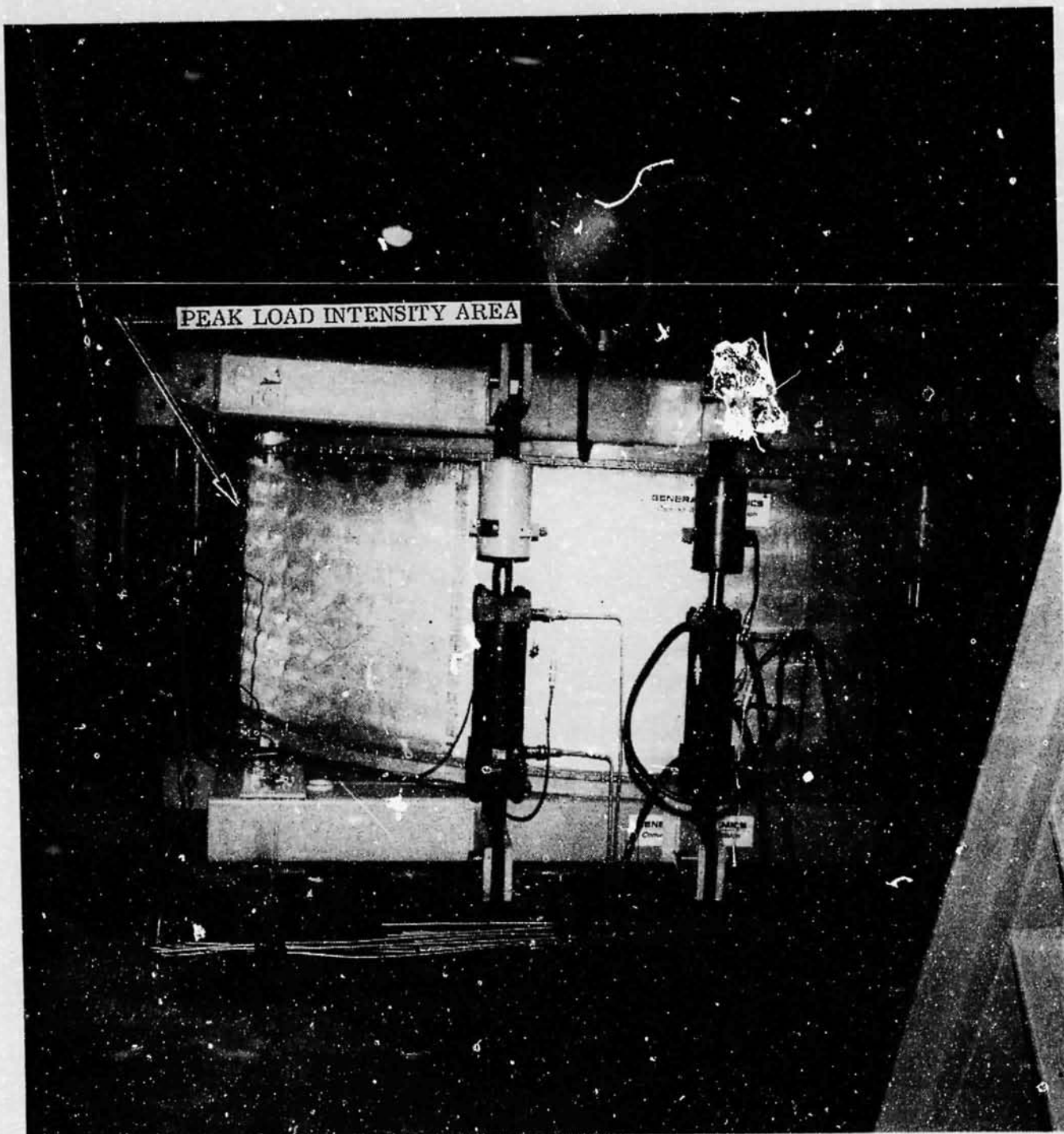


Figure C-7. Specimen near failure

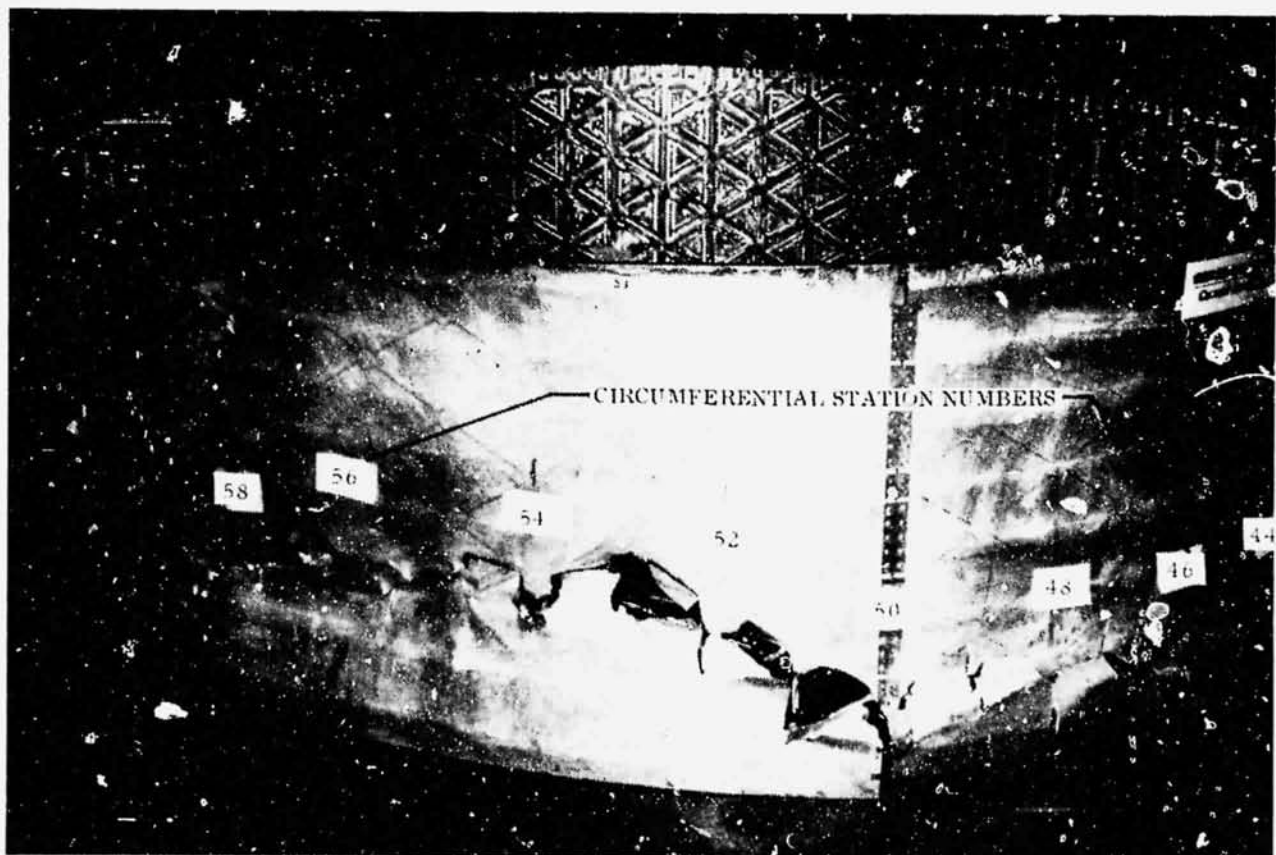
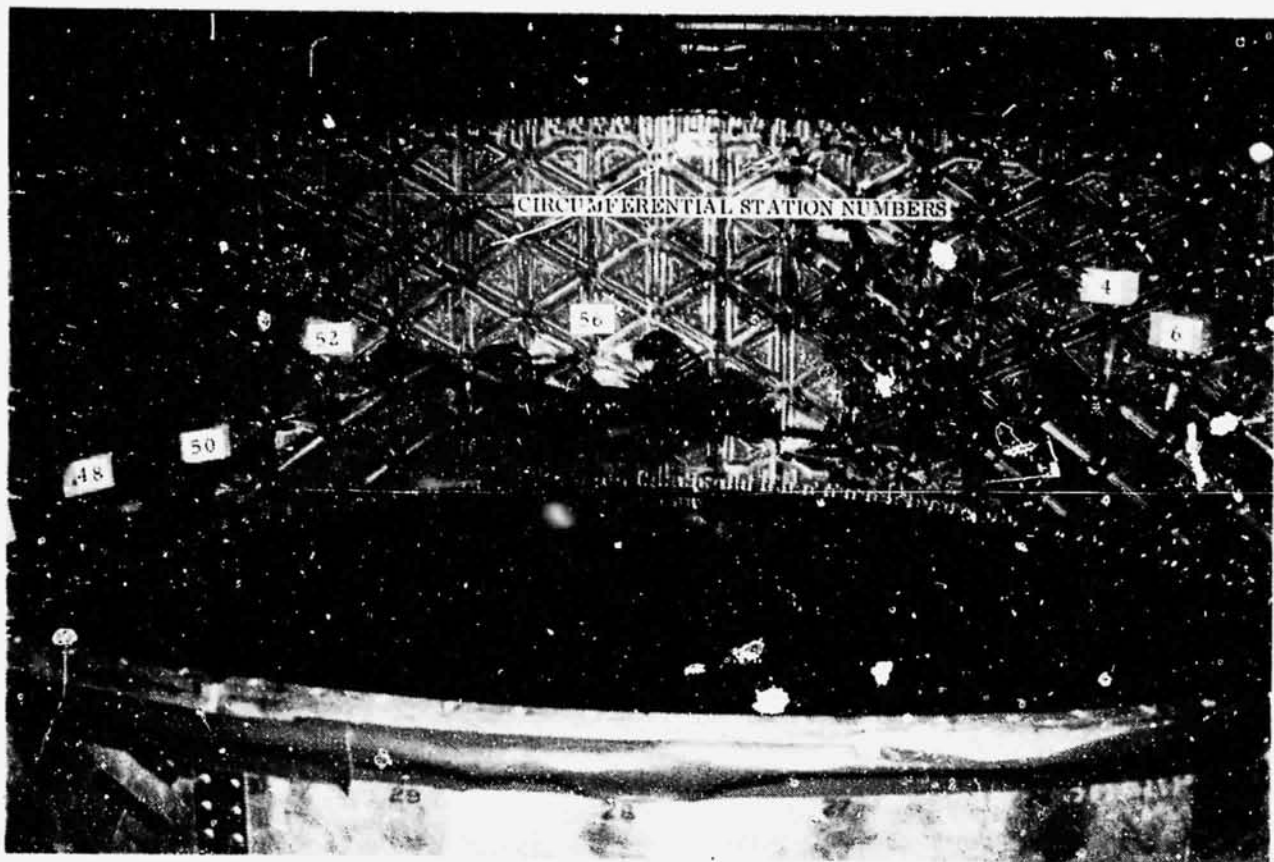


Figure C-8. Failed specimen
C-12

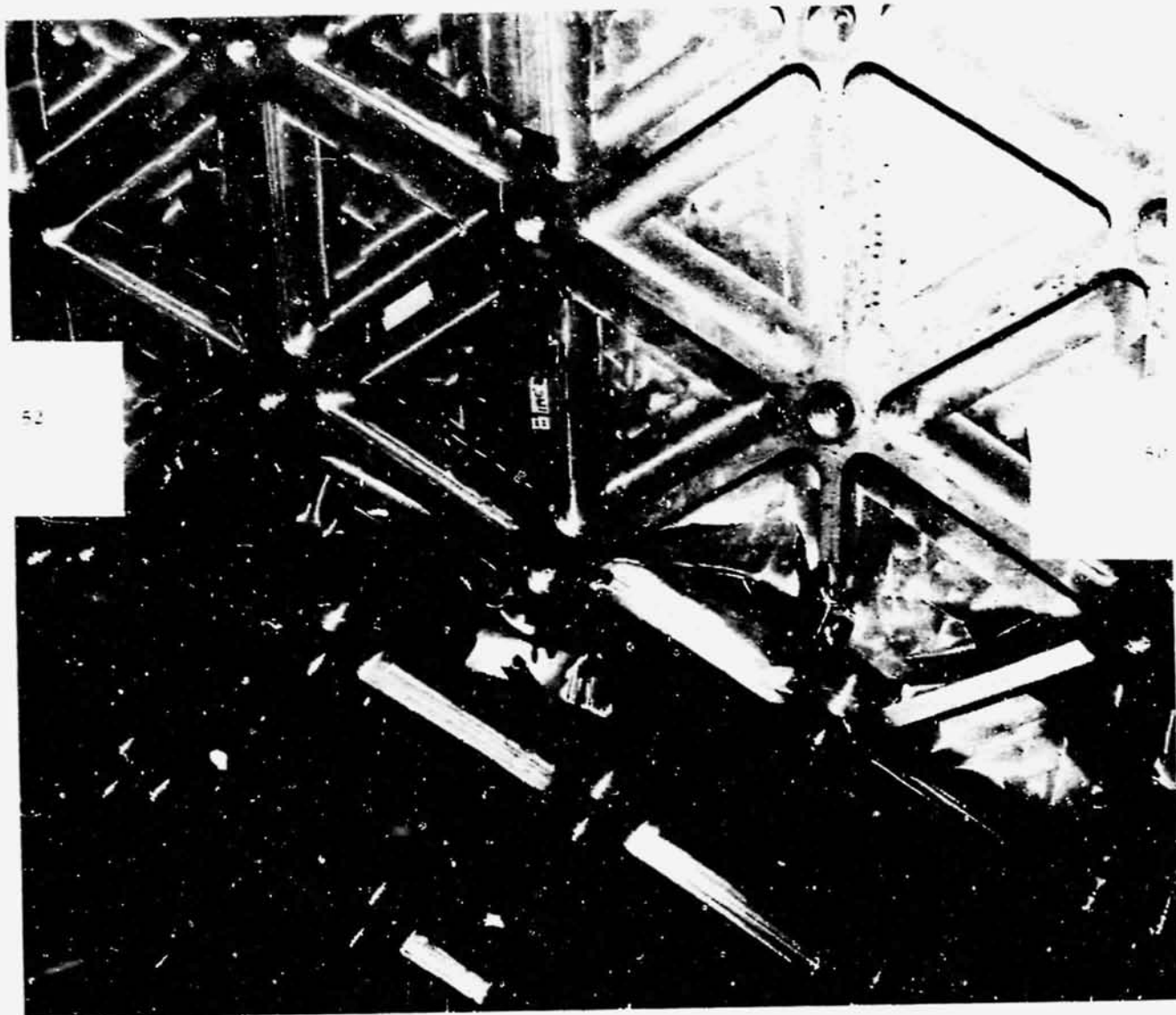
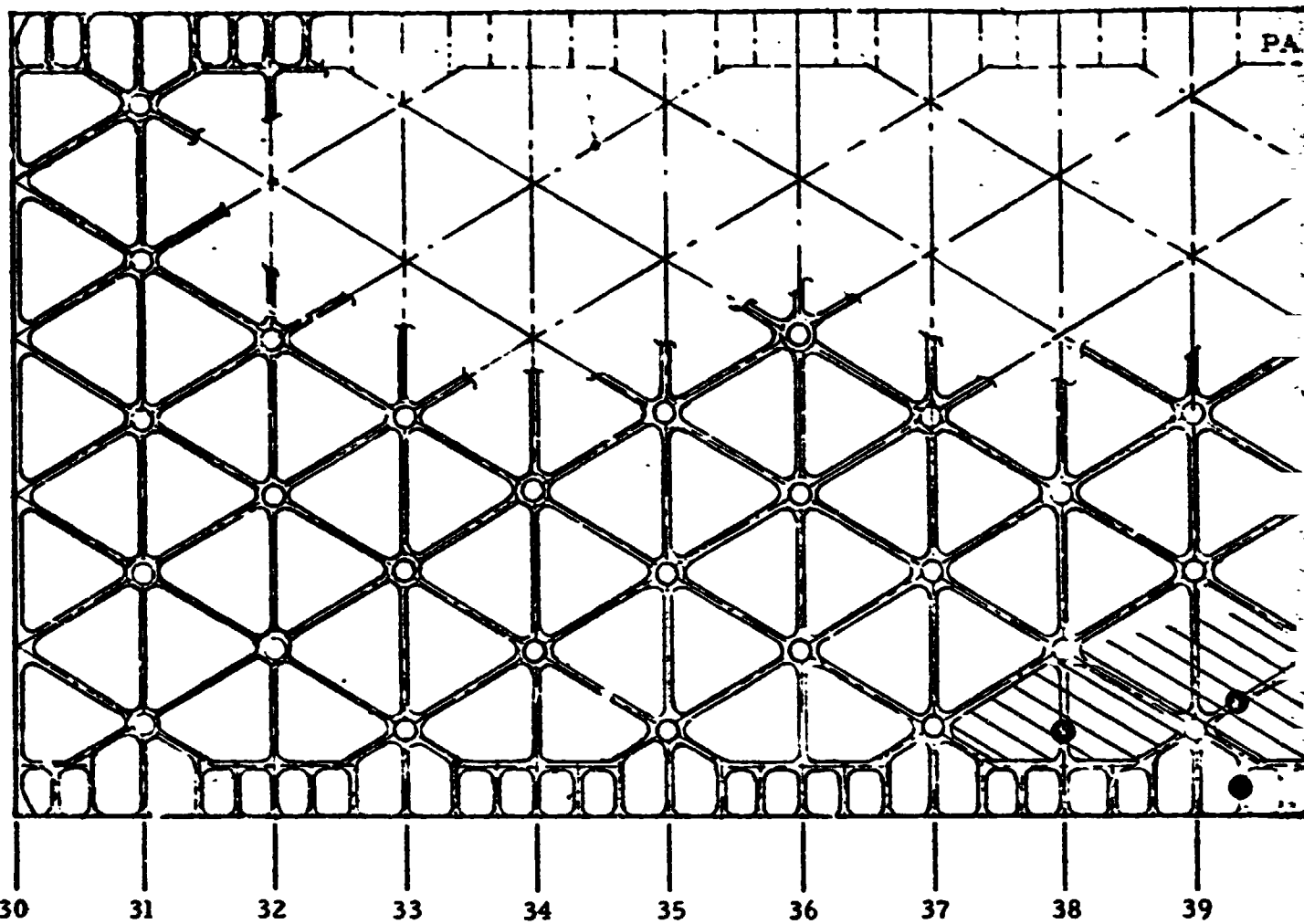
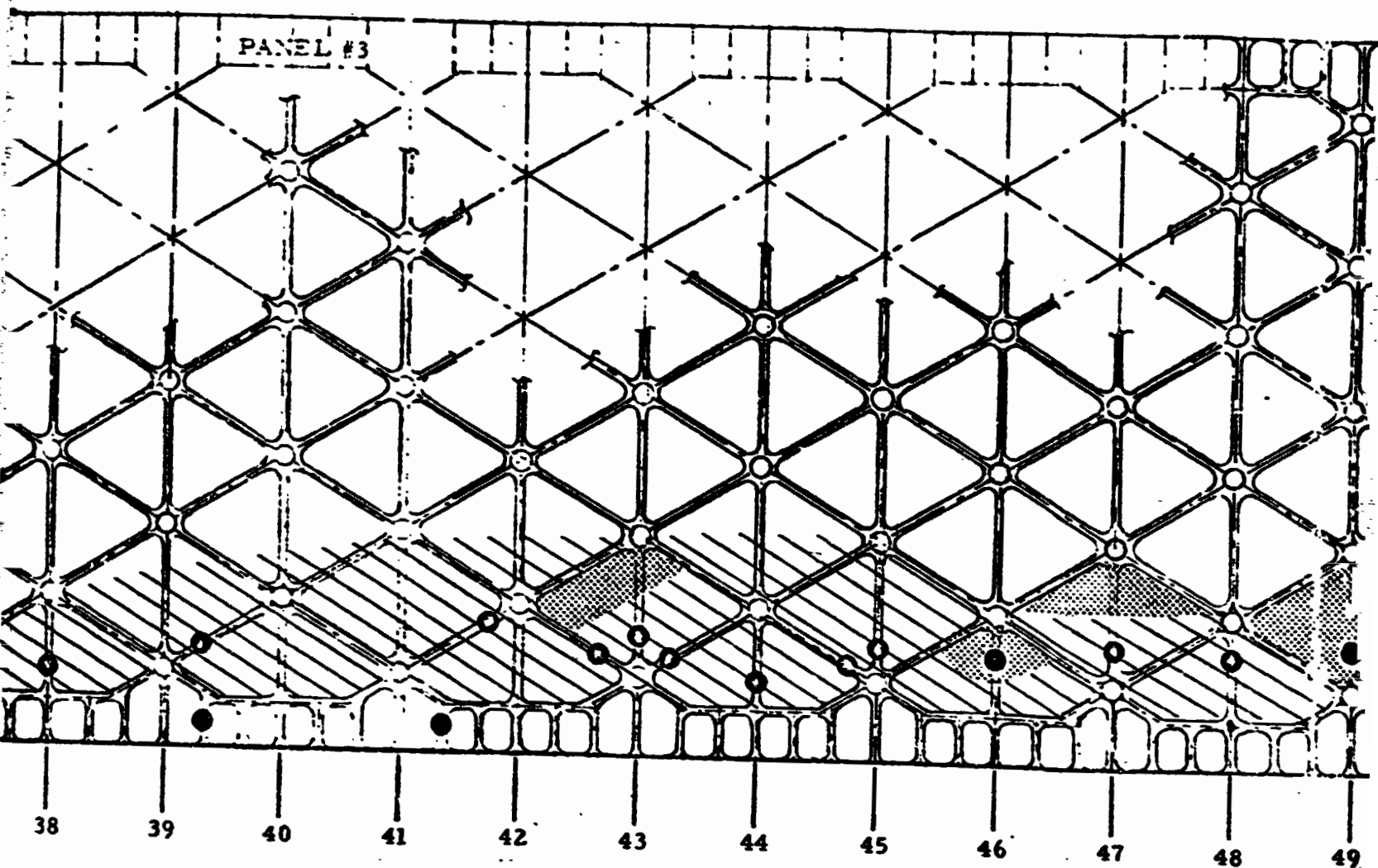


Figure C-9. Close up of typically failed area



REPRODUCIBILITY OF THE
ORIGINAL

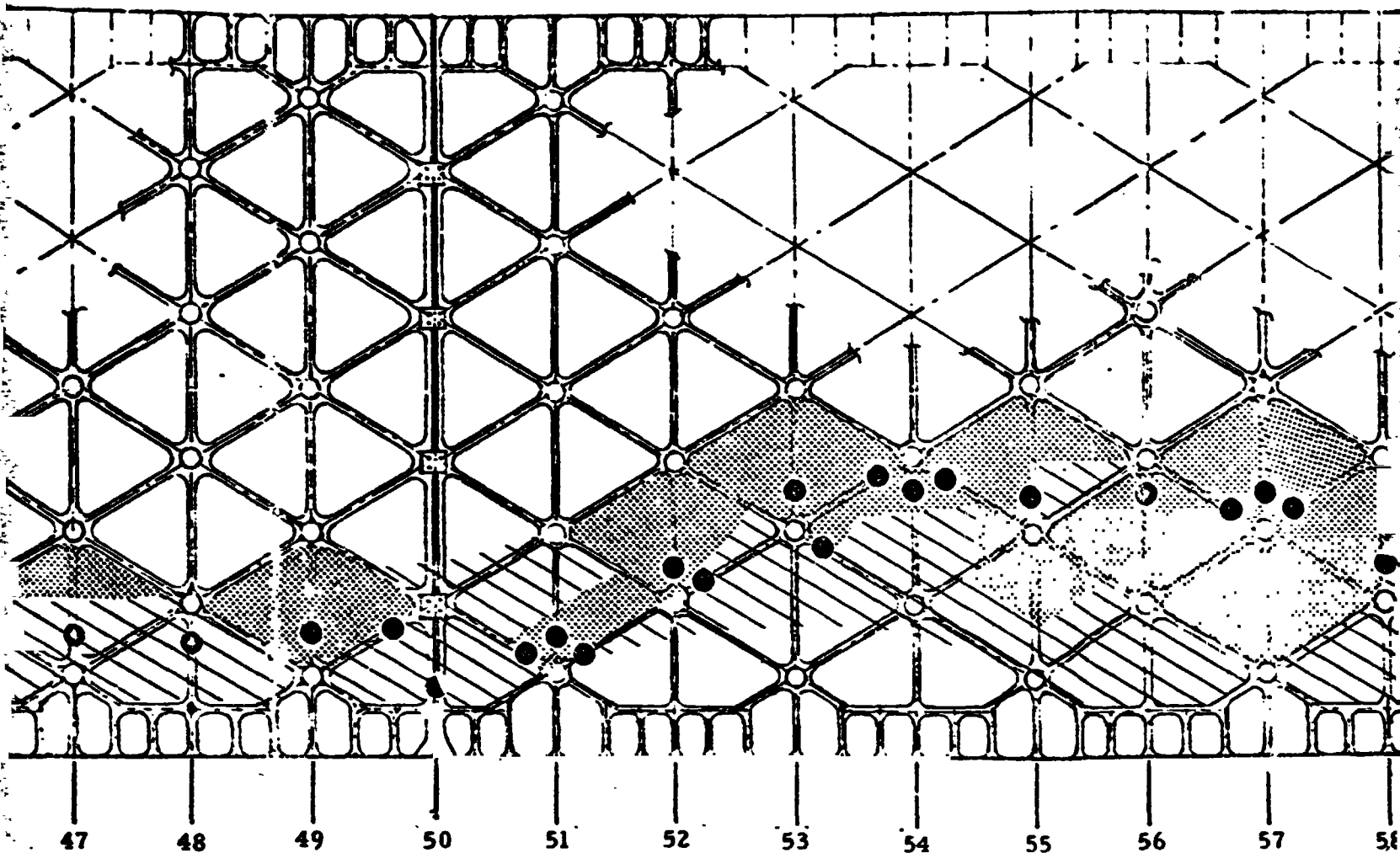
FOLDOUT FRAME



REPRODUCIBILITY OF THE
ORIGINAL PAGE IS POOR

No.	w	c
49	.420	.0
48	.420	.0
47	.420	.0
46	.410	.0
45	.410	.0
44	.410	.0
43	.420	.0
42	.408	.0
41	.408	.0
40	.415	.0
39	.415	.0
38	.415	.0

FOLDOUT FRAME

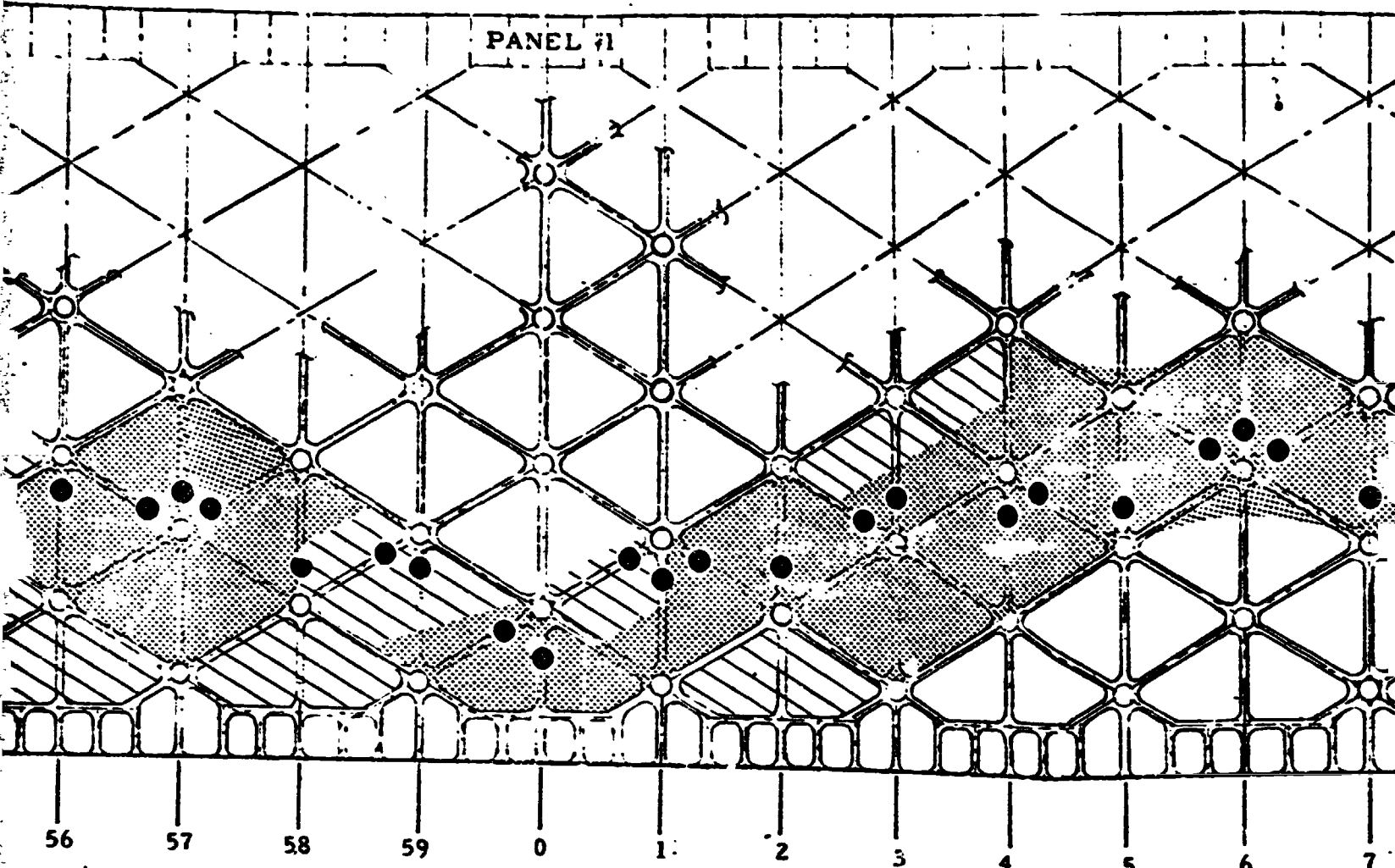


PANEL #3						
No.	w	c	b1	b2	t1	t2
49	.420	.086	.059	.086	.040	.057
48	.420	.086	.059	.086	.040	.057
47	.420	.086	.059	.086	.040	.057
46	.410	.079	.043	.074	.035	.055
45	.410	.079	.043	.074	.035	.055
44	.410	.079	.043	.074	.035	.055
43	.420	.085	.060	.088	.040	.060
42	.408	.085	.060	.088	.040	.060
41	.408	.085	.060	.088	.040	.060
40	.415	.085	.055	.085	.037	.057
39	.415	.085	.055	.085	.037	.057
38	.415	.085	.055	.085	.037	.057

PANEL #1						
No.	w	c	b1	b2	t1	t2
50	.260	.083	.055	.065	.037	.059
51	.420	.082	.053	.081	.035	.056
52	.420	.082	.053	.081	.035	.056
53	.414	.080	.042	.074	.037	.059
54	.420	.089	.057	.085	.038	.058
55	.420	.089	.057	.085	.037	.059
56	.419	.080	.055	.084	.036	.057
57	.415	.090	.048	.076	.037	.057
58	.411	.089	.044	.075	.037	.051
59	.412	.085	.047	.076	.038	.057
0	.411	.079	.047	.075	.088	.053
1	.415	.085	.055	.085	.038	.057
2	.408	.082	.041	.072	.036	.052
3	.420	.079	.060	.088	.040	.060
4	.420	.079	.060	.088	.040	.060
5	.420	.079	.060	.088	.040	.060
6	.410	.086	.043	.074	.035	.055
7	.420	.083	.059	.086	.040	.057
8	.420	.083	.059	.086	.040	.057
9	.420	.083	.059	.086	.040	.057
10	.260	.083	.055	.065	.037	.059

FOLDOUT FRAME

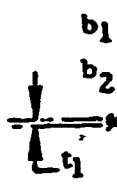
PANEL #1



#1			
	b ₂	t ₁	t ₂
	.065	.037	.059
	.081	.035	.056
	.081	.035	.056
	.074	.037	.059
	.085	.038	.058
	.085	.037	.059
	.084	.036	.057
	.076	.037	.057
	.075	.037	.051
	.076	.038	.057
	.075	.088	.053
	.085	.038	.057
	.072	.036	.052
	.088	.040	.060
	.088	.040	.060
	.088	.040	.060
	.074	.035	.055
	.086	.040	.057
	.086	.040	.057
	.086	.040	.057
	.065	.037	.059

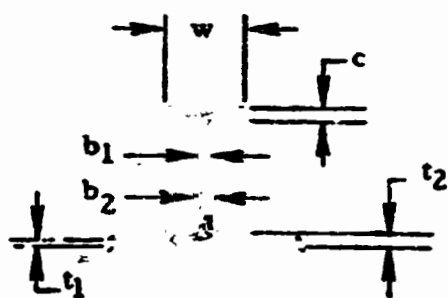
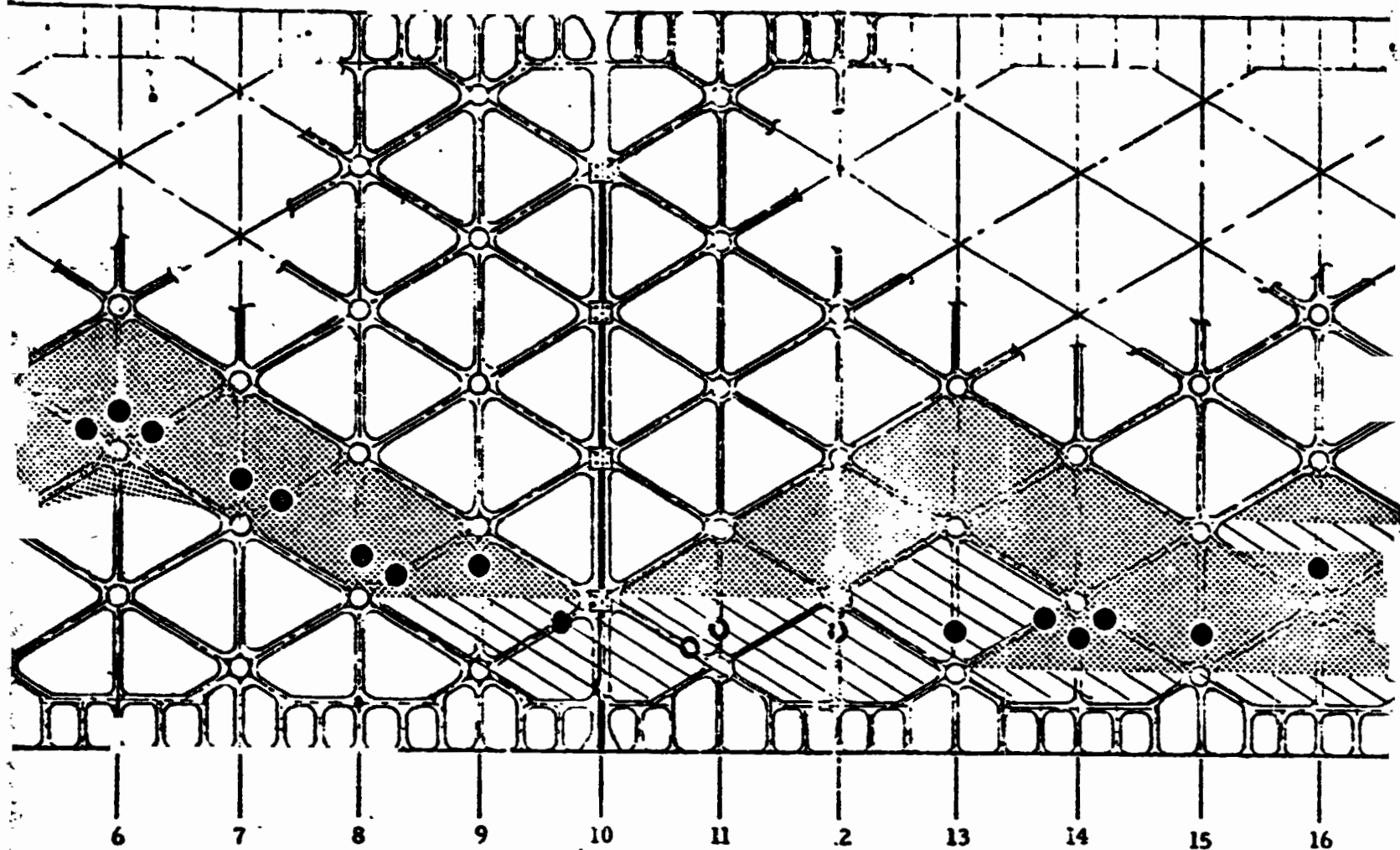
PANEL #2						
No.	w	c	b ₁	b ₂	t ₁	t ₂
11	.416	.037	.058	.086	.037	.055
12	.416	.037	.058	.086	.037	.055
13	.416	.037	.058	.086	.037	.055
14	.416	.037	.058	.086	.037	.055
15	.415	.037	.058	.087	.038	.058
16	.415	.037	.058	.087	.038	.058

REPRODUCIBILITY OF THE
ORIGINAL PAGE IS POOR

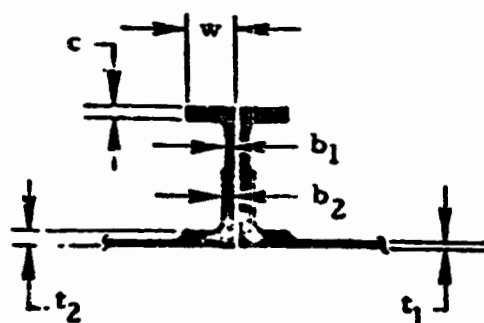


GRID S

OLDOUT FRA



GRID SECTION(TYPICAL)

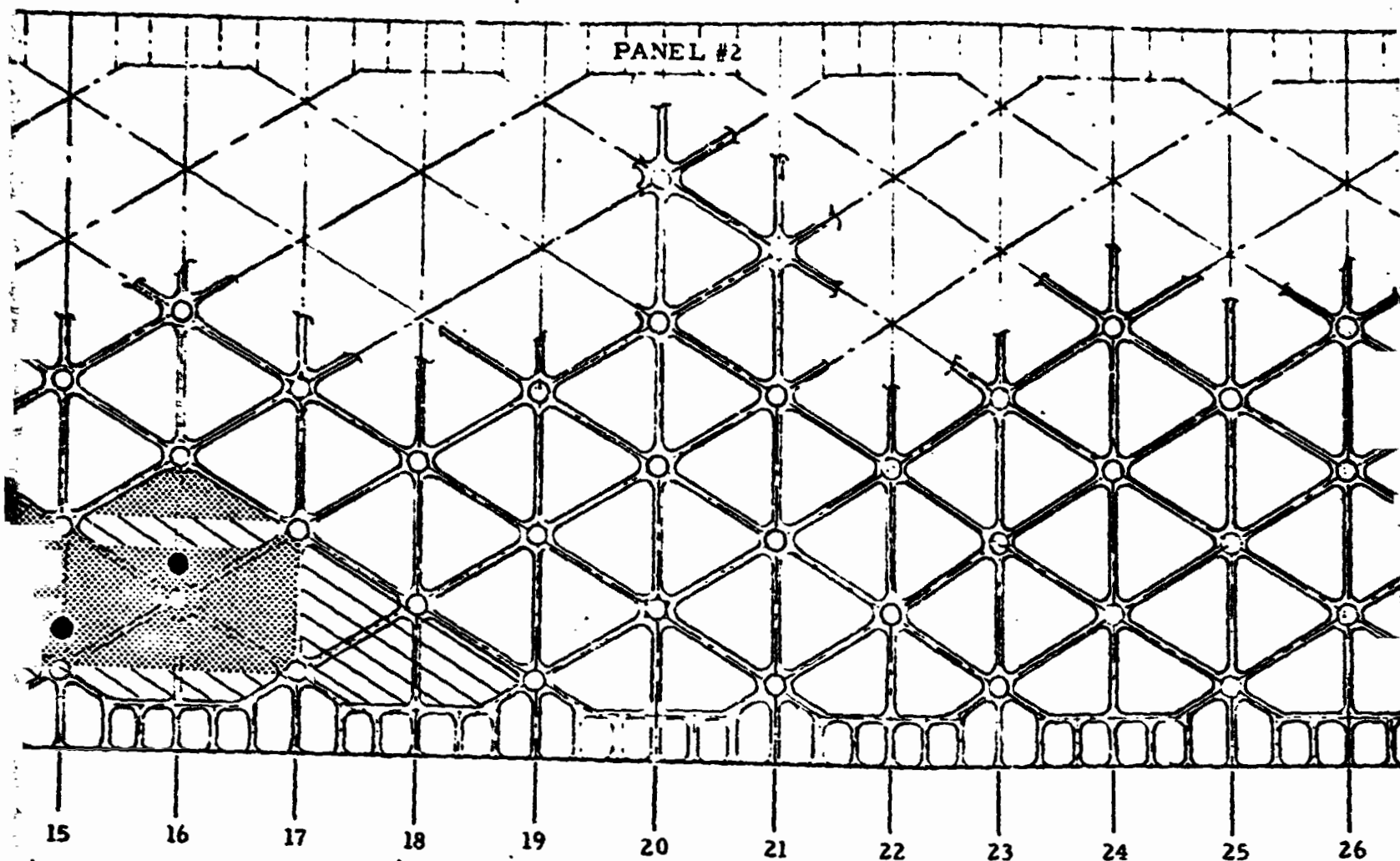


EDGE SECTION(TYPICAL)

REPRODUCIBILITY OF THE
ORIGINAL PAGE IS POOR

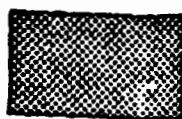
REPRODUCIBILITY OF THE
ORIGINAL PAGE IS POOR

5



SYMBOLS

● GRID FAILURE (SEE TABLE FOR DIMENSIONS OF CROSS SECTION)

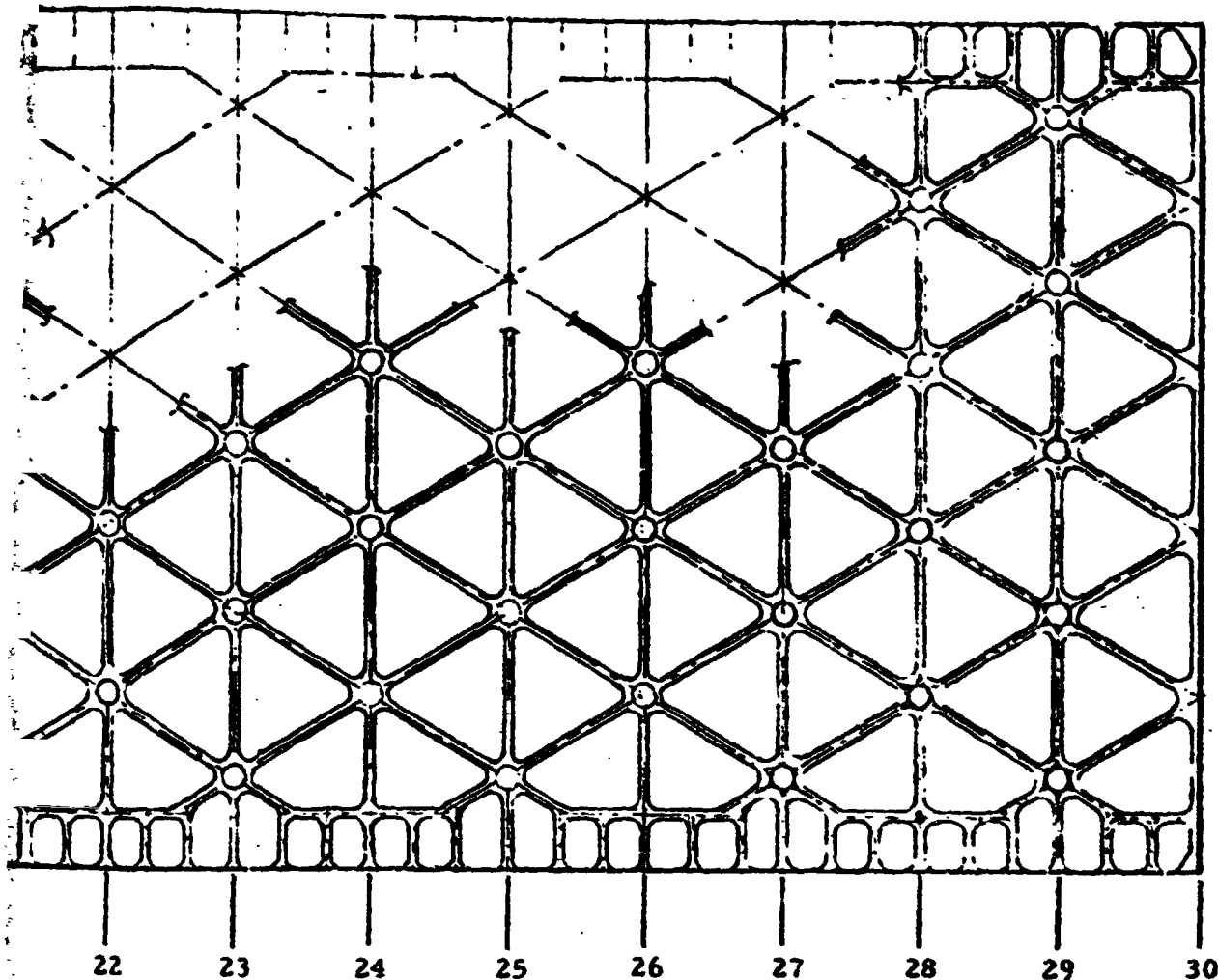


INBOARD FAILURE



OUTBOARD FAILURE

6



SYMBOLS

● GRID FAILURE (SEE TABLE FOR DIMENSIONS OF CROSS SECTION)



INBOARD FAILURE



OUTBOARD FAILURE

REPRODUCIBILITY OF THE
ORIGINAL PAGE IS POOR

FOLDOUT FRAME

Figure C-10. Inspection reference.

7

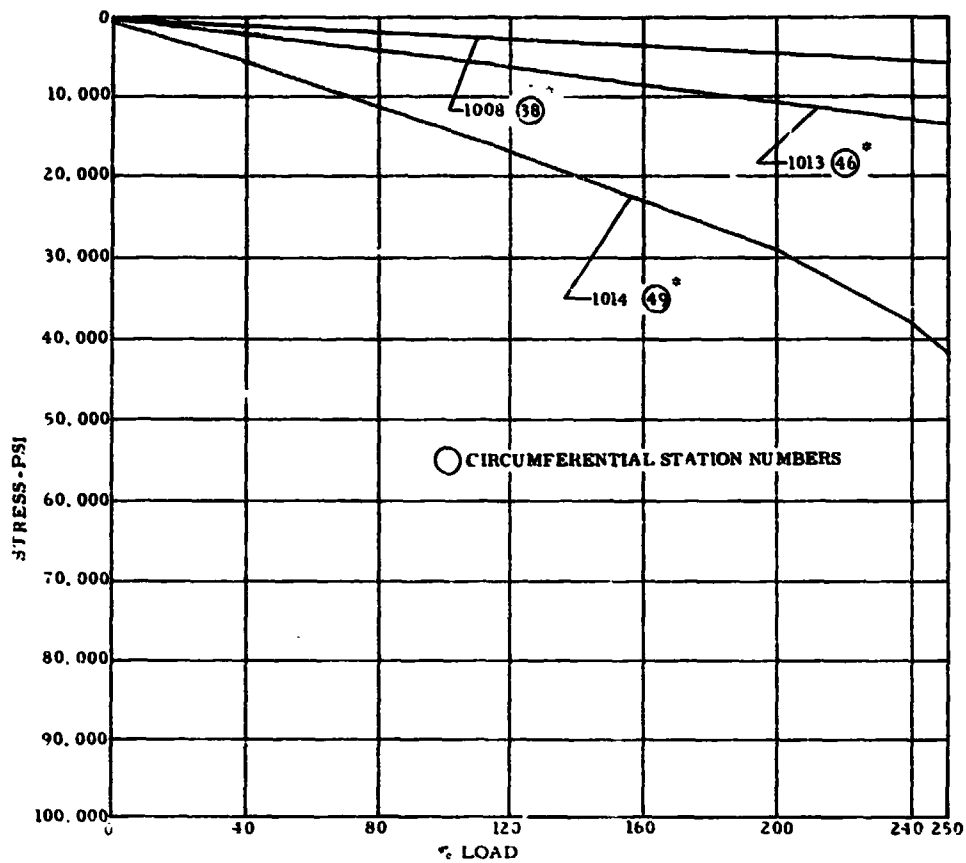


Figure C-11a. Stresses in failed grid members (longitudinal)

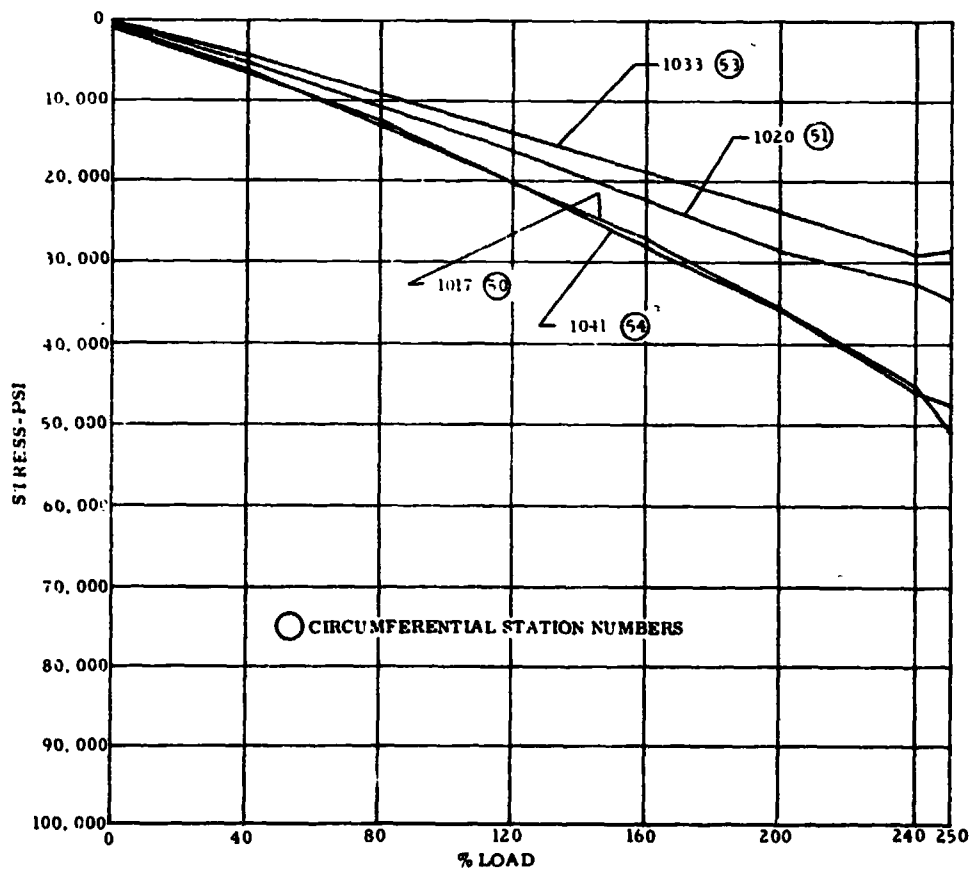


Figure C-11b. Stresses in failed grid members (longitudinal)

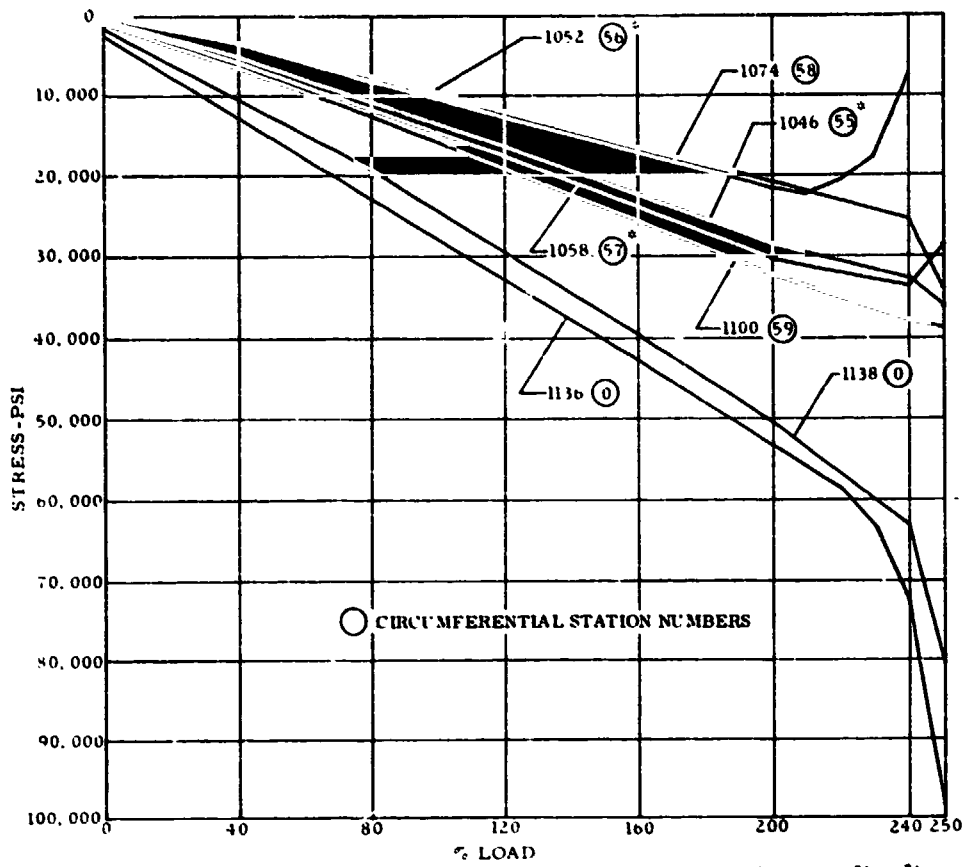


Figure C-11c. Stresses in failed grid numbers (longitudinal)

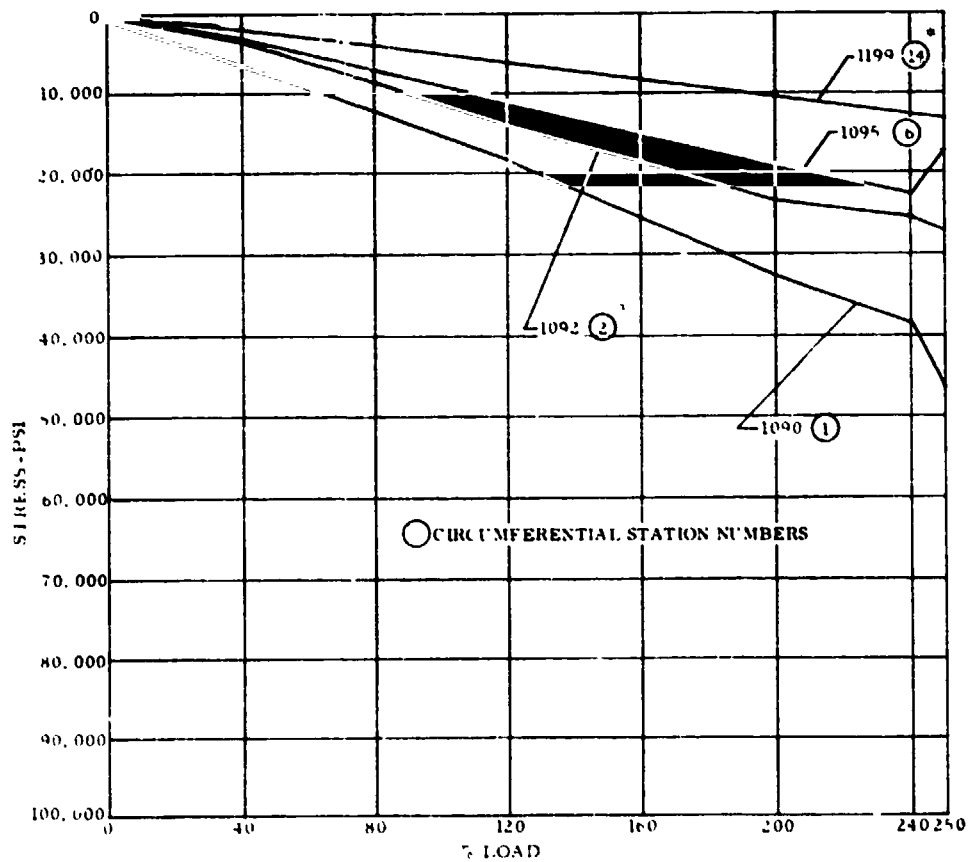


Figure C-11d. Stresses in failed grid members (longitudinal)

circumferential station numbers (per Figure C-5) are labeled with an asterisk in Figures C-10a to C-10d to indicate that stresses are for members representative of, but not the actual, failed grid member. When available these representative strain gages are chosen to have positions with respect to the upper bolted flange that are symmetrical with positions of failed grid with respect to the lower bolted flange. The tabulated cross sectional properties of failed grid members are average values based on the labeled representative grid members.

Figure C-12 shows plots of available measured stresses vs. percent load in failed diagonal grid members.

Figures C-11 and C-12 indicate different degrees of stress peaking or relief with load in the last 10 percent of load increment. From these plots the most likely candidate for having precipitated general instability is the failed grid member at circumferential Station 0. Apparently as seen in Figure C-11c this member is experiencing severe inelastic deformation in the last 10 percent load increment (i. e., stress exceeds the 61,000 psi yield stress of 2024-T851 aluminum). This is not a certain cause of general instability since there are other measurements of comparable and considerably greater plastic deformation in areas showing no fractures.

C. 2.5 STRESSES NEAR PEAK LOAD INTENSITY AREA

Axial load (F) and bending moment (M) in a grid member cross section is computed from simultaneous solution of the following equations:

$$-S_1 = \frac{MC_o}{I} + \frac{F}{A} \quad (2-1)$$

and

$$-S_2 = \frac{M(s-C_o)}{I} + \frac{F}{A} \quad (2-2)$$

where

S_1, S_2 are respectively measured stresses on the inner flange and outer flange on skin side,

C_o distance from neutral axis of grid member I-beam cross section to extreme fiber on inner flange,

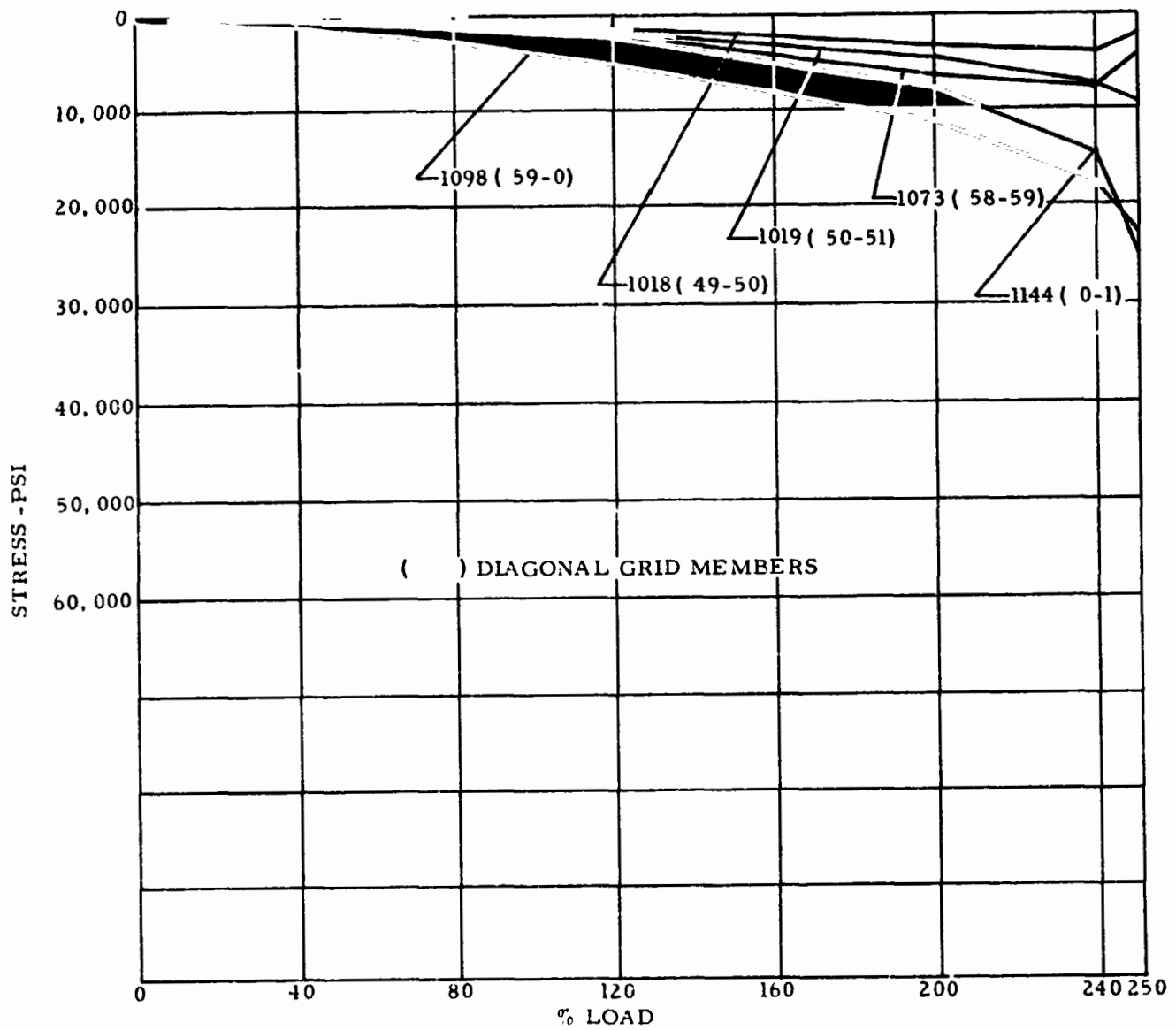


Figure C-12. Stresses in failed grid members (diagonal)

s distance between extreme fibers on inner and outer flanges
 I, A section moment of inertia and cross sectional area based on a
 skin width equal to 47 times the skin thickness being effective
 in contributing to these properties.

Based on average grid member cross section dimensions in Figure C-1b and the computerized analysis described in Subsection C.3.2.3, $C_o = 0.504$ inch, $A = 0.162$ in², and $I = 0.013$ in.⁴ ($s = 0.73$ inch).

Using the above and available S_1 and S_2 measured (strain gage) data in Eqs. 2-1 and 2-2 grid member axial forces and bending moments are computed for 200, 220, 240, and 250% load conditions for part of the structure near the peak load intensity area. These are shown in Figure C-13. When measured stresses S_1 or S_2 exceed 61,000 psi (material yield stress) actual stresses are assumed to be 61,000 psi. Data in Figure C-13 are labeled with an asterisk to indicate measured stresses that exceed 61,000 psi. Negative moments imply compression in outer flange.

The following observations are made after an examination of data in Figure C-13.

1. When the structure is primarily in its elastic range (i.e., up to 200% load) axial forces in the diagonal members are about 10% of axial forces in longitudinal members. At 250% load diagonal members experience as much as 25% of the load in longitudinal members. This is caused by load redistributions due to local yielding in the structure.
2. Positive moments in transition structure grid members at the upper and lower bolted flanges indicates possible failure of jack bolts in flanges. This failure would cause load to be relieved from the skin side of the structure and to be picked up on the inboard side of the loading fixture flange. The high bending moment in the failed longitudinal grid members at circumferential Stations 0 and 59 may have precipitated overall failure by failing inner flanges respectively in compression and tension. The negative bending moment in the failed grid member at Station 59 is due to beam column effects while at Station 0 it is due to flange kick moments.

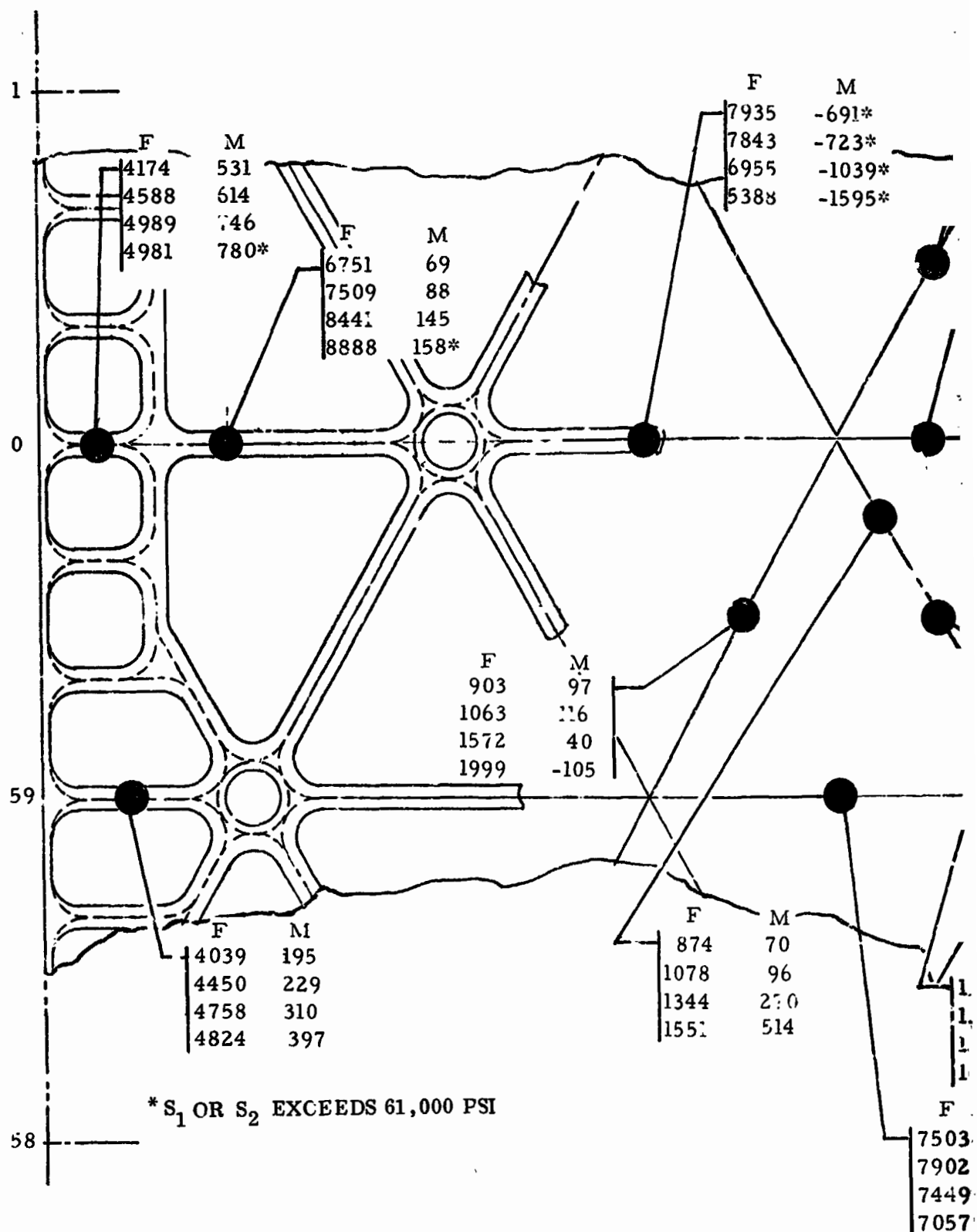
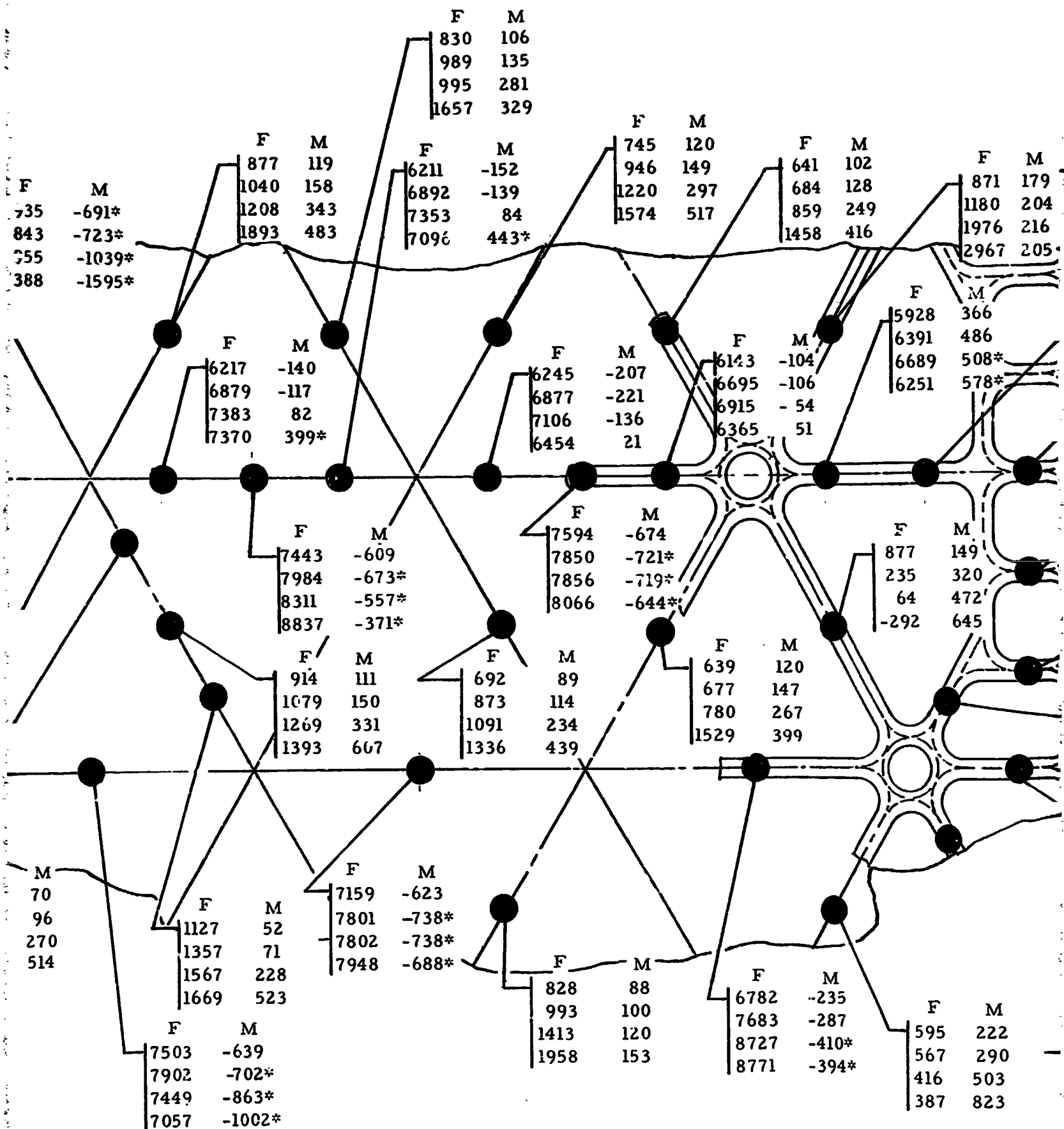
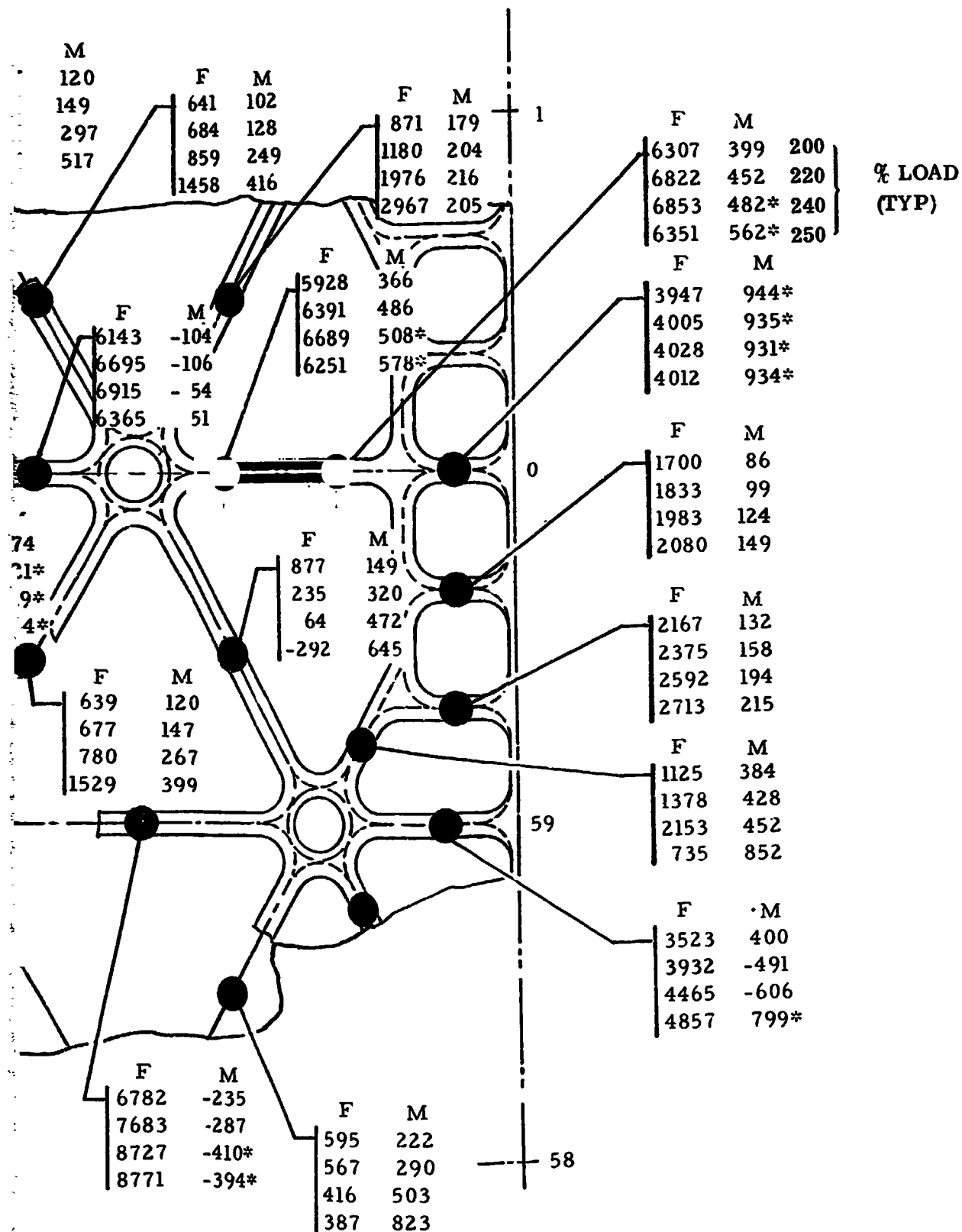


Figure C-13. Stresses near peak load intensity area.

FOLDOUT FRAME



FOLDOUT FRAME



FOLDOUT FRAME

3

3. Shear flow in skins and loads in diagonal members accounts for variations in loads along longitudinal members.
4. Since diagonal grid members experience less load than in-line grid members it may be reasonable to assume that $70 t_1$ effective skin width should be used in computing the cross sectional properties of diagonal members. If this were done the loads in the diagonal members would be greater than those indicated on Figure C-13 (by an estimated 17%).

C.2.6 APPLIED LOADS

It is assumed that loading fixture rigidity is an order of magnitude greater than that of the specimen. The 260%-of-loading-condition-9-failure load then produces theoretical edge load intensities, N , and stresses in the transition structure, S_t , at stations in the vicinity of expected peak load intensities. See Table C-1. Table C-1 was computed using:

$$N = \frac{P}{2\pi R} + \frac{M_b \cos \theta}{\pi R^2} \quad (2-3)$$

where

P is the axial load,

M_b body bending moment,

R cylinder radius,

θ angle between Station 0 and reference station.

Table C-1. Applied edge loads

STATION	N , lbs/in.	S_t , psi
0	1655	22,761
1, 59	1650	22,692
2, 48	1637	22,514
3, 57	1616	22,197
4, 56	1583	21,771
5, 55	1544	21,235
6, 54	1497	20,588
7, 53	1442	19,832

Measured specimen stresses in geometrically identical lower-flange-transition members which are in line with longitudinal members are plotted in Figure C-14 as a function of percent loading. Station positions in Figure C-14 are projected on a line normal to the bending axis. The stresses, S_t , from Table C-1, are also plotted on Figure C-14. The substantial difference between theoretical and measured stresses (at 260 and 250%) is due to the following collective or individual cases:

1. Reactions in the basic specimen structure produce bending moments in the transition structure. The measured stresses are the result of axial loads and flange bending moments.
2. Crippling of jack bolts in loading fixture transfers loads to the inner flanges and creates a kick moment.
3. Insufficient body rigidity in the loading fixture causes hydraulic cylinder loads to induce local load peaking.
4. There is a discrepancy between loads that are proportional to distance from loading fixture bending axis and actual loads used in test. In both cases at 100% load, the total applied axial load is 120,000 lbs and body bending moment is 3.6×10^6 in.-lb. Figure C-15 shows differences between proportional and actually used forces for 260% applied load. The 883 lbs force for example is the difference between forces actually used and that would have resulted from proportional loading in hydraulic cylinders 1, 12, and 11. The force discrepancies are 4% for the 883 lb force, 3% for 464 lbs, and 27% for 2558 lbs. Directions of discrepancies are such that if the loading fixture rigidity were negligible compared to the specimen load peaking at the high load intensity area would be 15.6% greater than predictable on the basis of a perfectly rigid loading fixture; it is estimated that the applied load error is not over 3 to 4% due to this cause.

Effects of above factors influence the out of plane character of measured displacements in the upper loading fixture as shown in Figure C-16. Changes in fixture plane slope (in Figure C-16) is also influenced by local changes in adapter

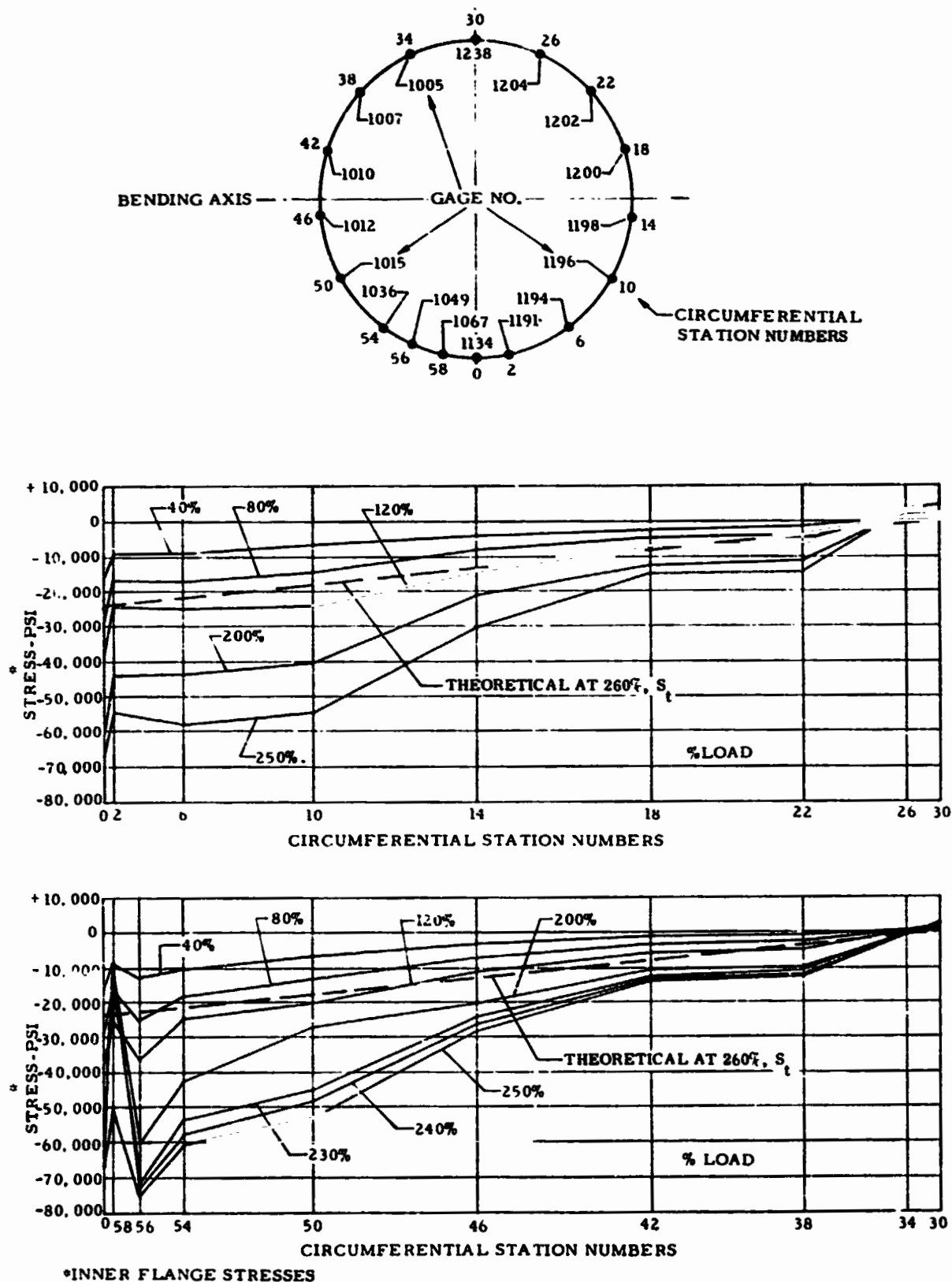


Figure C-14. Circumferential stress distribution in structural transition.

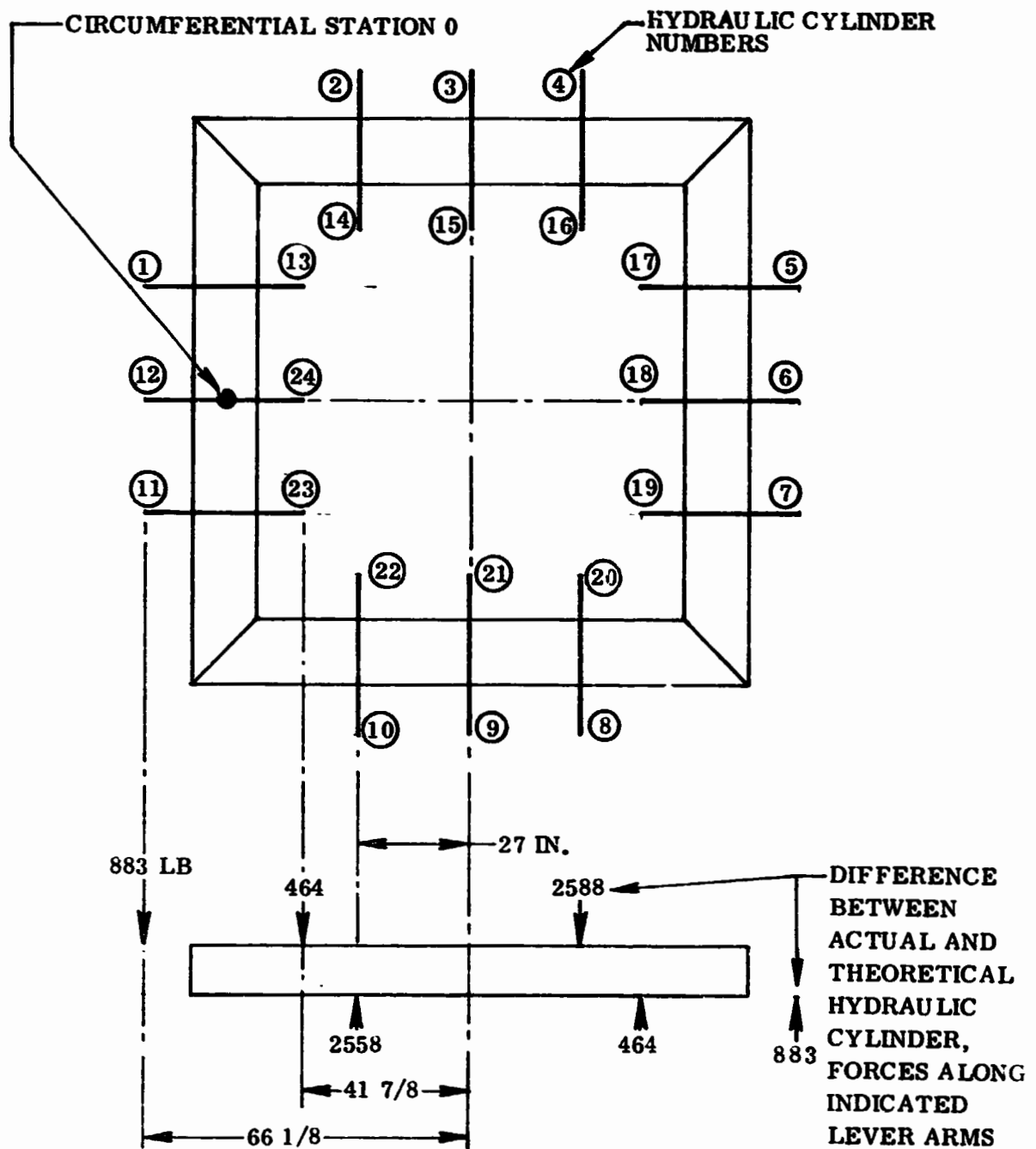


Figure C-15. Differential forces on loading fixture

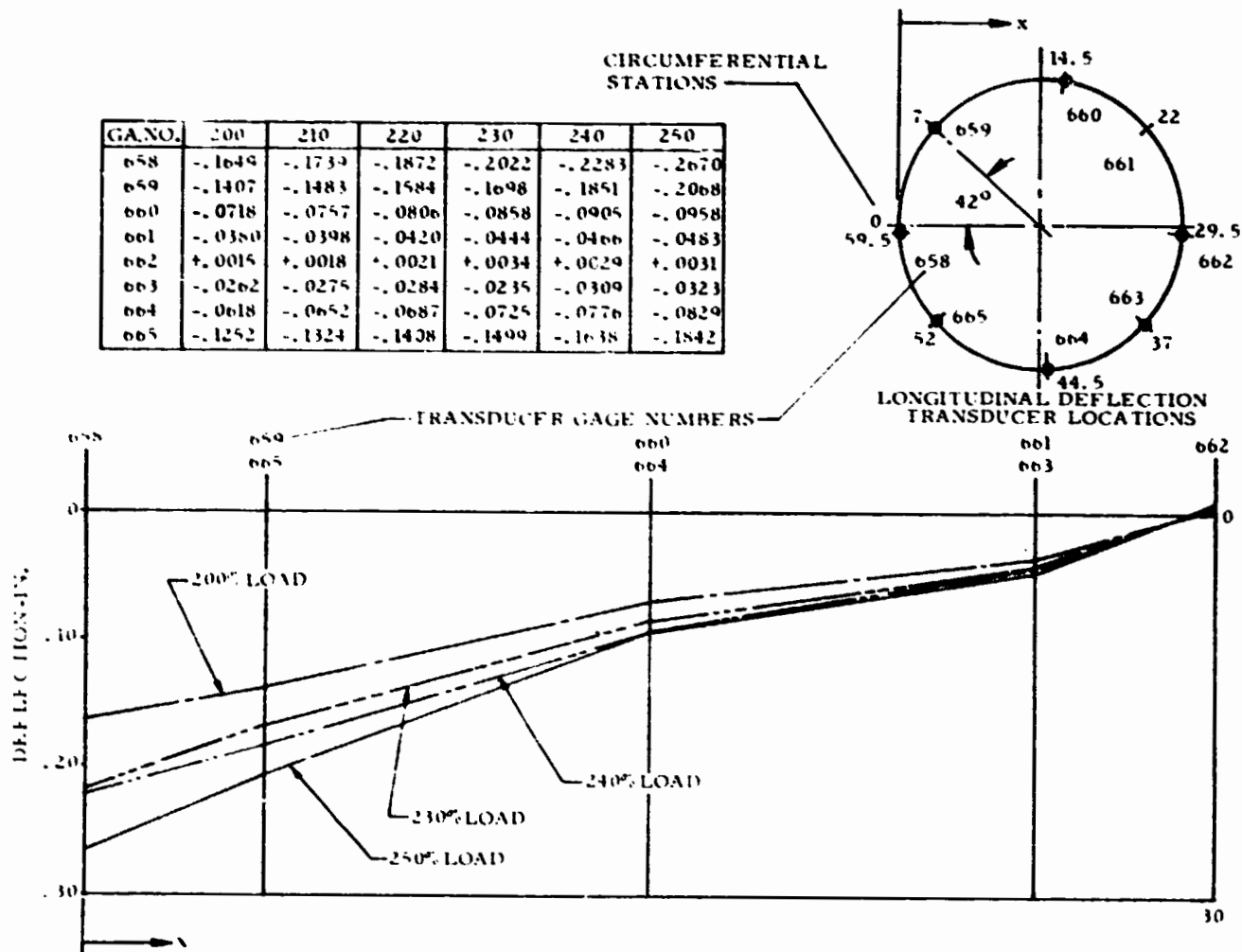


Figure C-16 Measured displacement of upper loading fixture

structure axial rigidity due to skin buckling. Skin buckling occurs at a fraction of the load carrying capability of the basic structure. This buckling is estimated to be limited to the central 2/3 of the adapter length.

The load peaking at circumferential Stations 0 and 56 as evidenced in Figure C-14 indicates the likelihood of failure having been precipitated at these stations. General instability is most likely to have occurred at Station 56 where load peaking is greatest.

The back-to-back strain gage data available on the longitudinal grid members between circumferential Stations 0 and 59 are used to compute applied axial (N) and kick moment (M) edge loading. These quantities are plotted vs. percent load in Figure C-17. The following assumptions were made to arrive at the computed values.

1. The skin in the transition structure is fully effective. This results in 42-times-skin-thickness effective skin width and resulting grid section properties are $C_o = 0.494$ in, $A = 0.154$ in² and $I = 0.0124$ in⁴.
2. Axial forces and bending moments in grid members were computed per procedure described in Subsection C.2.5 and averaged for the four grid members involved. This assumes that the transition structure is fully effective in smearing loads. The highest peak edge intensity in the transition structure at 260% load is 2224 lbs/inch, and the largest kick moment is 427 in-lb/inch.
3. Two plots are shown for both N and M in Figure C-17. The lower values derive from assuming that the actually transmitted stress never exceed the 61,000 psi yield stress even though the measured gage stresses are greater than 61,000 psi. The higher values are based on the measured stresses being the actual stresses even though they are over 61,000 psi.

Data in Figure C-17 reasonably confirms the estimated 1654 lbs/inch failure load, however, this load is not necessarily at the location for which Figure C-17 applies.

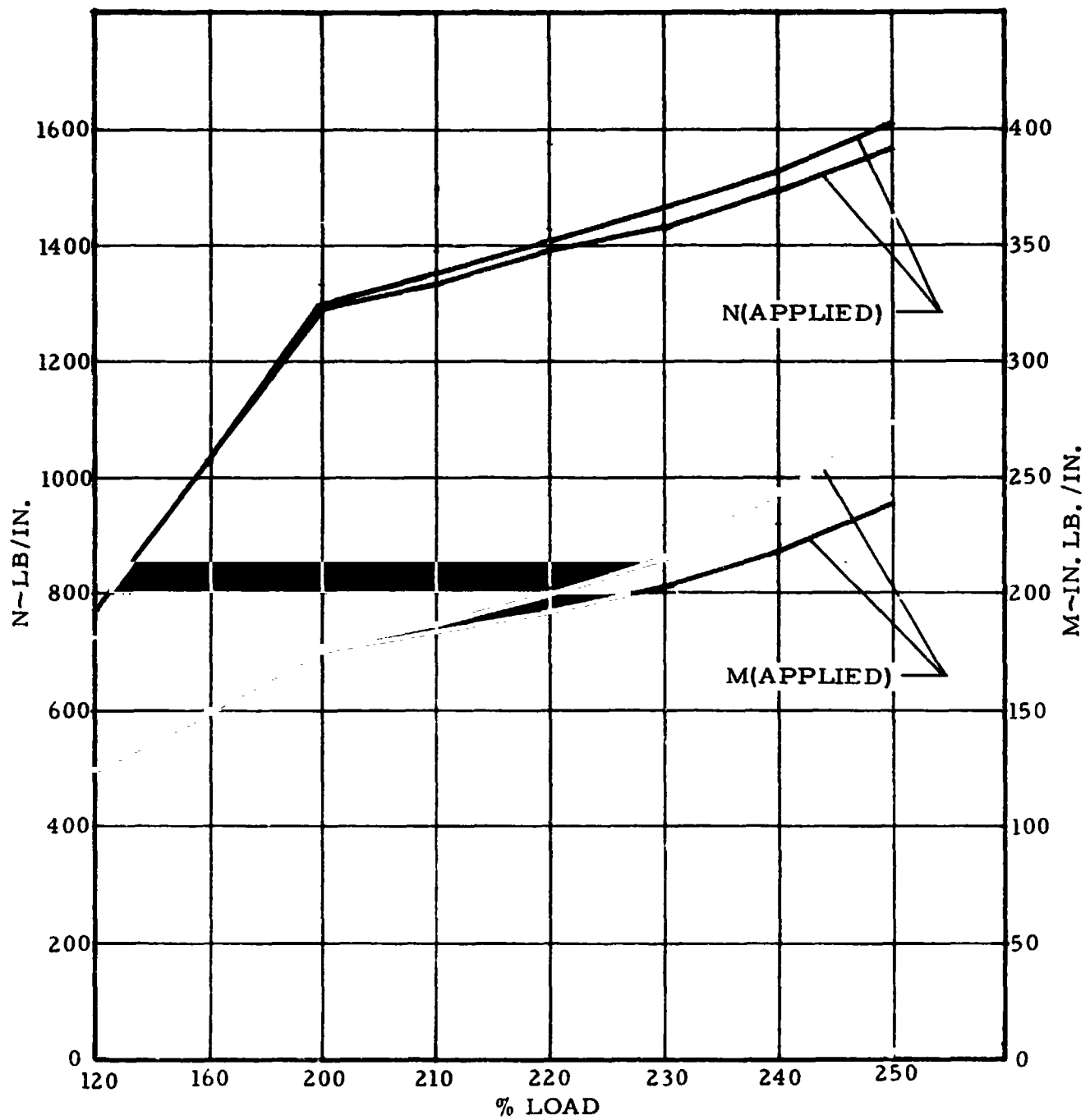


Figure C-17 Edge loading due to measured transition stresses

C.2.7 TOPOGRAPHICAL PLOTS

Topographical and differential topographical plots of radial deflection contours in the test specimen, as shown respectively in Figures C-18 and C-19, are obtained through automated data reduction and plotting. Linear transducers measuring radial deflections at structural nodes (see Figure C-5) provide basic input for generating the topographical plots.

C.2.7.1 Program description

Data reduction for isogrid topographical plots is broken down into four separate programs. Each program performs a unique function in the total process of conversion to final plot.

The first program takes the GE 235 computer data tape produced by the MSFC-Structural Test and Checkout System (STACS) and converts it to 60 bit words, acceptable to the CDC CYBER 70 computer.

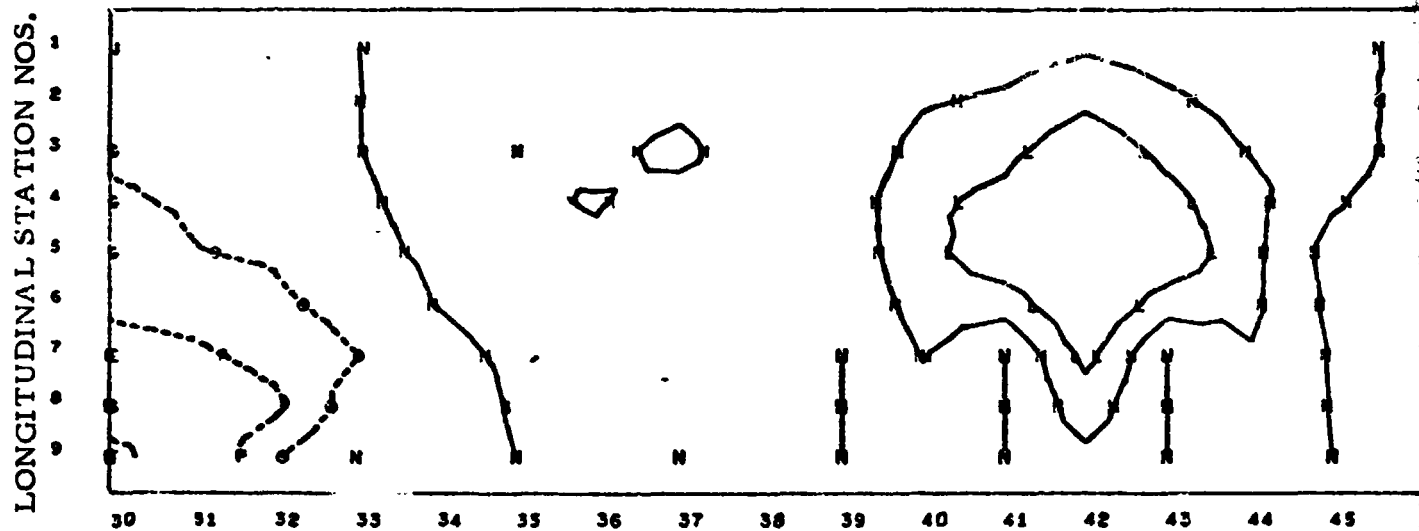
The second program takes the new data tape and decodes the 60 bit words into real values which are the same values as those in the GE 235 tape.

Program three writes the load scans on a tape for the plot program. This program by way of input parameters selects the load scans wanted, and by use of linear interpolation computes the values for non-existent nodes from the measured node values.

The final program plots the contours from the data tape constructed from program three. The program can check for as many as thirty different contour levels that show up as solid lines for positive deflections and dash lines for negative. This program generates either straight plots and/or first or second order differencing plots which are determined by the input parameters. The actual plots are produced by the SC 4020 plotter.

The smaller the selected increments between contour levels the closer are the contour plots and the more pronounced are surface slope indications.

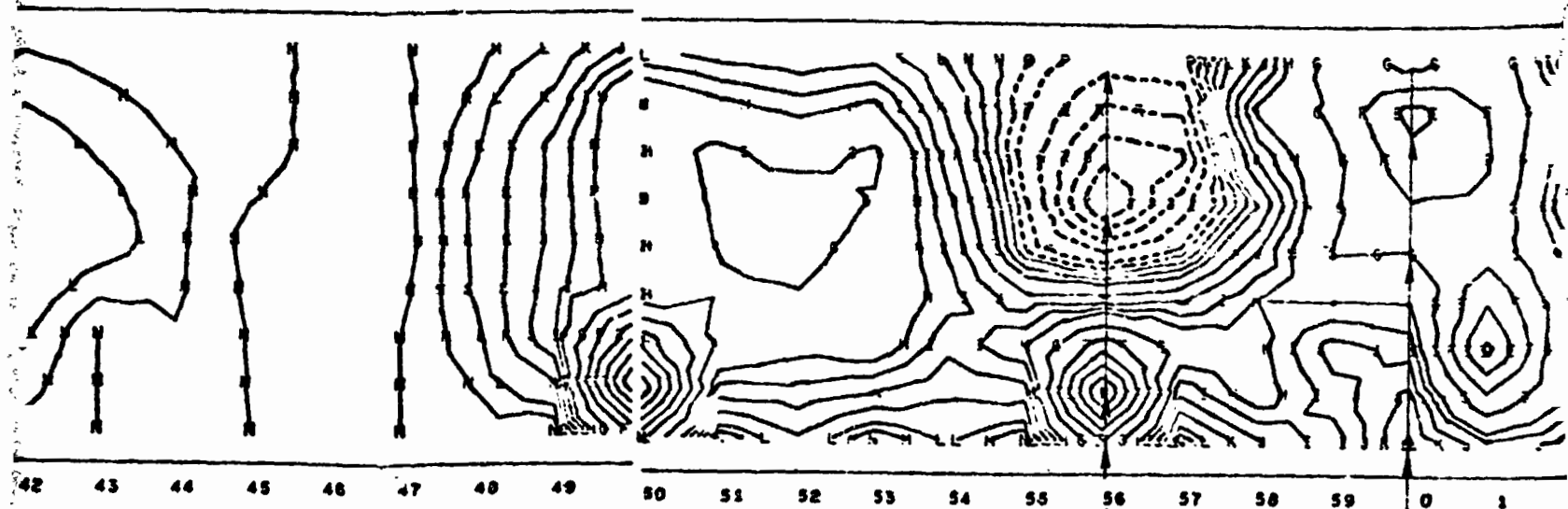
REPRODUCIBILITY OF THE
ORIGINAL PAGE IS POOR



ISOGRID ADAPTER TEST 37513 CONDITION 9A (1-07-74)
LOAD IS 250 PERCENT

A = .4300
B = .4000
C = .3500
D = .3000
E = .2500
F = .2000
G = .1500
H = .1000
I = .0800
J = .0600
K = .0400
L = .0200
M = .0100
N = 0.0000
O = -.0100
P = -.0200
Q = -.0400
R = -.0600
S = -.0800
T = -.1000

FOLDOUT FRAME



CUMFERENTIAL STATION NOS.

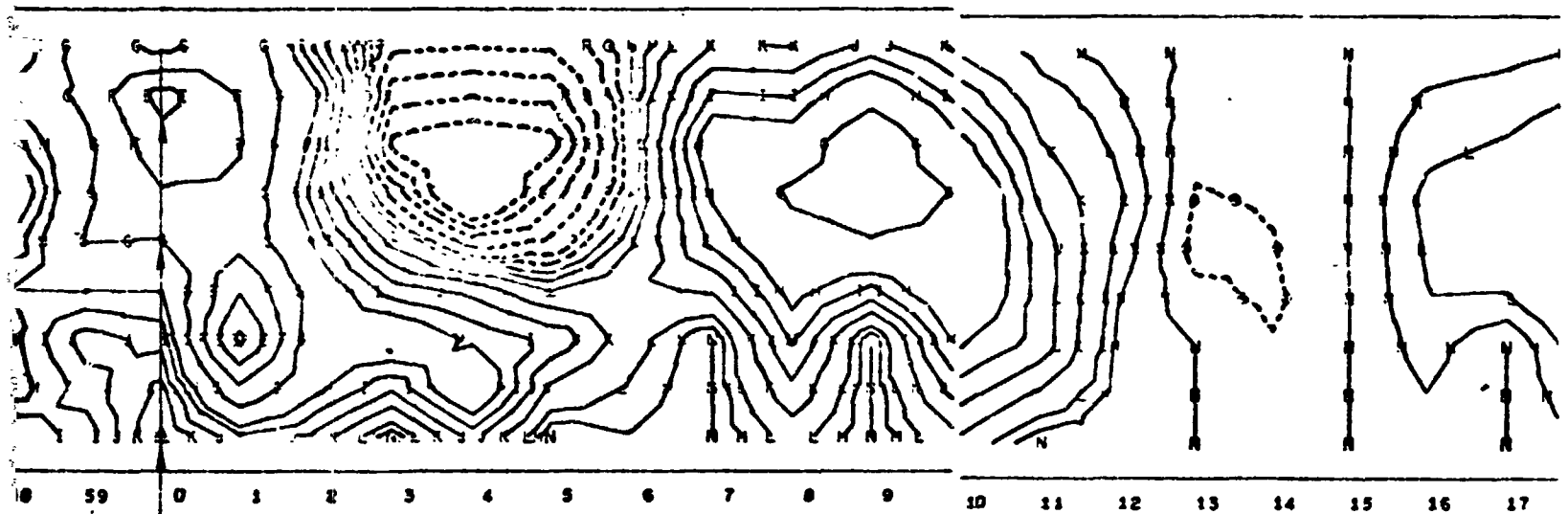
L K J I

F E D C B G H I J K
L M N O P Q R S T

FOLDOUT FRAME

2

REPRODUCIBILITY OF THE
ORIGINAL P



L K J I H G F E

C B G H I J K
C P Q R S T

FOLDOUT FRAME

5

REPRODUCIBILITY OF THE
ORIGINAL PAGE IS PO

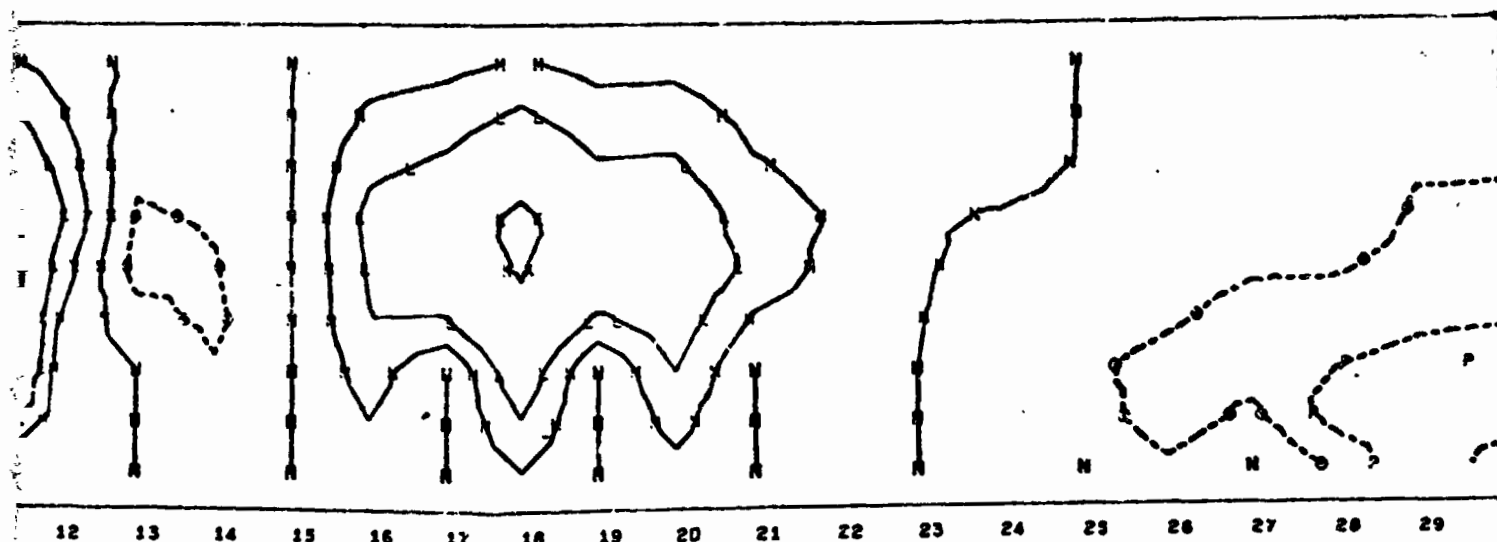
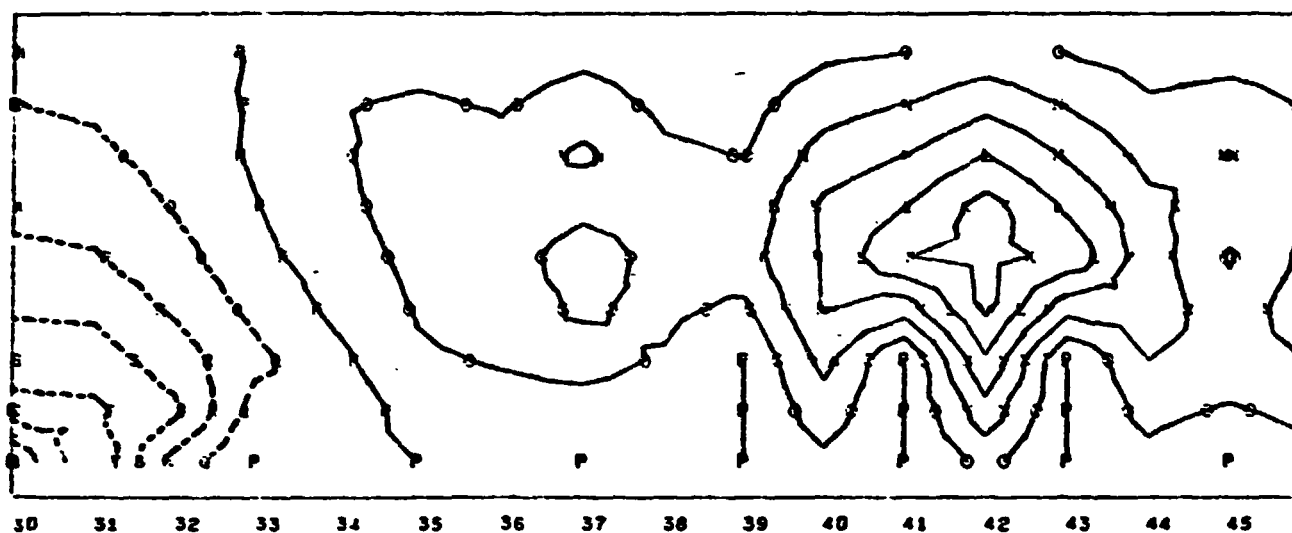


Figure C-18 Topographical plot 250% load

OUT-OUT FRAME

REPRODUCIBILITY OF THE
ORIGINAL PAGE IS POOR

LONGITUDINAL STATION NOS.

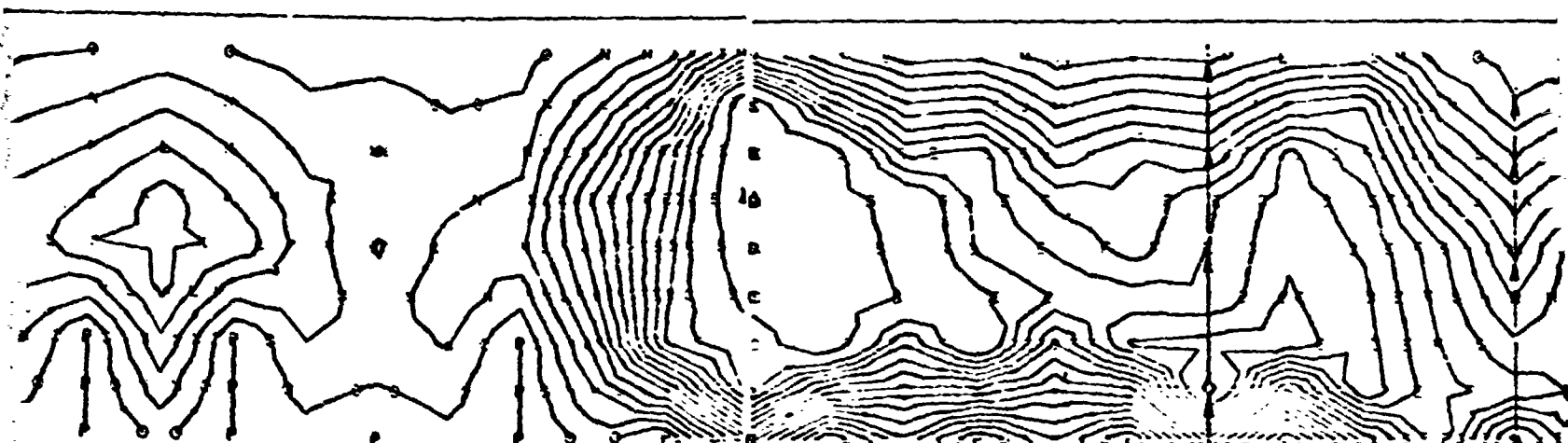


ISOGRID ADAPTER TEST 375012 CONDITION 9 (1-02-74)
LOAD IS 200 PERCENT

A = .0050
B = .0750
C = .0650
D = .0600
E = .0550
F = .0500
G = .0450
H = .0400
I = .0350
J = .0300
K = .0250
L = .0200
M = .0150
N = .0100
O = .0050
P = 0.0000
Q = -.0050
R = -.0100
S = -.0150
T = -.0200

FOLDOUT FRAME

THE
JOB



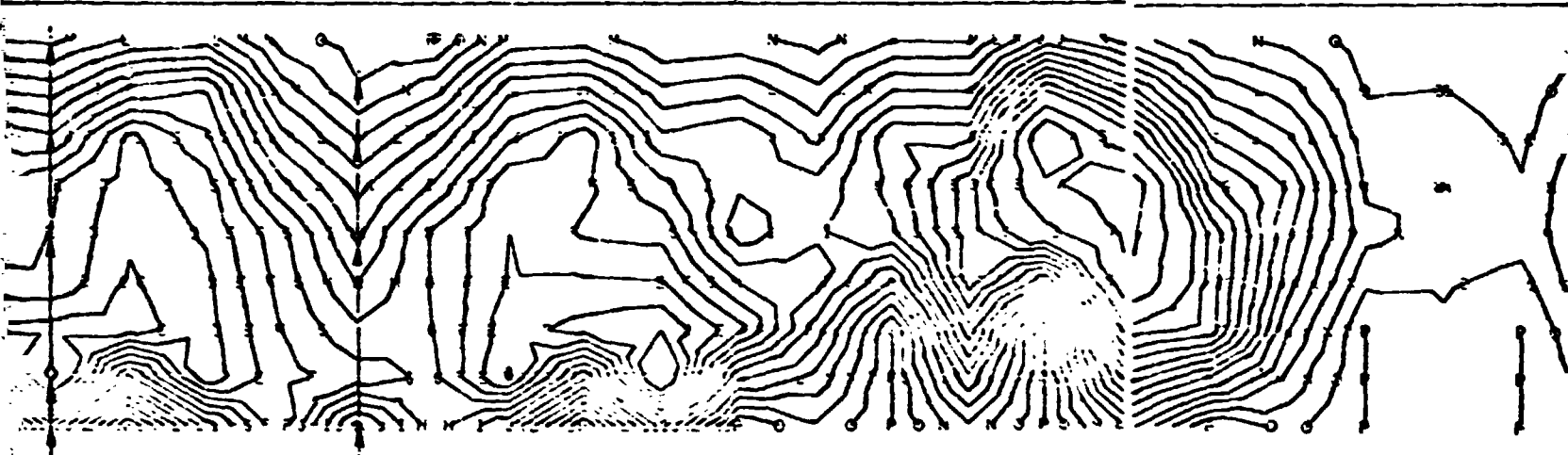
41 42 43 44 45 46 47 48 49 50 51 52 53 54 55 56 57 58 59 0

K
J

H G F E D C B C
E F G H I J K L

FOLDOUT FRAME

REPRODUCIBILITY OF THE
PAGE IS POOR



56 57 58 59 0 1 2 3 4 5 6 7 8 9 10 11 12 13 14 15

CIRCUMFERENTIAL STATION NOS.

K J I H G H I
J K L M N O

H G F E D C B C D
E F G H I J K L M

FOLDOUT FRAME

3

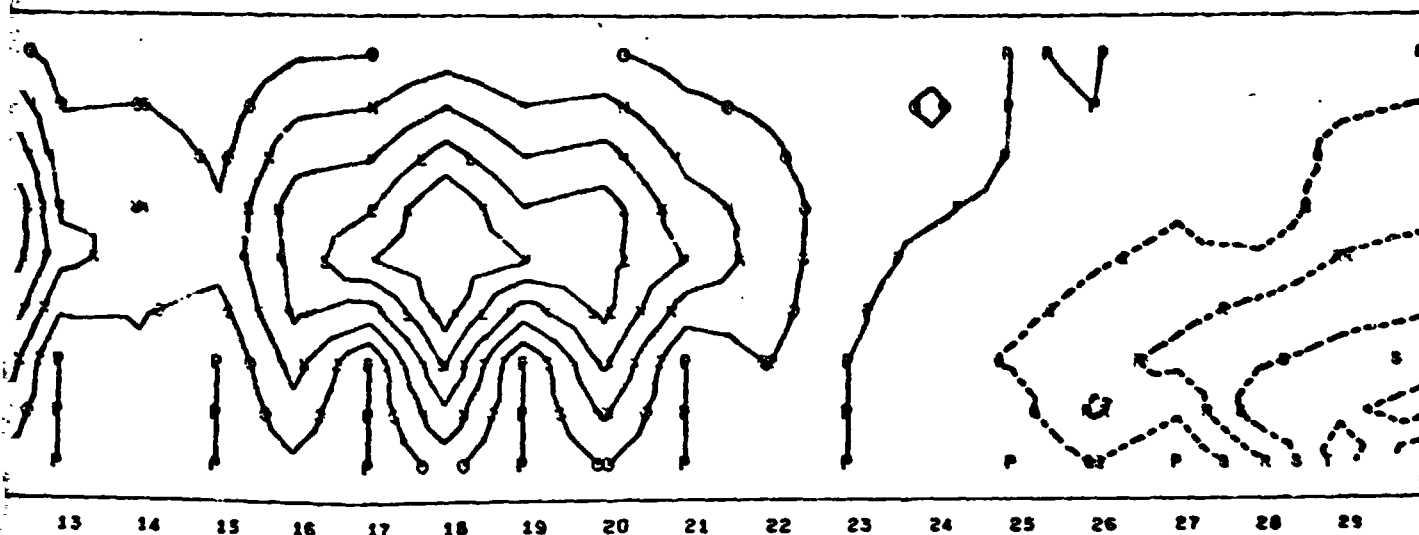


Figure C-19 Differential topographical plot 250-240% load

C.2.7.2 Preliminary evaluation

Examination of the contour plots (Figures C-18 and C-19) in the vicinity of circumferential Stations 0 and 56 indicates that surface grades in these areas are large compared to surrounding areas and that much of this contour irregularity developed in the 240 to 250% load increment. This tends to confirm the conclusion in Subsection C.2.6 that failure probably started near circumferential Station 0 or 56 and most likely Station 56.

C.3 ANALYSIS OF TEST RESULTS

The purpose of this section is to use test results to:

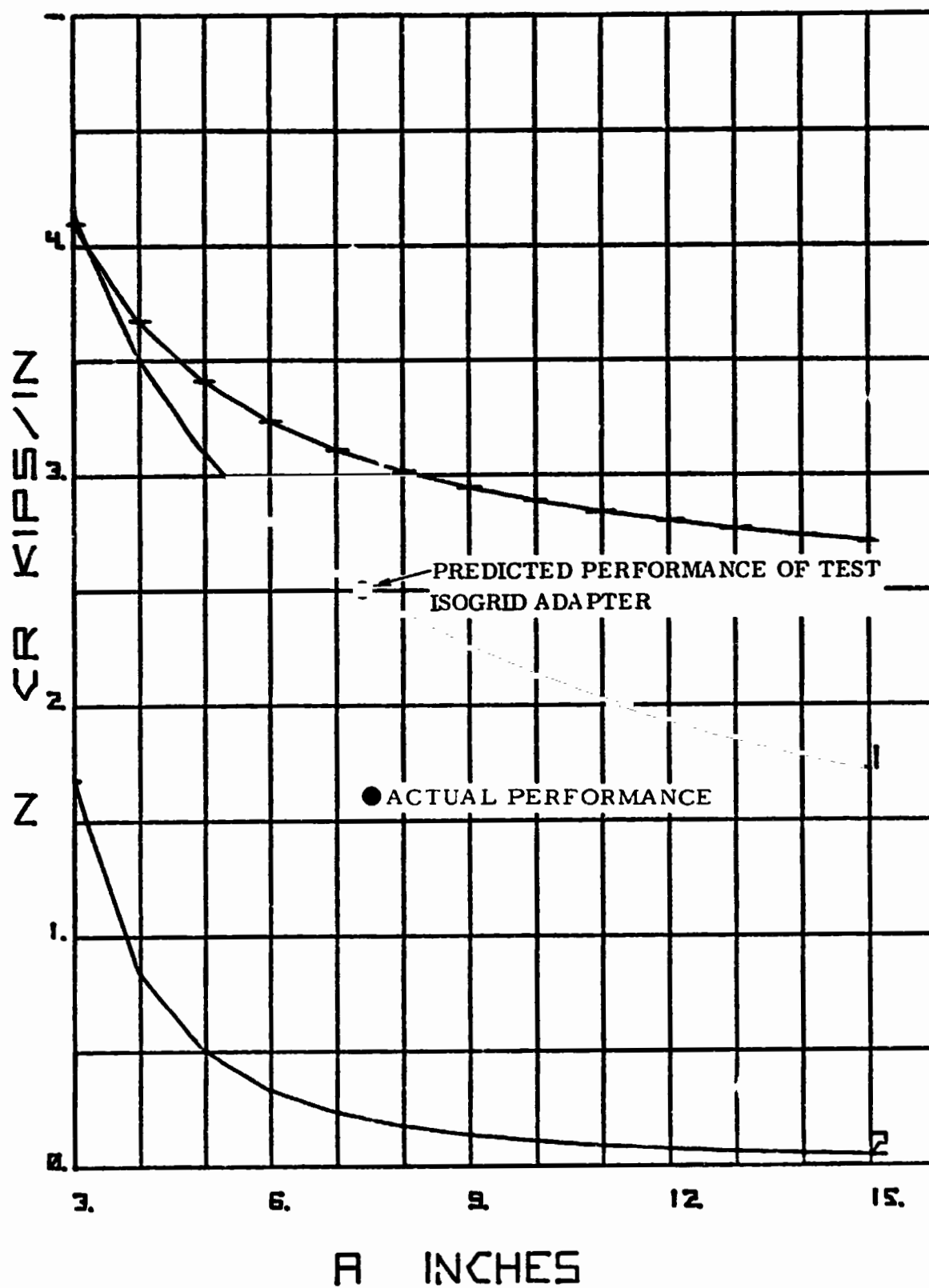
- (1) determine modification to the knock down factors for general instability described in Appendix B,
- (2) develop an extended local instability analysis and evaluate parameters in this analysis to obtain agreement with test results,
- (3) evaluate the effective skin width included in grid member cross section,
- (4) develop relationships for predicting local compression buckling in isogrid skin panels.

C.3.1 MODIFICATIONS OF GENERAL INSTABILITY KNOCKDOWN FACTORS

Using computer programs based on the analyses in Section B.2 of Appendix B, Figures C-20a to C-20d were produced to compare actual specimen performance with four different predicted specimen performances. Figures C-20a to C-20d include the following curves:

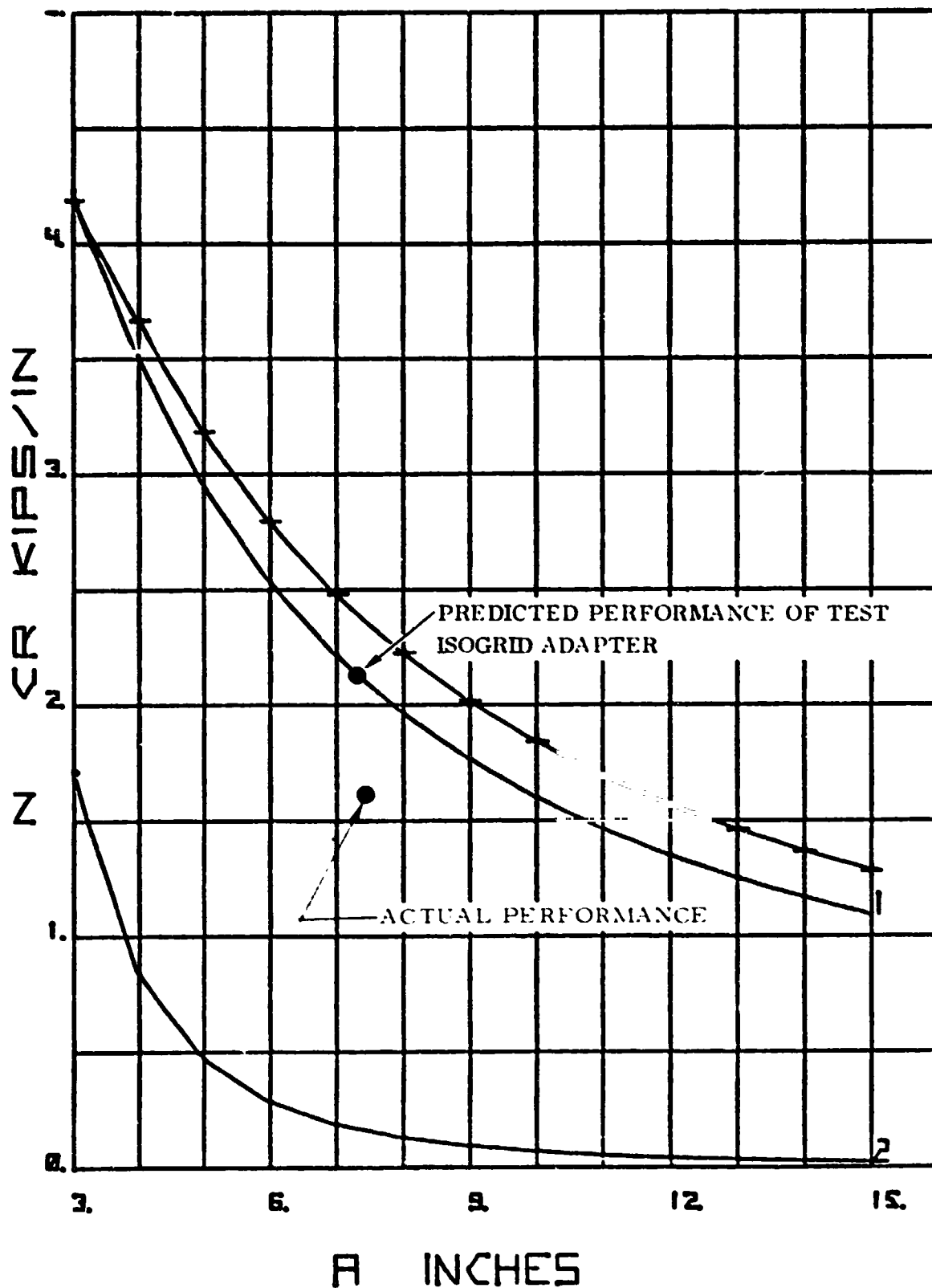
Curve labeled 1 is for general instability (i.e., it designates a plot of allowable edge load intensity N_{CR} , vs. node-to-node spacing a , for general instability as a limiting condition.)

Curve labeled 2 is for skin buckling (i.e., it indicates the edge intensity at which skin buckling starts. Since the test specimen includes I-beam grid members skin stability is not critical to overall structural load carrying capability. This is similar to a condition common in skin stringer designs.)



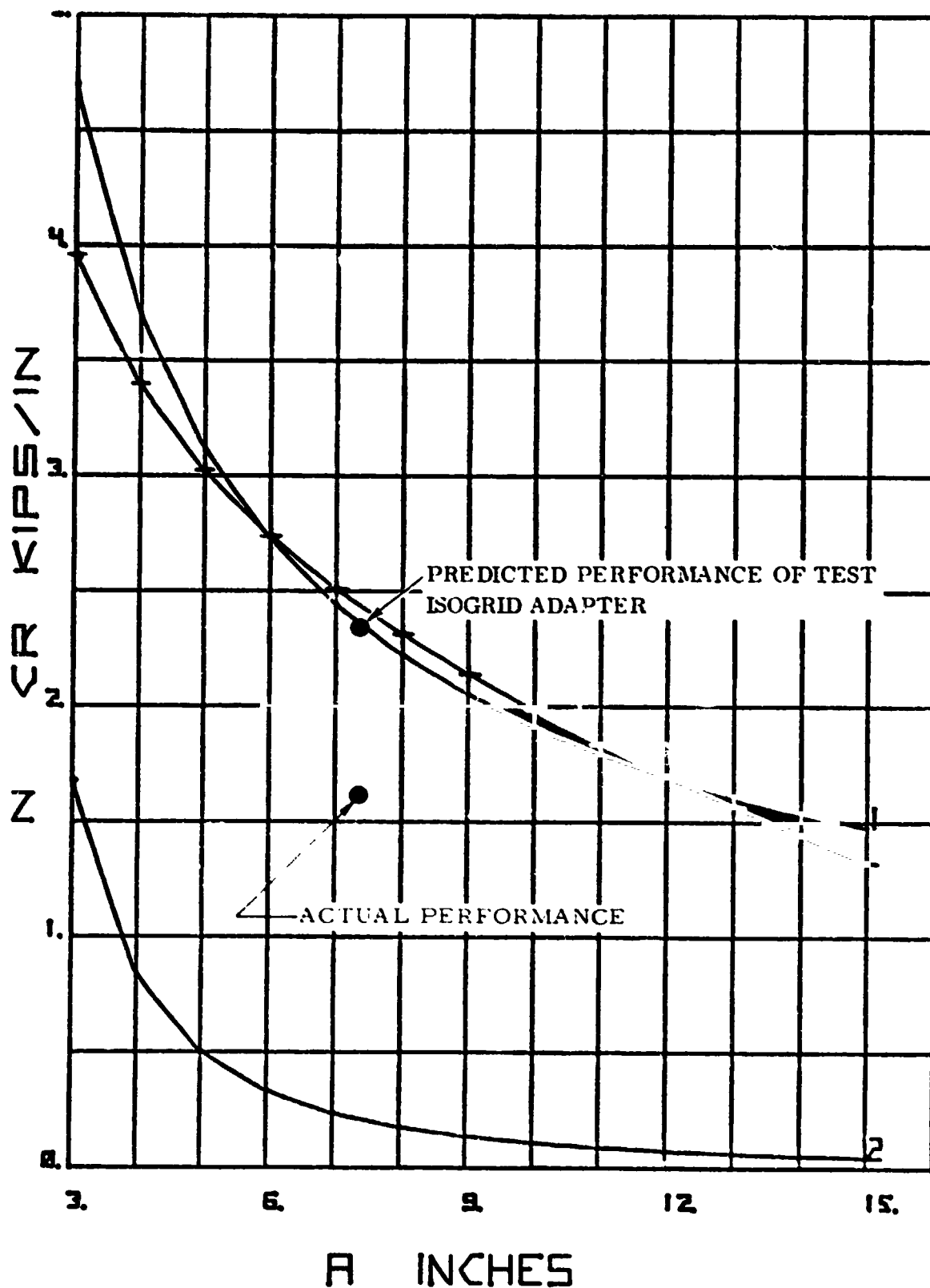
$T=0.040$ $D=0.584$ $S=0.730$ $W=0.415$ $R=60.00$
 $U=0.051$ $C=0.080$ $B=0.040$ $E=0.070$ $M-1A$

Figure C-20a Performance of test isogrid adapter



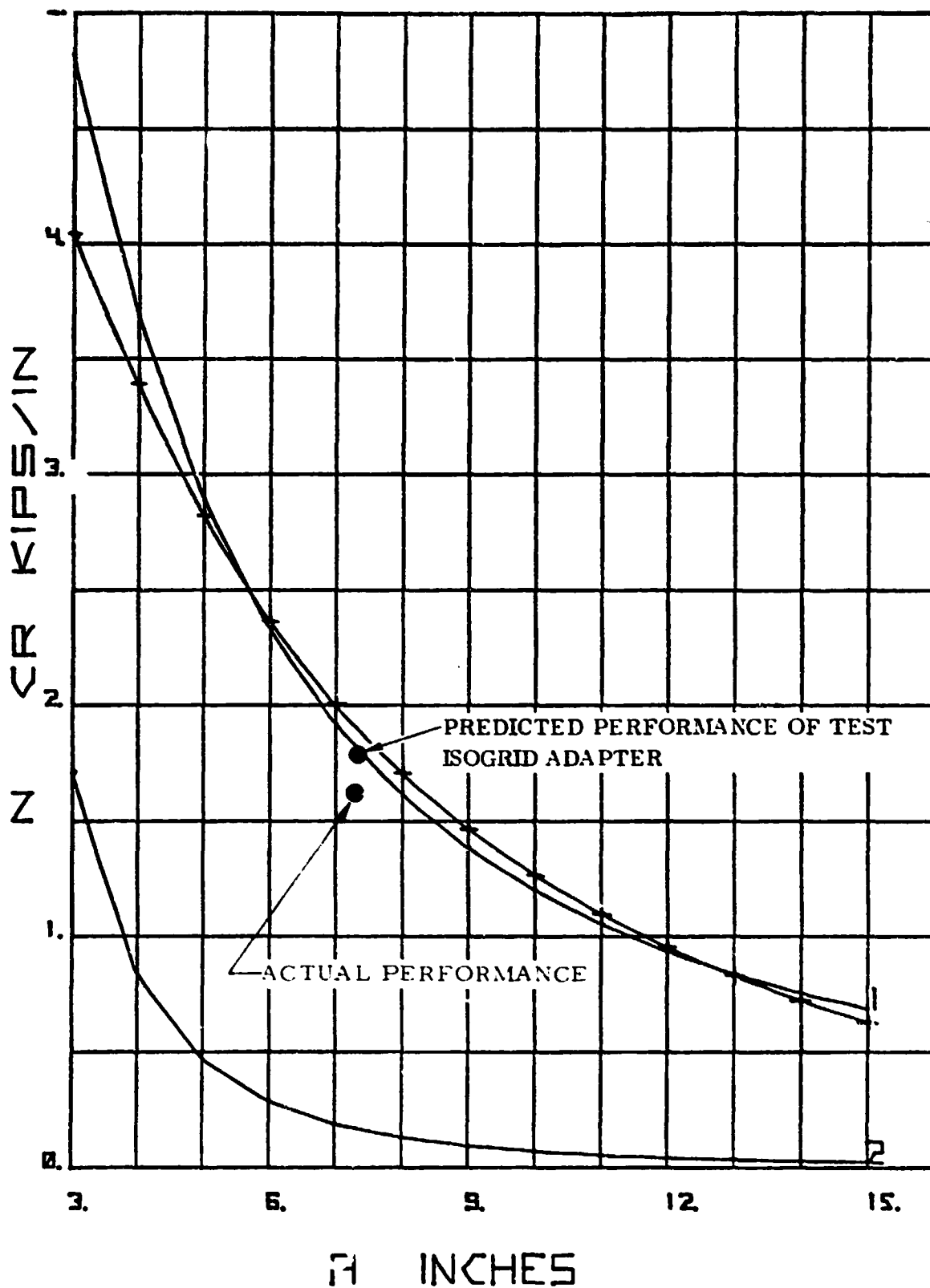
T=0.040 D=0.584 S=0.730 W=0.415 R=60.00
 U=0.051 C=0.080 B=0.040 E=0.070 M-18

Figure C-20b Performance of test isogrid adapter



T=0.040 D=0.584 S=0.730 W=0.415 R=60.00
 U=0.051 C=0.080 B=0.040 E=0.070 B-1A

Figure C-20c Performance of test isogrid adapter



T=0.040 D=0.584 S=0.730 W=0.415 R=60.00°
 U=0.051 C=0.090 B=0.040 E=0.070 B-18

Figure C-20d Performance of test isogrid adapter

Curves 3 and 4 (not shown in Figures C-20a to C-20d) are respectively for web crippling and flange buckling. Edge intensities that create web crippling or flange buckling are greater than chosen scale values therefore they do not appear on Figures C-20a to C-20d.

Curves labeled with cross marks are for edge intensities at which material yield strength or grid member column buckling is the limiting factor. In Figures 20a and 20b the cross marked curves indicate material yield properties while in Figures C-20c and C-20d they indicate column buckling.

The four predicted performances are:

M-1A (Figure C-20a) in which general instability is based on the McDonnell Douglas analysis (see Appendix B) and assumes that the skin is fully effective in reacting load (i. e. , even though the skins elastically buckle they develop tension fields that cause them to be fully effective in reacting loads).

M-1B (Figure C-20b) in which general instability is based on the McDonnell Douglas analysis assuming that a width of skin equal to 47 times its thickness, t_1 , effectively contributes to the cross sectional properties of the I-beam grid member (e. g. , $23.5t_1$, on each side of outer flange).

B-1A and B-1B (Figures C-20c and C-20d) which are respectively like M-1A and M-B except that the general instability curves in this case are based on a Convair Aerospace analysis presented in Subsection B.2.3 of Appendix B.

The structural parameters used in the above analyses are based on average values in Figure C-1 and listed on Figures C-20a to C-20d by the H. P. Calculator Plotter (see Section B.2.1 of Appendix B for definition of symbols).

In all cases predicted structural performance is dictated by general instability for the 7.338 inch node-to-node spacing in the test specimen.

C.3.1.1 Knock down factor corrections

It is clear from Figures C-20a and C-20c that the assumption of fully effective skin causes an excessive discrepancy between predicted and actual structural performance. These analyses are assumed invalid in evaluating test data.

From Figure C-20d it is seen that predicted performance based on general instability and column buckling are within about 5% of each other. This is within range of theoretical accuracy. Therefore the knock down factors corrections in Table C-2 are recommended to bring theory in line with test data.

Table C-2. Summary of theoretical and actual critical loads

Damaged area:	Center of panel No. 1 (see Figure C-1b)
Average actual failure load:	1655 lb/in
Theoretical failure loads	
General instability	
MDAC * analysis:	2140 lb/in
Convair** analysis:	1770 lb/in
Column buckling:	1854 lb/in
Knock down factor correction (N_{CR} theoretical/ N_{CR} actual)	
General instability	
MDAC analysis:	1.29
Convair analysis:	1.07
Column buckling:	1.12

*per Subsection B.2.2 of Appendix B

**per Subsection B.2.3 of Appendix B

Insufficient data is available at this time to preclude whether general instability or column buckling is the dominant failure mode.

C.3.2 EXTENDED LOCAL INSTABILITY ANALYSIS

Beam column instability of two tandem longitudinal grid members will be considered as a basis for evaluating extended local load carrying capability of iso-grid structures. Grid orientation "b" in Figure B-4 of Appendix B is assumed for purposes of this analysis.

C.3.2.1 Description of model

The model to be analyzed includes two initially straight members the neutral axes of which intersect at a point offset e with respect to a line along which applied forces F act as shown in Figure C-21a. The offset is taken as positive when it is in the skin-to-inner flange direction. It can represent anticlastic or synclastic curvature, misalignment of applied forces, and eccentricity between applied forces and beam neutral axis.

A fixity due to a torsional spring rate k_t is assumed to exist at points 1 and 3 in Figure C-21a. This spring rate, about a normal to grid-member-plane axis, is determined from the model in Figure C-21b which includes an in-line grid member of arbitrary length a'' . Likewise the linear spring restraint k at point 2 (also used in the model for determining k_t) is based on the model in Figure C-21c. An arbitrary grid member length a' is used in this model. The equivalent lengths a' and a'' are obtained from:

$$a' = K_f a \quad (3-1a)$$

$$a'' = K_a a \quad (3-1b)$$

where factors K_f and K_a are determined to equate theoretical and measured data.

Isogrid grid member cross section shown in Figure C-21d is taken normal to the neutral axis and to include $47 t_1$ effective skin width contributing to the cross sectional moment of inertia about the indicated neutral axis.

While the analysis to be presented is of a flanged isogrid structure it is readily extended to:

- (1) Unflanged isogrid with skin,
- (2) Flanged isogrid without skin,

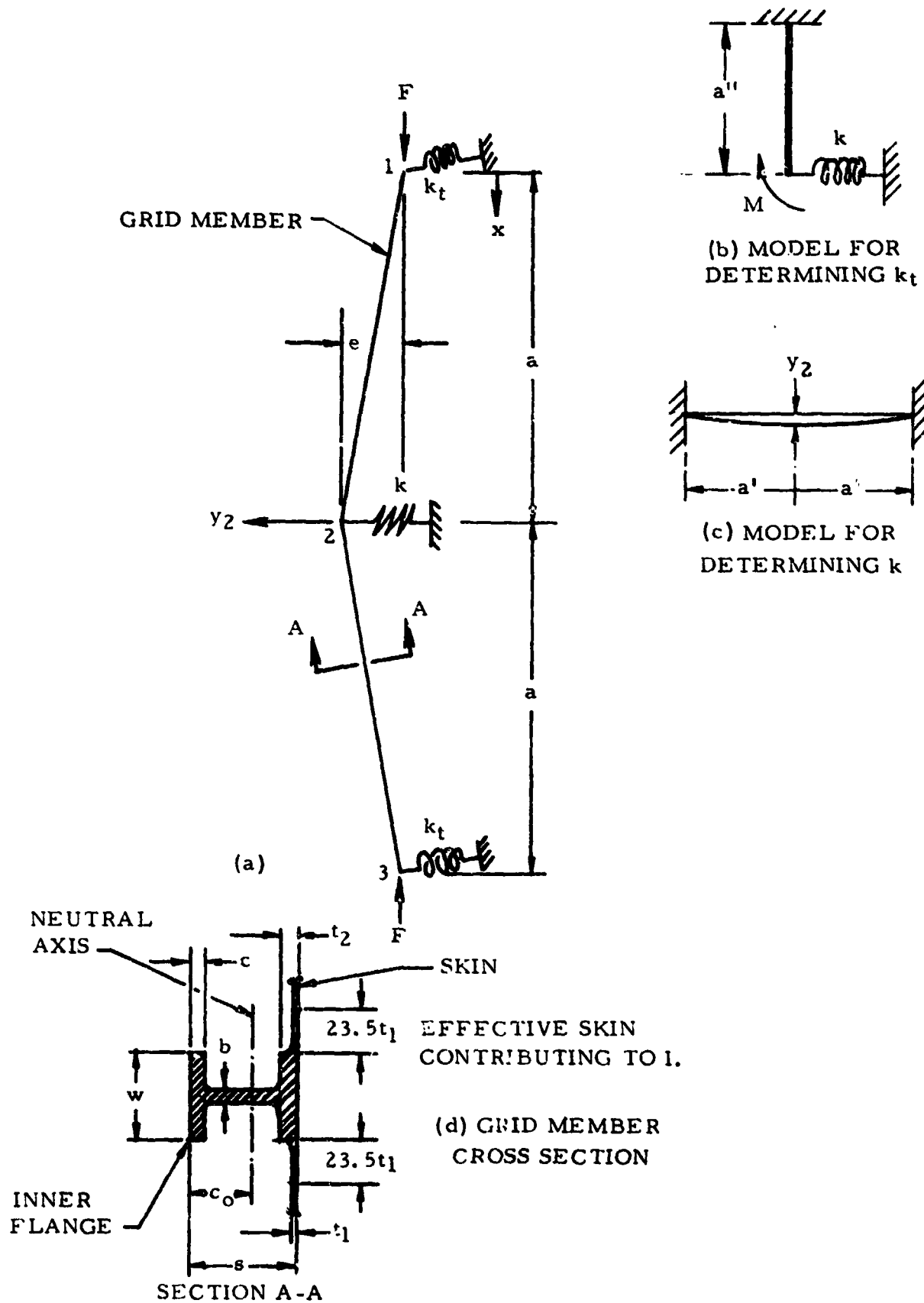


Figure C-21, Beam column model for extended local instability analysis

- (3) Frame stabilized skin-stringer structures. The choice of K_a and K_f factors would have to account for differences in frame and stringer cross-sectional properties if any,
- (4) Flanged or unflanged waffle structure.

C.3.2.2 Definition of symbols

The symbols used are as given in Subsection B.2.1 of Appendix B, those above, in Figure C-21 and the following:

- N_7 = allowable edge load for conditions that yield stress F_{cy} ,
is not exceeded in the structural model in Figure C-21,
- $A = A'$ = area of equivalent I-beam member cross section including
47 t, width of effective skin,
- S_o, S_a = grid member stresses at $x = 0$ and $x = a$ in Figure C-21a,
- I = is about the neutral axis shown in Figure C-21d,
- b = $(b_1 + b_2)/2$,
- η = the fraction of the total load reacted by in line grid members.

C.3.2.3 Isogrid cross sectional properties

The properties A , I and Co are computed from the following on the basis of the parameters shown in Figure C-21d.

$$A = (t_2 + c) w + 47 t_1^2 + (s - c + t_2) b \quad (3-2a)$$

$$I = \frac{1}{12} w c^3 + c w (c/2)^2 + b (s - c - t_2)^3 \frac{1}{12} \\ + (s - c - t_2) b \left[c + \frac{1}{2} (s - c - t_2) \right]^2 + \frac{1}{12} w t_2^3 \\ + t_2 w (s - t_2/2)^2 + \frac{1}{12} (47 t_1) t_1^3 + 47 t_1^2 (s - t_1/2)^2 \quad (3-2b)$$

$$Co \left[w c - \frac{b}{2} (2c) + 47 t_1^2 + w t_2 + s b - t_2 b \right] = \frac{w c^2}{2} - \frac{b c^2}{2} \\ + 47 t_1^2 (s - t_1/2) + w t_2 (s - t_2/2) + \frac{b}{2} (s - t_2)^2 \quad (3-2c)$$

C.3.2.4 Analytical Formulation

Assuming a straight line grid member between points 1 and 2 in Figure C-21a and that y is a deflection with respect to this line

$$M = -EI \frac{d^2 y}{dx^2} \quad (3-3)$$

where M , and applied bending moment, is positive when it causes compression on the right side of the grid member.

Between points 1 and 2:

$$M = Fy + \frac{Fex}{a} - k_t \Theta_1 - y_2 \frac{kx}{2} \quad (3-4)$$

where Θ_1 is the angular deflection at point 1 with respect to the line between points 1 and 2 and is positive when clockwise relative to this line. y_2 is the displacement at point 2.

From Eqs. 3-3 and 3-4

$$EI \frac{d^2 y}{dx^2} = -Fy + \left[-\frac{Fe}{a} + \frac{ky_2}{2} \right] x + k_t \Theta_1 \quad (3-4a)$$

The following is a model for Eq. 3-4a:

$$\ddot{y} = b_1 y + a_1 x + c_1 \quad (3-4b)$$

Using La Place Transform techniques the following solution has been developed for Eq. 3-4b.

$$y = - \left[\frac{a_1}{(-b_1)^{1.5}} + \frac{\Theta_1}{-(-b_1)^{0.5}} \right] \sin (x \sqrt{-b_1}) - \frac{a_1 x}{b_1} + \frac{c_1}{b_1} \left[\cos (x \sqrt{-b_1}) - 1 \right] \quad (3-4c)$$

This is also a solution to Eq. 3-4a when the following substitutions are made

$$\left\{ \begin{array}{ll} b_1 = -\frac{F}{EI} & b_1^1 = \frac{-Fe}{aEI} \\ a_1 = b_1^1 - k_{11} y_2 & k_{11} = -k/2EI \\ c_1 = k_{14} \Theta_1 & k_{14} = k_t/EI \end{array} \right\} \quad (3-4d)$$

Eq. 3-4c is valid when the force, F , is compressive as shown in Figure C-21a and therefore b_1 in Eq. 3-4d is negative (i.e., $-b_1$ is a positive value).

Slope, Θ , at any point on the elastic curve as a function of x is given by

$$\Theta = \Theta_1 - \frac{1}{EI} \int_0^x M dx \quad (3-5)$$

Using Eqs. 3-4 and 3-4d in Eq. 3-5 and performing integration

$$\begin{aligned} \Theta = \Theta_1 + \frac{1}{EI} \left\{ -F \left[\left(\frac{a_1}{(-b_1)^{1.5}} - \frac{\Theta_1}{(-b_1)^{0.5}} \right) \frac{[\cos(x\sqrt{-b_1}) - 1]}{(-b_1)^{0.5}} \right. \right. \\ \left. \left. - \frac{a_1 x^2}{2b_1} + \frac{k_{14} \Theta_1 \sin(x\sqrt{-b_1})}{b_1 (-b_1)^{0.5}} - \frac{k_{14} \Theta_1 x}{b_1} \right] \right. \\ \left. + \left[\frac{-Fe}{a} + \frac{ky_2}{2} \right] \frac{x^2}{2} + k_t \Theta_1 x \right\} \quad (3-5a) \end{aligned}$$

Making use of the boundary condition $\Theta_1 = 0$ at $x = a$ in Eq. 3-5a, Θ_1 is determined

as follows:

$$\Theta_1 = \frac{1}{k_2 EI} \left[-b_1^1 k_7 + \frac{F ea}{2} - y_2 \left(\frac{ka^2}{4} - k_{11} k_7 \right) \right] \quad (3-6)$$

where

$$k_2 = 1 - \frac{F [\cos (a \sqrt{-b_1}) - 1]}{EI b_1} + \frac{k_t a}{EI} + \frac{k_{14} a F}{b_1 EI} - \frac{F k_{14} \sin (a \sqrt{-b_1})}{EI b_1 (-b_1)^{0.5}} \quad (3-6a)$$

$$k_7 = -F \left[\frac{\cos (a \sqrt{-b_1}) - 1}{b_1^2} - \frac{a^2}{2 b_1} \right] \quad (3-6b)$$

Making use of the boundry condition $y = y_2$ at $x = a$ and Θ_1 from Eq. 3-6 in Eq.

3-4c:

$$y_2 = \frac{b_1^1 k_{71} + k_{72} k_{74} / k_2 EI}{1 - k_{75}} \quad (3-7)$$

where

$$k_{71} = - \frac{\sin (a \sqrt{-b_1})}{(-b_1)^{1.5}} - \frac{a}{b_1} \quad (3-7a)$$

$$k_{72} = -b_1^1 k_7 + \frac{F e a}{2} \quad (3-7b)$$

$$k_{74} = \frac{\sin (a \sqrt{-b_1})}{(-b_1)^{0.5}} + \frac{k_{14}}{b_1} [\cos (a \sqrt{-b_1}) - 1] \quad (3-7c)$$

$$k_{73} = \frac{k a^2}{4} - k_{11} k_7 \quad (3-7d)$$

$$k_{75} = -k_{11} k_{71} - \frac{k_{73} k_{74}}{k_2 EI} \quad (3-7e)$$

Deflection y_2 is numerically evaluable from Eq. 3-7. y_2 is then used in Eq. 3-6 to determine Θ .

When the applied force is in tension, and therefore b_1 in Eq. 3-4d is positive, the sine and cosine terms in the above expressions are replaced by hyperbolic functions which are expressed as:

$$\cos (a \sqrt{-b_1}) = \frac{1}{2} \left[\exp (a \sqrt{b_1}) + \exp (-a \sqrt{b_1}) \right],$$

and

$$\sin (a \sqrt{-b_1}) = \frac{-1}{2i} \left[\exp (a \sqrt{b_1}) - \exp (-a \sqrt{b_1}) \right].$$

Imaginary terms resulting from positive b_1 cancel out when these substitutions are made.

The equivalent spring restraints k and k_t in Figure C-21b and C-21c are

$$k = \frac{24 EI}{(a')^3} \quad (3-8)$$

and

$$k_t = \frac{EI}{a'' \left[1 + \frac{k/4}{k/3 + EI/(a'')^3} \right]} \quad (3-9)$$

where a' and a'' are defined in Eqs. 3-1 and 3-2.

When y_2 and Θ_1 are determined M can be solved from Eq. 3-4 and beam stresses are found from

$$S = \frac{MC}{I} + \frac{F}{A} \quad \text{or} \quad S = \frac{M(s-C)}{I} + \frac{F}{A} \quad (3-10)$$

Maximum stresses occur at $x = 0$, S_o , and $x = a$, S_a .

The analytical approach is to determine the force F at which either S_o or S_a is at the yield stress F_{cy} . Then

$$N_7 = \frac{F}{\cos 60^\circ \eta a} \quad (3-11)$$

C.3.2.5 Computerized Analysis

The analysis outlined in Section C.3.2.4 has been programmed for the Hewlett Packard 9810 Desk Computer and 9862A Calculator Plotter. Figure C-22 is a flow diagram for this program. It has the following features:

1. The inputs include parameters needed in the plot program as well as in the structural analysis part of the program. The latter includes an initial applied force, F -start, and an arbitrary increment ΔF .
2. Initially A , I and C_0 are computed. The quantity b_1 is then computed and its sign is checked by an IF statement which decides whether hyperbolic or trigonometric functions are applicable in the analysis. Results of analysis using either of these functions are branched to LBL 1.
3. Quantities y_2 and Θ_1 are next computed after all the k factors needed in their evaluation have been determined.
4. It has been found that near critical loads a small increment in F causes radical increases in y_2 and Θ_1 . If F is increased beyond the critical load point y_2 quickly rises to positive and then negative infinity and behaves like a tangent function for argument at $\pi/2$ radians. To avoid resulting irrational solutions, especially when F start is chosen to be larger than experience with a few runs would indicate it should be, a test is performed to determine if y_2 is greater than $0.01 a$. The 0.01 is arbitrary but found adequate to compute forces F within 1% of critical values. When the $y_2 > |0.01a|$ statement is satisfied N_7 is computed and sent into storage for plotting. Computed N_2 , y_2 , S_0 , S_a and F are printed out at this time.
5. If the $y_2 > |0.01a|$ test is not satisfied S_0 and S_a at the two ends of the beam-column are computed and individually checked against F_{cy} . If F_{cy} is not exceeded F is incremented by ΔF and the loop beyond LBL 1 is recycled. When F_{cy} is exceeded at either end of the beam column N_7 is computed and directed to LBL X² beyond which the indicated parameters are computed and printed.

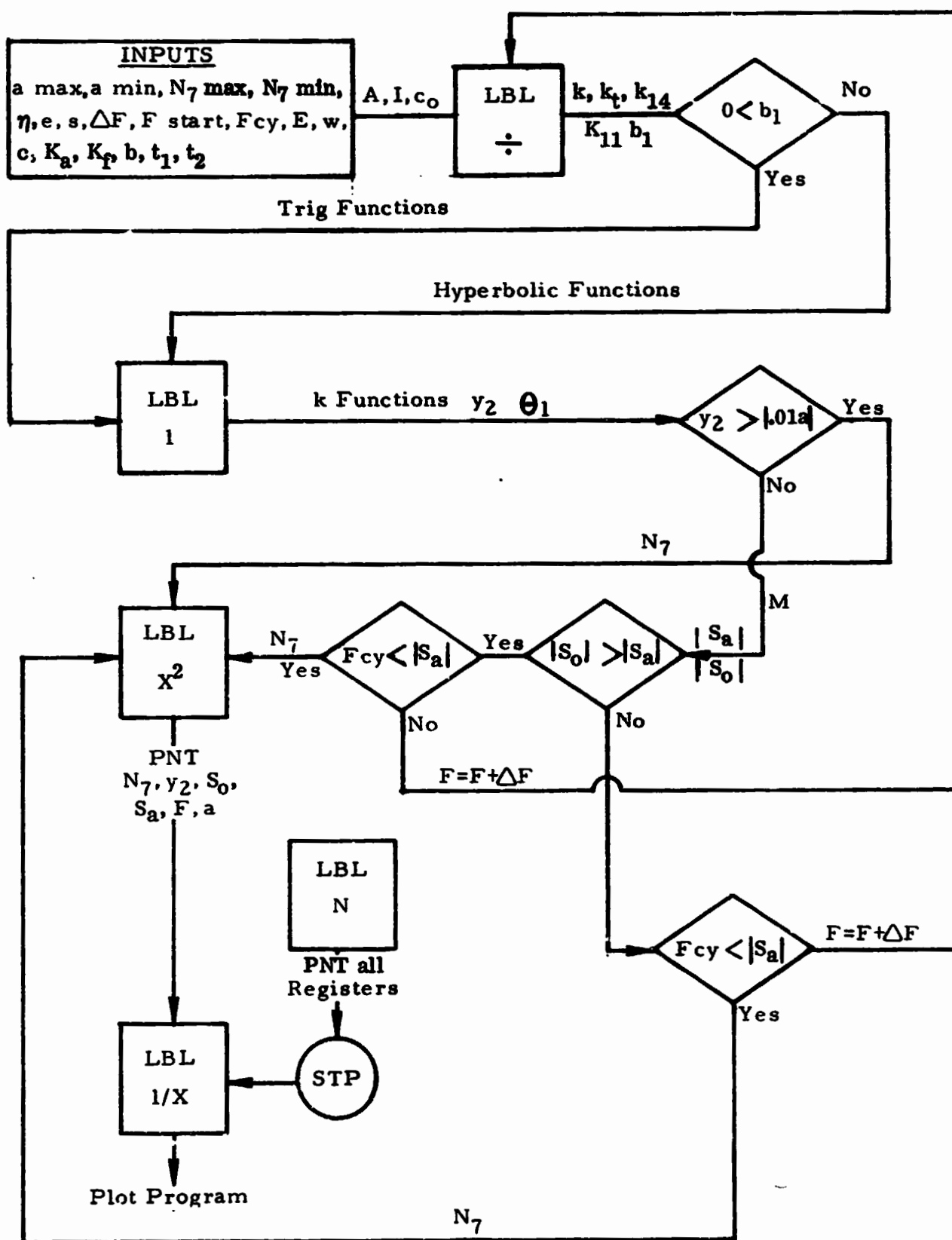


Figure C-22 Computer program flow diagram

6. After a is used beyond LBL X^2 it is incremented by 1 in. and returned to LBL \div for program recycling. The program ends when $a = a_{\min}$. at which time the plot program generates N_7 vs. a .
7. Force, F , is incremented from small to large values and the initial node-to-node spacing, a , is the largest to be plotted. This causes the maximum F for any a to always a good initial value for the succeeding a (since the load reacting capability of a column either increases or remains unchanged as its length decreases).

C.3.2.6 Numerical Evaluation

The following program parameter inputs include η , K_a , and K_f values found to produce analytical results that agree with the test results.

η	= 0.9	w	= 0.415
e	= 0.02 in.	c	= 0.082
s	= 0.73 in.	K_a	= 1.4
ΔF	= 100 lb.	K_f	= 1.4
F-start	= 2000 lb.	b	= 0.053
F_{cy}	= 60,000 psi	t_1	= 0.040
E	= 10^7 psi	t_2	= 0.052
Effective skin = $47 t_1$			

The $\eta = 0.9$ was estimated from data in Subsection C.2.5. The $e = 0.02$ in. was computed on the basis of 0.15 in. total anticlastic curvature offset measured in the full length (37.25 in.) of the test specimen. The s , w , c , b , t_1 and t_2 values are for the average grid member cross section from Figure C-1b. F-start and ΔF are arbitrary program operational values. F_{cy} and E are for the 2024-T851 aluminum from which the specimen is fabricated. Finally K_a and K_f factors were determined by exercising the program.

Influences of the different parameters affecting computed and automated plots of N_7 vs. a are studies in Figures C-23a to C-23d. In these figures program input parameters are as listed above except for one parameter being studied and indicated on each figure.

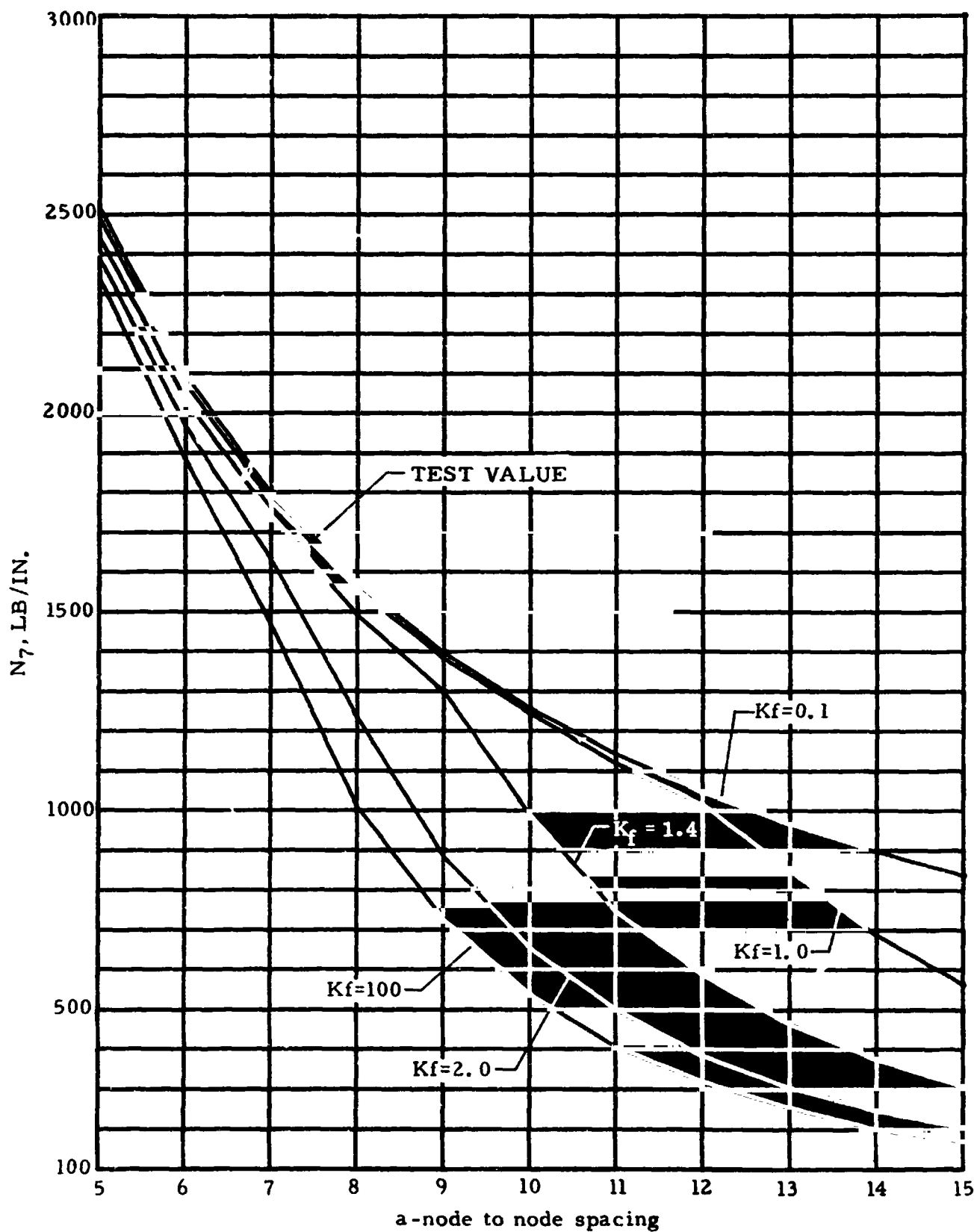


Figure C-23a. Computed N_7 vs a , in.

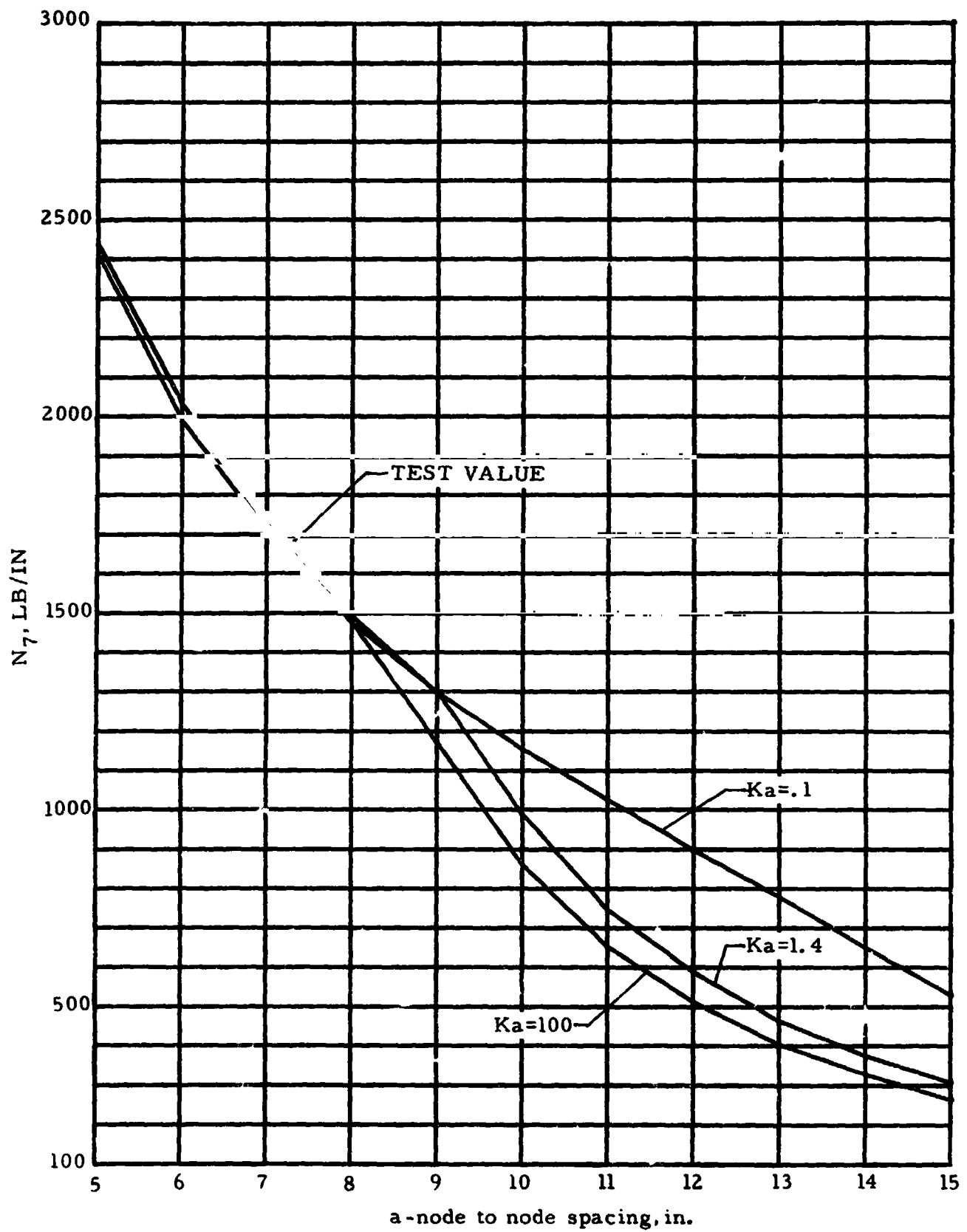


Figure C-23b Computed N_7 vs a .

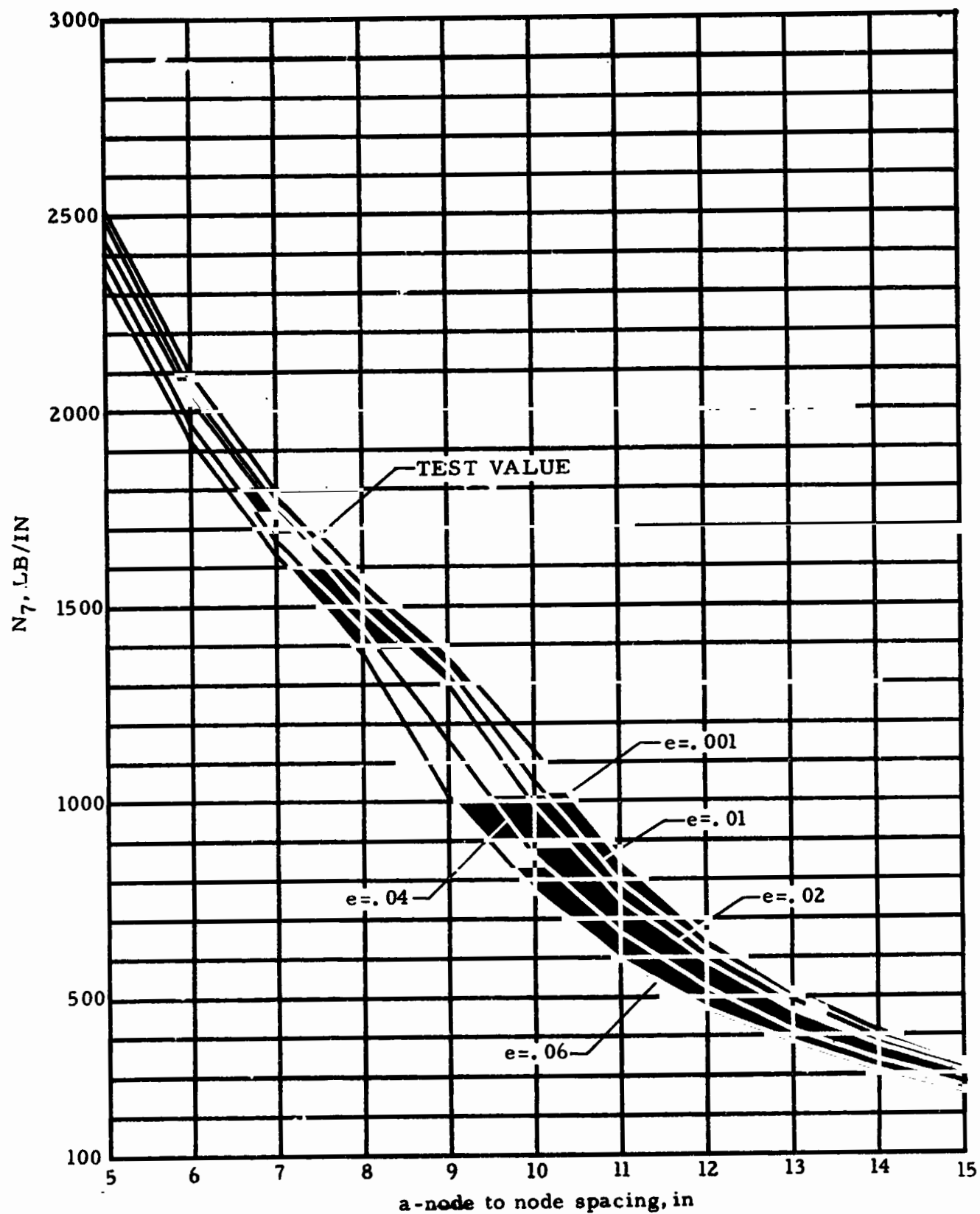


Figure C-23c Computed N_7 vs a , in.

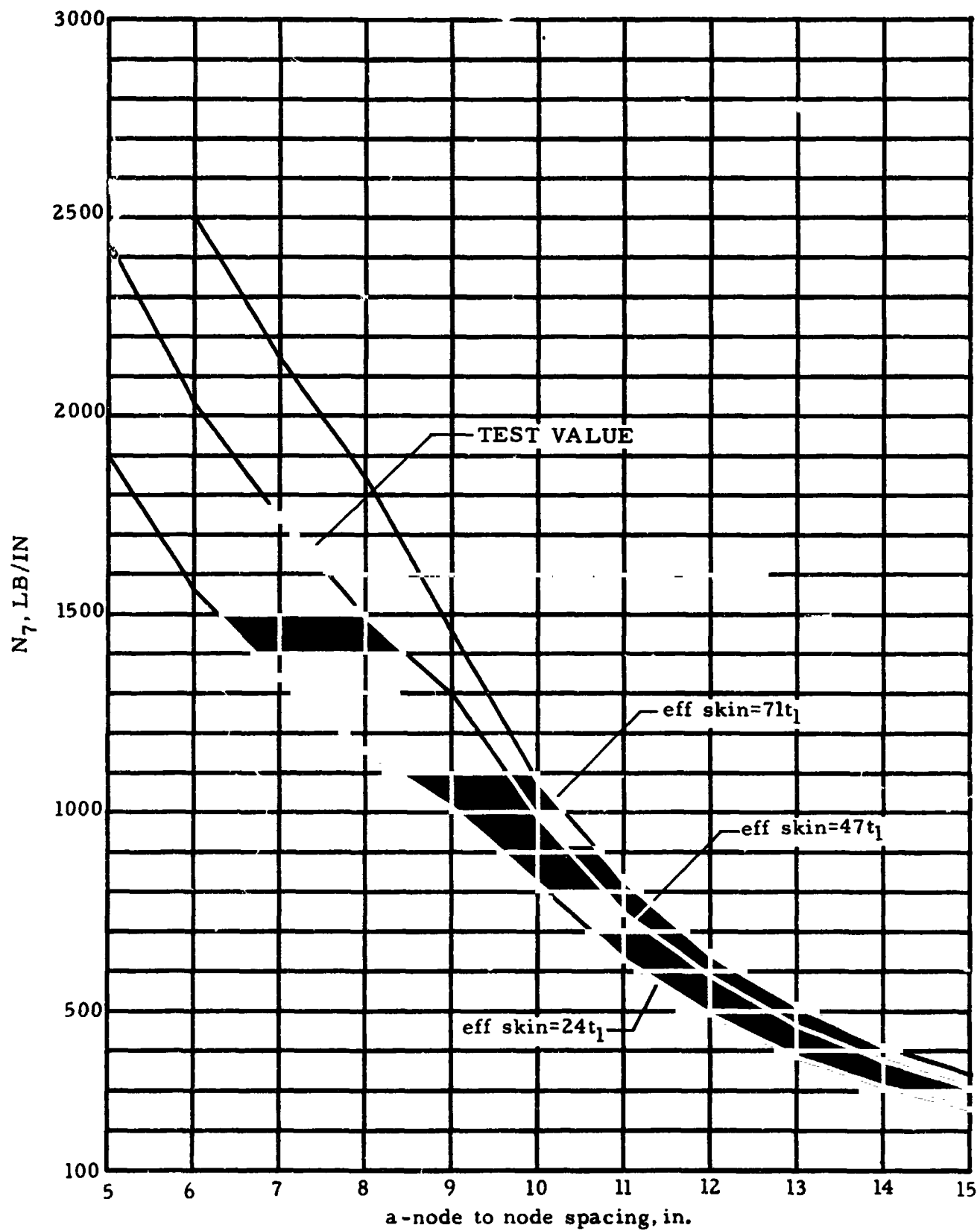


Figure C-23d Computed N_7 vs a , in.

Figure C-23a shows the effect of changes in K_f on N_7 . Note that the N_7 vs. a curve passes through the 1655 lb/in. test value when $K_f = 1.4$. Figure C-23b shows the effects of changes in K_a . It is apparent that K_f is more significant than K_a . Note also that the N_7 for $K_a = 0.1$ is slightly less than it is for the less-end-fixity case $K_a = 100$. This is because in the first case peak stresses develop at $x = 0$ where the distance to the extreme fiber C_o is greater than $s - C_o$ for the latter case in which peak stresses are at $x = a$.

For values of a greater than 9 inch N_7 values in Figure C-23b are controlled by the $y_2 > |0.01a|$ test in Figure C-22.

Figures C-23c and C-23d show effects of variations in e and effective skin. It is seen that e is not as critical a factor as the effective skin based on values chosen for each.

Table C-3 is a computer printout for the inputs listed at the beginning of this subsection. It is noted from observation of y_2 and a values that N_7 , S_o , S_a and F are determined from the $y_2 > |0.01a|$ test for values of $a = 15$ to 10 in. For these values the full stress F_{cy} of the beam column is not developed. For values less than $a = 9$ in. the full yield stress is developed at one end of the beam column (and $y_2 < 0.01a$).

C.3.3 EFFECTIVE SKIN WIDTH

The object of this subsection is to use isogrid adapter test data to develop relationships for predicting the effective skin width in compression to be included in grid member cross-section.

Preliminary evaluation of isogrid test data indicated that effective compression skin width acting with the stiffener is higher than predicted by the standard method used for skin-stringer design. To effectively use this added area, a method for predicting effective skin width consistent with available test data is developed.

The simplified analysis most often used for skin-stringer design assumes a plate of width $2w$ simply supported on all four sides working at the same stress level as the stringer.

REPRODUCIBILITY OF THE
ORIGINAL PAGE IS POOR

Table C-3. Computer printouts.

0.9000000		746.4949728
0.0200000		0.1153340
0.7300000		4.261709009 04
100.0000000		4.154176636 04
2.000000000 03		6.400000000 03
6.000000000 04		11.0000000
1.000000000 07	INPUTS	987.9394406
0.4150000		0.1101646
0.0820000		5.133463218 04
1.4000000		5.004995550 04
1.4000000		7.700000000 03
0.0530000		10.0000000
0.0400000		
0.0520000		1.297294215 03
0.5048276		0.0815181
0.1623980		6.071381274 04
0.0129647	Co	5.929973891 04
	A	9.100000000 03
	I	9.0000000
307.9291763	N ₇	1.491531948 03
0.1806909	Y ₂	0.0334215
2.417489474 04	So	6.001579195 04
2.349621992 04	Sa	5.892004088 04
3.600000000 03	F	9.300000000 03
15.0000000	a	8.0000000
375.7469115		1.741266175 03
0.1645130		0.0181030
2.753163533 04		6.063564649 04
2.677172763 04		5.964494402 04
4.100000000 03		9.500000000 03
14.0000000		7.0000000
463.8676694		2.031477205 03
0.1452583		0.0103138
3.147185460 04		6.028889269 04
3.96280779 04		5.937237530 04
4.700000000 03		9.500000000 03
13.0000000		6.0000000
588.0591908		2.437772646 03
0.1411165		0.0067272
3.695154679 04		6.009488248 04
3.596081792 04		5.922411321 04
5.500000000 03		9.500000000 03
12.0000000		5.0000000

For the skin section in Figure C-24 critical buckling stress;

$$F_{cCR} = KE \left(\frac{t}{2w} \right)^2 \quad (3-12)$$

For $l \gg 2w$, $K = 3.62$ for all sides simply supported.

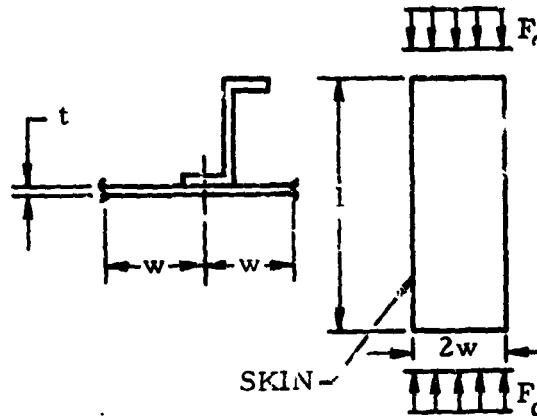


Figure C-24. Typical skin stringer geometry

Solving Eq. 3-12 for w in terms of F_c with $K = 3.62$

$$w = 0.95 t \sqrt{\frac{E}{F_c}} \quad (3-12a)$$

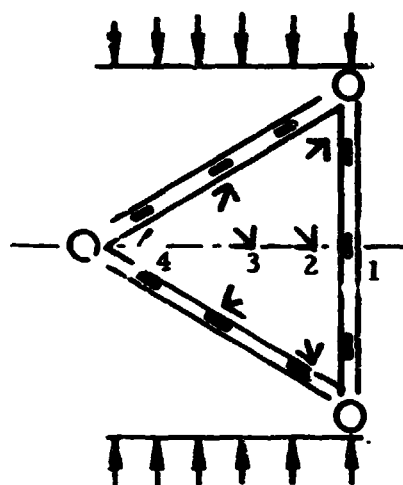
This is the classical equation for effective skin width. For a typical aluminum alloy working at $F_c = 40,000$ psi, $w = 15 t$ or $2w = 30 t$ is often used for preliminary sizing.

C.3.3.1 Test Data

One of the skin panels on the test specimen was instrumented with several rosette strain gages as shown in Figure C-25a. Figure C-25a and C-25b outline strain and stress data resulting from these gages. See Ref. C-1 for detailed test data.

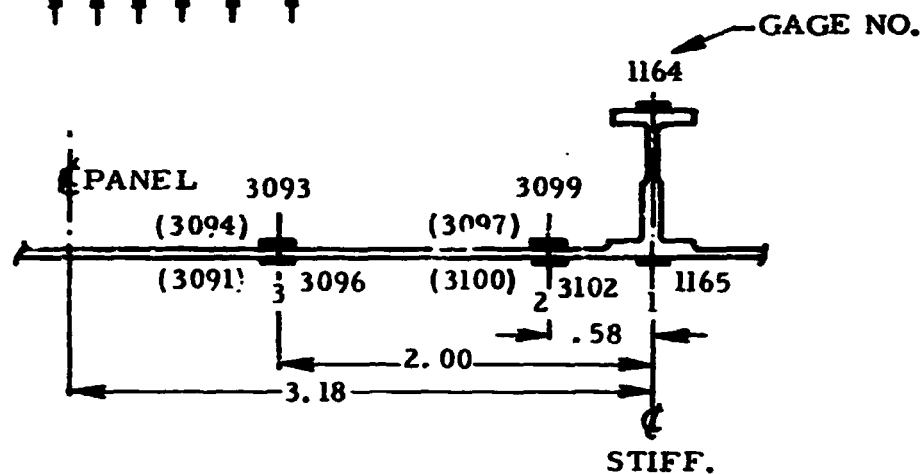
Figure C-26 is a plot of data in Figure C-25a. Figure C-27 shows calculations of average stress and factor C in effective skin determination based on test data. From Figure C-27 the effective skin width is

$$w = 1.67 t \sqrt{\frac{E}{F_c}} \quad (3-12b)$$



GAGES AT 1, 2 & 3 WERE USED TO
CALCULATE THE STRESS
DISTRIBUTION IN THE SKIN
AND STIFFENER.

() INDICATES GAGE AT
RIGHT ANGLE TO LOADING



GAGES IN DIRECTION OF LOADING					
STRAIN - μ IN/IN (COND 9A)					
GAGE	80%	120%	1' 0%	200%	240%
1164	-869	-1286	-1776	-2232	-2961
1165	-1431	-2775	-4063	-5654	-8642
3099	-970	-1631	-2299	-2962	-3246
3102	-1602	-2969	-4304	-5692	-7689
3093	898	1745	2396	2975	3373
3096	-2029	-3033	-3883	-4677	-5278

Figure C-25a Typical local specimen strain stress data

GAGES AT RIGHT ANGLE TO LOADING

Gage	Strain - μ in./in. (Cond 9A)				
	80%	120%	160%	200%	240%
3091	705	1026	1339	1656	1876
3094	-245	-41	209	454	703
3097	408	1499	2772	4123	5821
3100	645	721	668	475	-599

AVG STRAIN

PT	Strain - μ in./in. (Cond 9A)									
	80%		120%		160%		200%		240%	
	ϵ_{\parallel}	ϵ_{\perp}	ϵ_{\parallel}	ϵ_{\perp}	ϵ_{\parallel}	ϵ_{\perp}	ϵ_{\parallel}	ϵ_{\perp}	ϵ_{\parallel}	ϵ_{\perp}
1	-1415*	526†	-2666*	1098†	-4000*	1733†	-5560*	2399†	-8486*	3255†
2	-1286	526	-2300	1110	-3301	1720	-4327	2299	-5467	2611
3	-565	230	-644	492	-746	774	-851	1055	-952	1289

Calculate stresses parallel and perpendicular to direction of loading.

$$\sigma_{\parallel} = \frac{E}{1-\nu^2} (\epsilon_{\parallel} + \nu \epsilon_{\perp})$$

$$\sigma_{\perp} = \frac{E}{1-\nu^2} (\epsilon_{\perp} + \nu \epsilon_{\parallel})$$

AVG STRESS

PT	Stress - psi (Cond 9A)									
	80%		120%		160%		200%		240%	
	σ_{\parallel}	σ_{\perp}	σ_{\parallel}	σ_{\perp}	σ_{\parallel}	σ_{\perp}	σ_{\parallel}	σ_{\perp}	σ_{\parallel}	σ_{\perp}
1	-14503	1181†	-26960	3451†	-40155	6152†	-55849	8438†	-86648**	8186†
2	-13017	1617	-22696	4846	-32134	8419	-41968	11548	-54042	11202
3	-5723	698	-5727	3447	-5928	6348	-6167	9227	-6522	11577

$$*\epsilon_{\parallel} = \epsilon_{\text{Skin}} - \frac{.02}{.73} (\epsilon_{\text{Skin}} - \epsilon_{\text{Stiff}})$$

**Based on $E = 10.5 \times 10^6$. Material has obviously exceeded the yield stress so this value is too high.

†There were no rosette gages on the stiffener at point 1, so average stress is calculated using stresses perpendicular to loading direction at point 2. Assume stress perpendicular to loading direction at point 1 (σ_{\perp}) is equal to

$$\sigma_{\perp(1)} = \sigma_{\perp(2)} \frac{t_{(2)}}{t_{(1)}} \quad t_{(2)} = .038 \text{ in.} \quad t_{(1)} = .052 \text{ in.}$$

$$\sigma_{\perp} = \frac{E}{1-\nu^2} (\epsilon_{\perp} + \nu \epsilon_{\parallel})$$

Solving for ϵ_{\perp} :

$$\epsilon_{\perp} = \left(\sigma_{\perp} \left(\frac{1-\nu^2}{E} \right) - \nu \epsilon_{\parallel} \right)$$

Figure C-25b. Typical local specimen strain/stress data.

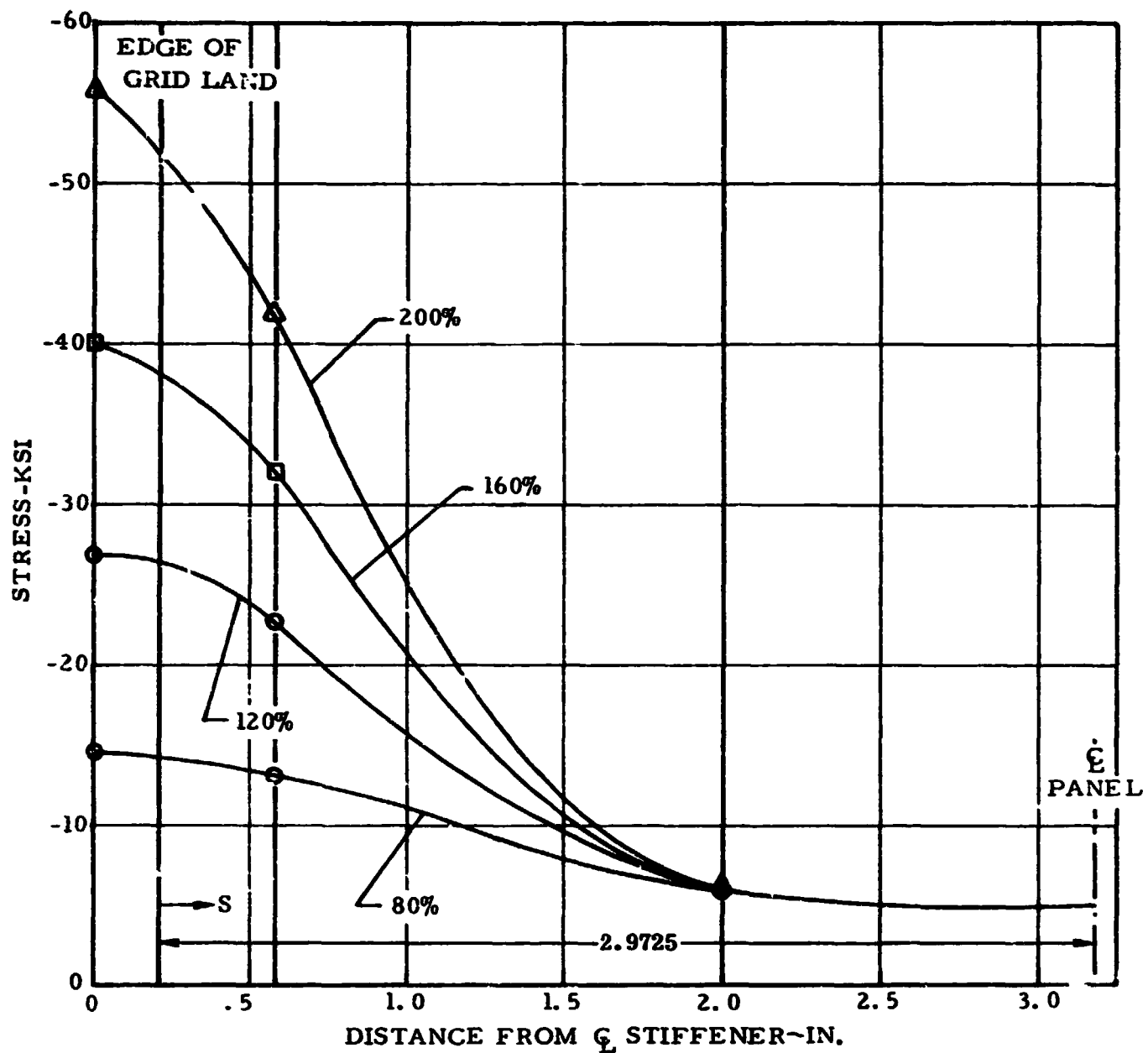


Figure C-26 Grid-skin stress distribution

AVG SKIN STRESS (KSI) AND EFFECTIVE WIDTH (IN)				
	80%	120%	160%	200%
σ_{Avg}	8.2013	11.1624	14.0504	16.9290
w	1.681	1.231	1.040	.901
c	1.64	1.64	1.69	1.73

$$\sigma_{Avg} = \left(\int_0^{2.9725} \sigma ds \right) / (2.9725)$$

$$\text{EFFECTIVE SKIN WIDTH, } w = \frac{2.9725 \sigma_{Avg}}{\sigma_{Stiff}}$$

WHERE $\sigma_{Stiff} = \sigma_{11} @ \text{PT (1) FROM FIGURE C-25b.}$

$$w = ct \sqrt{\frac{E}{F_c}}$$

SOLVING FOR c

$$c = \frac{w}{t \sqrt{E/F_c}}$$

WHERE $t = .038 \text{ IN}$

$$F_c = \sigma_{Stiff}$$

FROM THE ABOVE $c_{Avg} = 1.67$

Figure C-27 Effective skin calculations

C.3.3.2 Analytical Estimation of Effective Skin Width

From the analysis of compression buckling of skin panels in Subsection

C.3.4 K_C for the reference panel is 17.25.

$$K = \frac{K_C \pi^2}{12 (1 - \nu^2)} = 15.59 \quad (3-13)$$

$$\text{using } F_{c_{CR}} = KE \left(\frac{t}{2w} \right)^2$$

$$w = \frac{\sqrt{K}}{2} t \sqrt{\frac{E}{F_{c_{CR}}}} \quad (3-14)$$

and since $K = 15.59$

$$w = 1.97 t \sqrt{\frac{E}{F_C}} \quad (3-14a)$$

This is obviously optimistic since the K is based on all edges having substantial support above simple support. For all edges simply supported $K = 6.78$ and

$$w = 1.30 t \sqrt{\frac{E}{F_C}} \quad (3-14b)$$

Obviously the actual value of w falls somewhere between the values defined by equations 3-14a and 3-14b. Therefore letting

$$c_0 = \frac{\sqrt{K}}{2} \quad (3-14c)$$

The effective value of c can arbitrarily be defined as

$$c = 1.30 + \frac{c_0 - 1.30}{2} \quad (3-14d)$$

and the effective skin width is

$$w = ct \sqrt{\frac{E}{F_C}} \quad (3-14e)$$

Using Eqs. 3-14d and 3-14e for the test panel

$$c_0 = \frac{\sqrt{15.59}}{2} = 1.97$$

$$c = 1.30 + \frac{1.97 - 1.30}{2} = 1.64$$

which agrees closely with the measured values.

C.3.3.3 Analysis Procedure

1. Calculate skin panel buckling coefficient, K_c , using procedure outlined in Subsection C.3.4.
2. Calculate $K = \frac{K_c \pi^2}{12 (1 - \nu^2)}$
3. Calculate $c_o = \frac{\sqrt{K}}{2}$
4. Calculate $c = 1.30 + \frac{c_o - 1.30}{2}$
5. Calculate effective skin width

$$w = ct \sqrt{\frac{E}{F_c}}$$

As a conservative approximation w can be defined as

$$w = 1.30t \sqrt{\frac{E}{F_c}} \quad .$$

Using this relationship for w and $F_c = 40,000$ psi (aluminum)

$$w = 21.06 t \text{ and } 2w = 42.12 t \text{ (compares to } 2w = 30 t \text{ used for skin-stringer)}$$

which can be used for preliminary isogrid sizing.

C.3.4 COMPRESSION BUCKLING OF SKIN PANELS

The objective in this subsection is to use test data to develop relationships for predicting compression buckling of isogrid skins.

C.3.4.1 Measured Buckling Data Evaluation

Buckling of skins was measured by back-to-back rosette strain gages on four triangular skin panels. Outputs of these gages are plotted in Figures C-28a to C-28d for loading condition 7 in Reference 1. The figures also show ϵ_1 and ϵ_2 computed from this data.

ϵ_1 is the average strain in the direction of loading. ϵ_2 is the average strain perpendicular to the direction of loading. The point of incipient buckling is

defined as the point at which the ϵ_1 curves in Figures C-28a to C-28d start to deviate from a straight line. Critical buckling stress,

$$\sigma_{CR} = \frac{E}{1-\mu^2} (\epsilon_1 + \mu \epsilon_2) \quad (3-15)$$

ϵ_1 and ϵ_2 being the measured strains at incipient buckling

From Reference C-2 critical buckling stress can be defined as

$$\sigma_{CR} = \frac{K_c \pi^2 E}{12(1-\mu^2)} \left(\frac{t}{b} \right)^2 \quad (3-15a)$$

solving for K_c (the buckling coefficient)

$$K_c = \frac{12(1-\mu^2) \sigma_{CR}}{\pi^2 E (t/b)^2} \quad (3-15b)$$

where

t = average skin thickness, inch

b = panel size, inch.

K_c calculations are summarized in Table C-4 using data from Figures C-28a to C-28d. From Table C-4 the average value of K_c is 17.0.

Table C-4. K_c Calculations

Panel	Gages	t (in)	b (in)	ϵ_1 Micro Strain	ϵ_2 Micro Strain	σ_{CR} (psi)	K_c
1	3055/3058 3057/3060	0.039	6.35	-580	180	-6069	16.95
2	3091/3094 3093/3096	0.038	6.35	-550	240	-5861	17.25
3	3121/3124 3123/3126	0.37	6.35	-520	160	-5446	16.90
4	3147/3150	0.037	6.35	-520	150	-5480	17.00

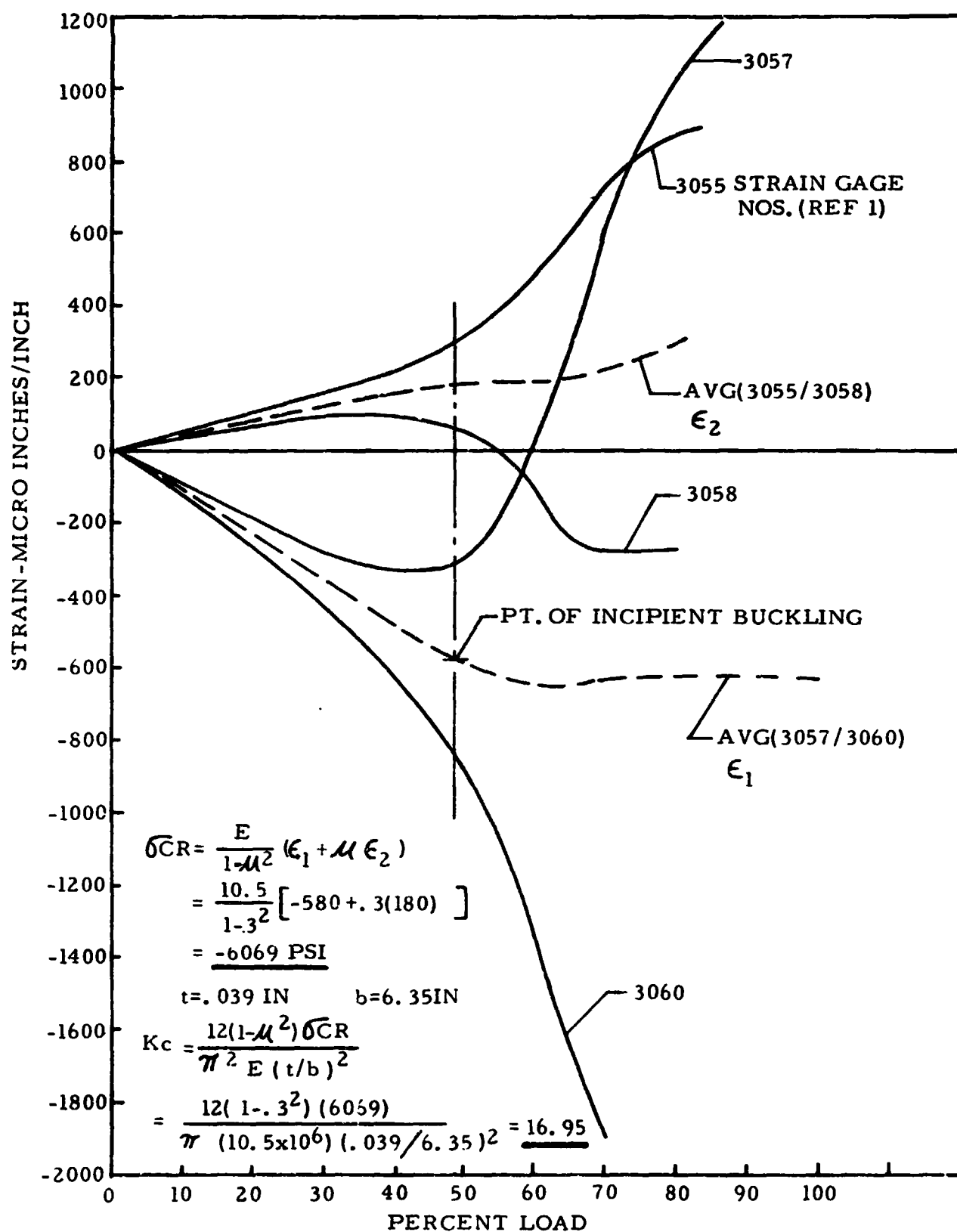


Figure C-28a Skin strains vs load

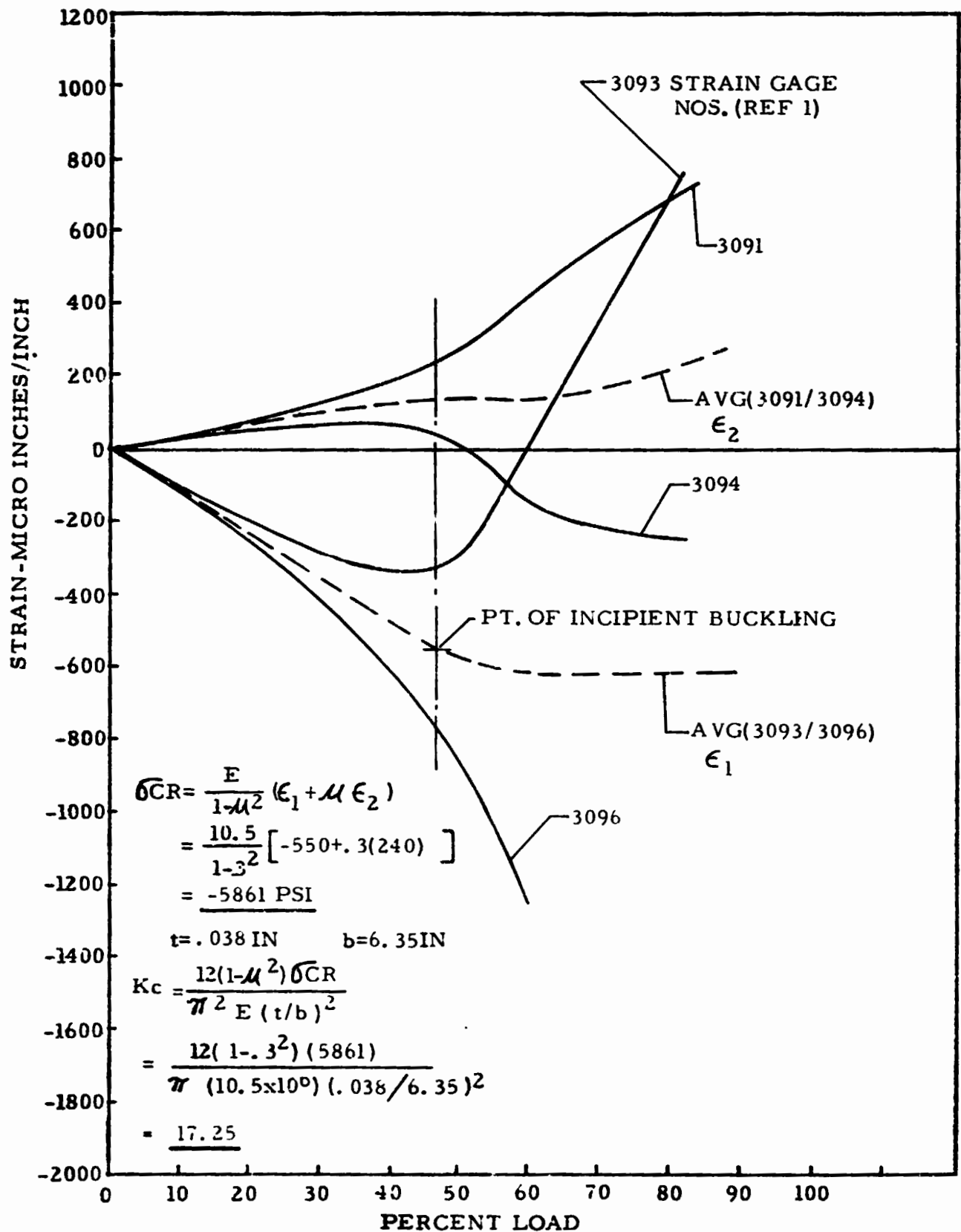


Figure C-28b Skin strains vs load

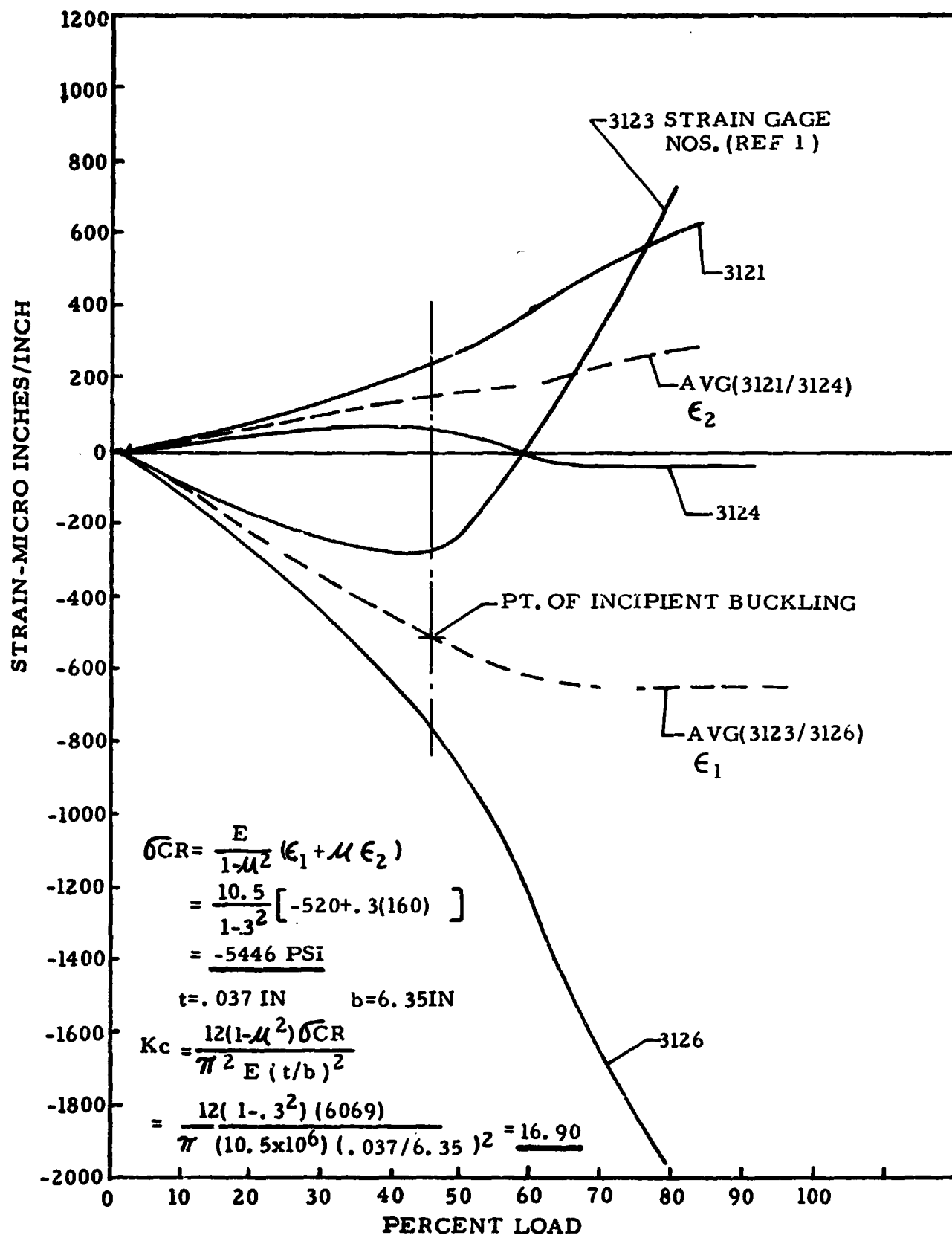


Figure C-28c Skin strains vs load

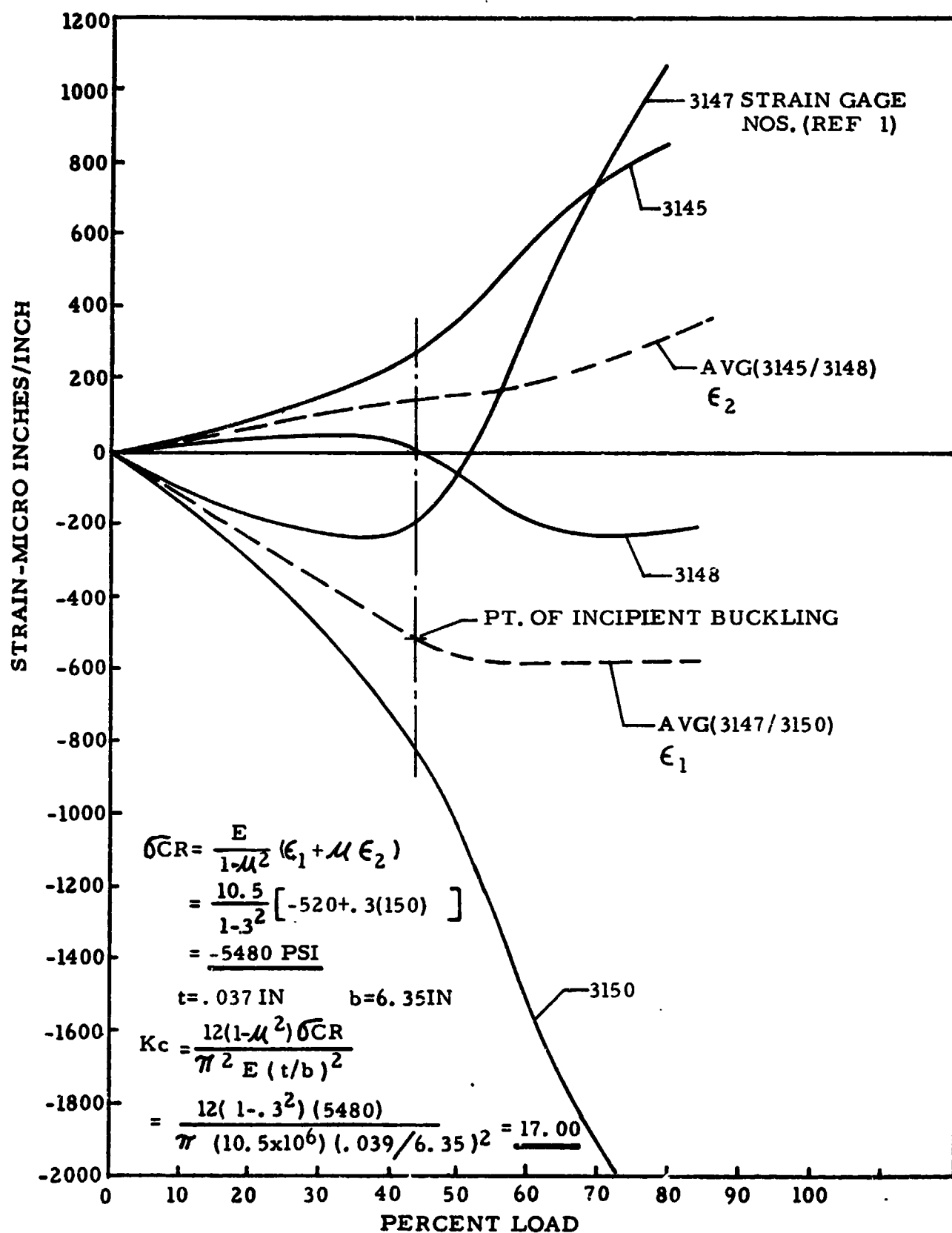


Figure C-28d Skin strains vs load

C.3.4.2 Effects of Skin Edge Fixity

Actually K_c is a function of the rigidity ratio,

$$\epsilon = \frac{\Theta_{\max \text{ skin}}}{\Theta_{\max \text{ grid member}}} \quad (3-16)$$

where $\Theta_{\max \text{ skin}}$ is the maximum edge rotation for a triangular skin panel subjected to a unit distributed edge moment and $\Theta_{\max \text{ grid member}}$ is the maximum rotation for a grid member subjected to a unit distributed moment.

Using Table C-5 and Figure C-29, rigidity ratios are calculated in Table C-6.

where

I = Minimum Moment of Inertia about the 0-0 axis in Figure C-29, in.⁴

J = Polar Moment of Inertia, in.⁴

Table C-5. Panel Geometry Values

Panel	Cages	Panel t	d	l	w	c	b ₁	b ₂	t ₂
1	3055/3058 3057/3060	0.039	6.35	7.33	0.415	0.085	0.055	0.083	0.057
2	3091/3094 3093/3096	0.038	6.35	7.33	0.415	0.085	0.054	0.083	0.052
3	3121/3124 3123/3126	0.037	6.35	7.33	0.415	0.087	0.058	0.086	0.056
4	3147/3150 3145/3148	0.037	6.35	7.33	0.415	0.085	0.053	0.083	0.051

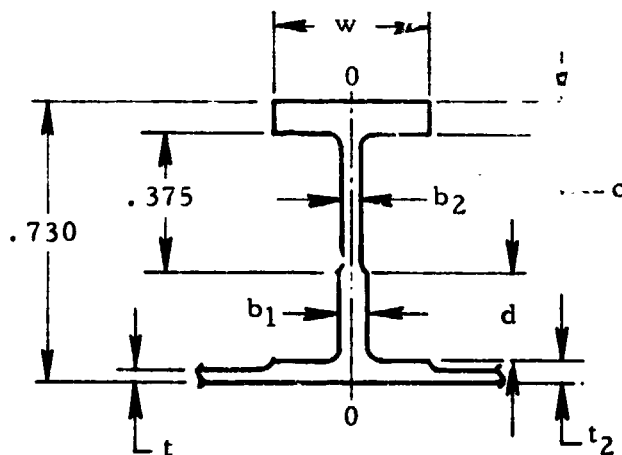


Figure C-29. Average Panel Geometry Sketch

Table C-6. Panel Rigidity Ratios

Panel	Gages	D	I	J	a	$\Theta_{\max_{\text{plate}}}$	$\Theta_{\max_{\text{stiff}}}$	ϵ
1	3055/3058 3057/3060	57.04	8.611×10^{-4}	1.720×10^{-4}	1.323	2.78×10^{-2}	6.91×10^{-4}	40.2
2	3091/3094 3093/3096	52.76	8.313×10^{-4}	1.656×10^{-4}	1.325	3.01×10^{-2}	7.18×10^{-4}	41.9
3	3121/3124 3123/3126	48.70	8.691×10^{-4}	1.847×10^{-4}	1.283	3.26×10^{-2}	6.37×10^{-4}	51.2
4	3147/3150 3145/3148	48.70	8.251×10^{-4}	1.636×10^{-4}	1.328	3.26×10^{-2}	7.27×10^{-4}	44.8

$$I = \frac{cw^3}{12} + \frac{.375 b_1^3}{12} + \frac{db_2^3}{12} + \frac{t_2 w^3}{12}$$

$$J = \frac{wc^3}{3} + \frac{.375 b_1^3}{3} + \frac{db_2^3}{3} + \frac{wt_2^3}{3}$$

In Equation 3-16 ϵ is computed with the following.

From Reference C-2

$$\Theta_{\max_{\text{skin}}} = \frac{b}{4D} \quad (3-16a)$$

where

$$D = \frac{Et^3}{12(1-\mu^2)} \quad (3-16b)$$

from Reference C-3

$$\Theta_{\max_{\text{grid member}}} = \frac{1}{2JG} \left[\frac{l}{4} - a \tanh \left(\frac{l}{4a} \right) \right] \quad (3-16c)$$

where

$$a = \frac{h}{2} \sqrt{EI/JG} \quad (3-16d)$$

h = Stiffener height

l = Stiffener Length, in.

Triangular panel compression buckling coefficient as a function of panel to edge member rotational rigidity ratio is plotted in Figure C-30 from the data in Tables C-4 and C-6.

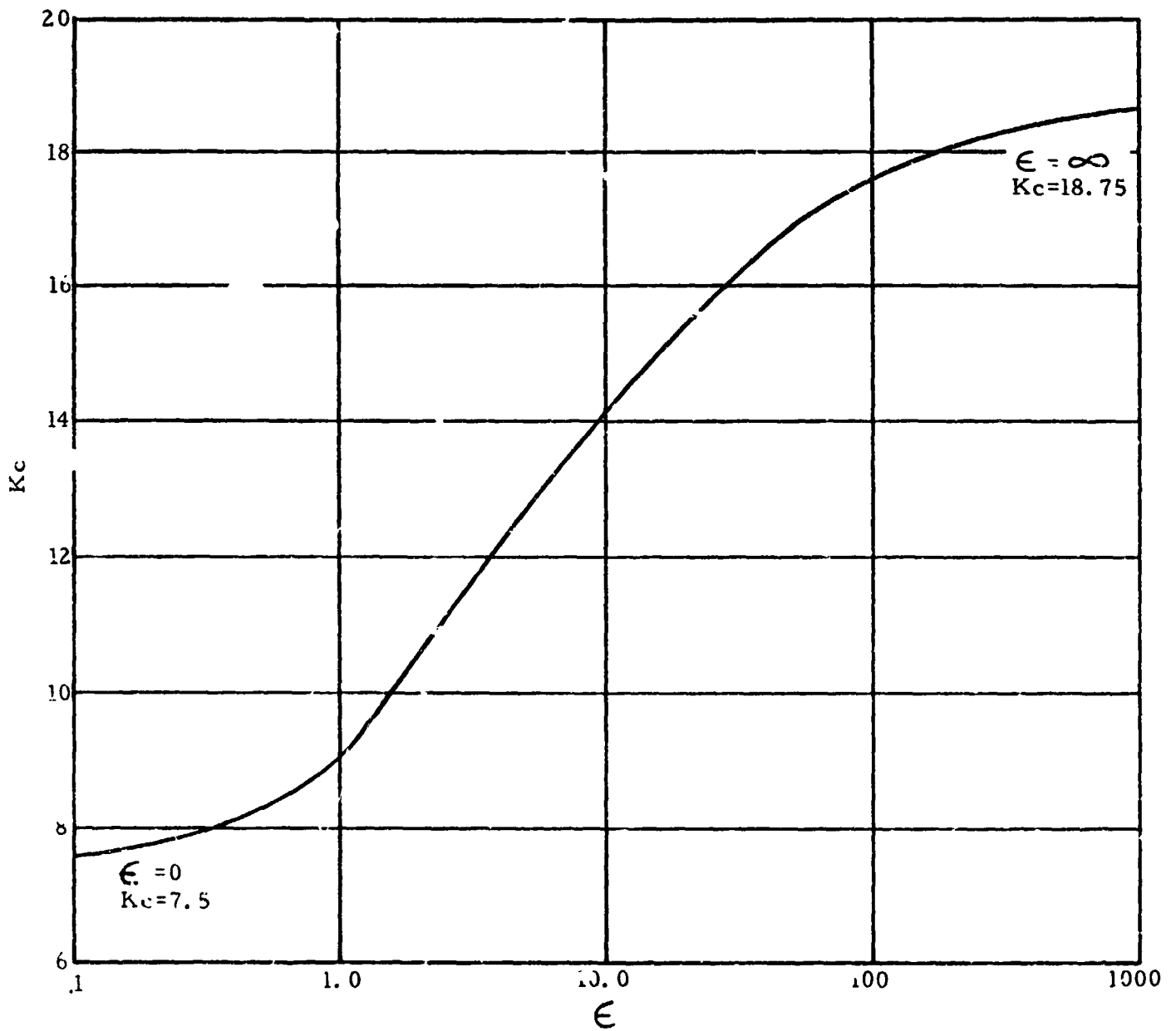


Figure C-30 Panel buckling coefficient vs edge rigidity ratio

C.3.4.3 Analysis Procedure

1. Calculate rigidity ratio, ϵ as outlined.
2. Using the calculated value of ϵ obtain K_c from Figure C-30.
3. Calculate critical buckling stress (uniaxial compression) for the panel from Equation 3-15a.

C.4 SUMMARY AND RECOMMENDATIONS

1. A limited treatment of the test data has been presented. The data has been used to evaluate knockdown factors for general instability, extended local instability, effective skin width and compression buckling of skin panels.
2. Failure of the loading fixture bolted flange jack bolts probably produced premature failure of the test specimen. It may also explain failure along the adapter lower end, although such failure modes in cylinders are common. The load reacted by the cylinder would likely have been 20% higher, were it not for the flange failure.
3. A unique automated method has been developed for generating topographical plots of radial deflection contours in the cylindrical adapter. The plots are used to anticipate and identify areas of incipient and actual structural failure.
4. A developed extended local instability analysis generally agrees with the general instability analyses presented in Appendix B.
5. Effective skin width and skin buckling evaluation techniques have been developed for isogrid structures.
6. It is recommended that test data be used in further evaluations including discrete element modeling of the test specimen.

The knowledge gained in conducting and evaluating the isogrid cylinder test will be significant in planning and executing future isogrid cylinder tests. It is recommended that if the subject test be rerun: (1) the loading fixtures be stiffened and strengthened, to ensure two orders of magnitude greater stiffness and strength in

the fixture as compared to that in the adapter; (2) greater concentration of back-to-back grid member strain gages be used in the expected failure area; and (3) only body bending load application be used, to maximize localization of failure area.

C.5 REFERENCES

- C-1 Hildebrand, A.G., Isogrid Cylinder Structural Test, NASA, MSFC Report No. IN-ET13-74-1, 1974**
- C-2 Timoshenko, S.P., Woinowsky-Krieger, S., Theory of Plates and Shells, McGraw Hill, 1959.**
- C-3 Seely, F.B., Advanced Mechanics of Materials, John Wiley and Sons, 1961.**